Energy Transfer Processes in Organic Molecular Semiconductors



Hannah Julia Eggimann

Linacre College

University of Oxford

A thesis submitted for the degree of

Doctor of Philosophy

Trinity 2020

Acknowledgements

First and foremost, I would like to express my sincere thanks and appreciation to my supervisor Prof Laura Herz - for her guidance, support, patience and encouragement and for being an academic role model. I am further grateful to Prof Michael Johnston for his support and practical advice. I would also like to thank my Master thesis supervisor Prof Klaus Ensslin for his encouragement to pursue a doctorate.

I am very grateful for the received funding from the EPSRC and the Fondation Zdenek and Michaela Bakala who made the time of my DPhil in Oxford much less worrisome.

To the Herz-Johnston group: you are amazing! Thank you all for your collaboration and friendship. I especially want to thank Dr Rebecca Milot and Dr Jay Patel for sharing their expertise and experience, Dr Juliane Gong for her introduction to the PL-upconversion system and Kimberley Savill for the many hours we spent aligning, discussing and troubleshooting "our" system together.

Meeting many wonderful people is one of the greatest joys of Oxford. I would like to thank everyone from the CLS cohort, the house group and the Monday breakfasts for their friendship and companionship. Alissa & David, Erin, Heather & Brad, Lena & Nathan - thanks for being part of our Oxford life. Special thanks also to Christy for introducing me to the fun of running 21.1 km and to Melissa for our friendship and the Tuesday night dinners and conversations. Further thanks and appreciation goes to St Andrew's church for encouragement and support.

It was overwhelming to have so much support from our friends back home. A "Merci tuusig" to everyone who visited us in Oxford. I am especially obliged to my school friends Simone and Adrienne and to my sister Rebekka for their continuing friendship and patiently listening to all the joys, worries and frustrations of being a DPhil student.

I am truly grateful to my family, especially to my parents Dorothea and Dietmar, for their constant support and love - without you I would not be where I am. Finally, I would like to express my immense gratitude to my husband Sven for being my best friend and my greatest support!

Soli Deo Gloria.

Abstract

Organic semiconductors exhibit excellently suited material properties for a variety of applications and offer the possibility of low-cost and large-scale production. This thesis analyses photonic properties of several organic semiconductors, which are of great interest for different applications. To explore these materials, a combination of steady-state and time-resolved optical measurement techniques is employed and energy transfer dynamics within organic semiconductors are modelled. Research was focused on the following areas:

The influence of the fraction of chain segments that adapt β-phase conformation on film microstructure of thin films of the blue-emitting polymer PFO is consistently investigated for the first time. An analysis of emission and absorption properties of PFO films with systematically varying β-phase content indicates that with increasing β-phase in PFO films, the chain conformation becomes more planar and includes more repeat units.

Energy transfer, which occurs upon photoexcitation from glassy-phase to β-phase chain segments in PFO thin films is evaluated in terms of Förster resonant energy transfer theory. Differences in Förster radii calculated from ultrafast emission dynamics and spectral overlap between steady-state emission and absorption indicate that the energy transfer process is influenced by exciton diffusion within the glassy phase.

Parasitic absorption of light in a molecular sun-facing charge extraction layer (CTL) of a metal halide perovskite (MHP)-based solar cell structure is addressed. Experimentally observed energy transfer between layers of photoexcited conjugated polymers and a MHP layer is combined with modelling the efficiency of the energy transfer process. Efficient energy transfer is found to counteract parasitic light absorption in the CTL for thin layers ($\leq$ 10 nm) and/or high PLQE materials.

Morphological changes in films of the hole-transport material P3HT deposited on $MAPbI_3$ are explored. Changes in aggregation are observed through careful analysis of absorption and emission spectra from P3HT films of varying thickness and spin speed during their fabrication on a $MAPbI_3$ layer.

Contents

Publications vii

Abbreviations viii

1 Introduction 1
- 1.1 Thesis Structure . . . 4

2 Electronic Processes in Organic Semiconductors 6
- 2.1 Excitations in π-conjugated Systems . . . 7
  - 2.1.1 Molecular States . . . 7
  - 2.1.2 Absorption and Emission Spectra . . . 9
  - 2.1.3 Excitations . . . 12
- 2.2 Aggregates in Polymeric Semiconductors . . . 16
- 2.3 Förster Resonant Energy Transfer . . . 17
  - 2.3.1 Point Dipole Approximation by Förster . . . 19
  - 2.3.2 Refined Models of FRET . . . 21
  - 2.3.3 FRET in Restricted Geometries . . . 24

3 Experimental Methods 27
- 3.1 Steady State PL Spectra . . . 28
- 3.2 PL-Upconversion . . . 29
  - 3.2.1 Operating Principle . . . 29
  - 3.2.2 Measurements . . . 32
- 3.3 Time-Correlated Single Photon Counting . . . 35
  - 3.3.1 Operating Principle . . . 35
  - 3.3.2 Measurements . . . 37
  - 3.3.3 Time Resolution . . . 37
- 3.4 Fourier Transform Infra-Red Spectroscopy . . . 39
  - 3.4.1 Operating Principle . . . 39
  - 3.4.2 Measurements . . . 41

4 Influence of β-phase Content on Chain Conformation in PFO Films 43
4.1 Background and Motivation . . . 44
4.2 Sample Preparation . . . 47
4.3 Experimental Details . . . 49
4.3.1 Absorption . . . 49
4.3.2 PL . . . 50
4.3.3 PLQE . . . 50
4.3.4 TCSPC . . . 50
4.4 Results . . . 51
4.4.1 Absorption . . . 51
4.4.2 Time-Integrated PL . . . 56
4.4.3 PLQE and Decay Rates . . . 59
4.5 Discussion . . . 63
4.6 Summary and Conclusion . . . 68

5 Energy Transfer in PFO Films with Varying β-phase Content 69
5.1 Background and Motivation . . . 70
5.2 Experimental Details . . . 71
5.3 Results and Analysis . . . 72
5.3.1 Calculating Förster Radius from PL Dynamics . . . 72
5.3.2 Calculating Förster Radius from Donor Emission and Acceptor Absorption Spectra . . . 82
5.4 Discussion . . . 88
5.5 Summary and Conclusion . . . 93

6 Energy Transfer between Layers of Photoexcited Organic Semiconductor and Metal Halide Perovskite 94
6.1 Background and Motivation . . . 95
6.2 Sample Preparation . . . 97
6.2.1 Substrate Cleaning . . . 97
6.2.2 $MAPbI_3$ Layer . . . 97
6.2.3 Polymer Layers . . . 98
6.3 Absorption and PL Spectra . . . 100
6.3.1 F8BT . . . 101
6.3.2 Super Yellow . . . 103
6.3.3 P3HT . . . 105
6.3.4 PTAA . . . 106
6.3.5 $MAPbI_3$ . . . 108
6.4 PLQE . . . 109

6.5 PL Lifetimes . . . 111
6.6 Fluorescence Decay and ET Efficiency Model . . . 112
6.6.1 FRET in Two-Layer Geometry . . . 114
6.6.2 PL Decay Modelling . . . 117
6.6.3 Calculation of ET Efficiency . . . 122
6.7 Discussion . . . 126
6.8 Summary and Conclusion . . . 131

7 Aggregation in P3HT Films on a Metal Halide Perovskite Layer 132
7.1 Background and Motivation . . . 133
7.2 Sample Preparation . . . 135
7.3 Absorption . . . 135
7.4 Photoluminescence . . . 136
7.5 Discussion . . . 140
7.6 Summary and Conclusion . . . 145

8 Conclusion and Outlook 146

References 150

Publications

Eggimann, H. J., Le Roux, F. and Herz, L. M. 'How β-Phase Content Moderates Chain Conjugation and Energy Transfer in Polyfluorene Films'. *J. Phys. Chem. Lett.*, 2019, **10**, 1729-1736.

Haver R., Tejereina, L., Jiang H.-W., Rickhaus, M., Jirasek, M., Gruebner, I., **Eggimann, H. J.**, Herz, L. M. and Anderson, H. L. 'Tuning the Circumference of Six-Porphyrin Nanorings'. *J. Am. Chem. Soc.*. 2019, **141**, 7965-7971.

Ulatowski A. M., Wright A. D., Wenger, B., Buizza L. R. V., Motti S. G., **Eggimann, H. J.**, Savill K. J., Borchert, J., Snaith, H. J., Johnston M. B. and Herz, L. M. 'Charge-Carrier Trapping Dynamics in Bismuth-Doped Thin Films of $MAPbBr_3$ Perovskite'. *J. Phys. Chem. Lett.*. 2020, **11**, 3681-3688.

Eggimann, H. J., Patel, J. B., Johnston, M. B. and Herz, L. M. 'Efficient Energy Transfer Mitigates Parasitic Light Absorption in Molecular Charge-Extraction Layers for Perovskite Solar Cells'. *Nat. Commun.*, 2020, **11**, 5525.

Abbreviations

BBO . . . . . Beta-Barium-Boronate
CCD . . . . . Charge Coupled Device
CTL . . . . . Charge Transport Layer
(E)ET . . . . . (Excitation) Energy Transfer
F8BT . . . . . $(C_{35}H_{42}N_2S)_n$
FRET . . . . . Förster Resonant Energy Transfer
FTIR . . . . . Fourier-Transform Infrared Spectroscopy
FWHM . . . . Full Width Half Maximum
GaP . . . . . Gallium Phosphide
IRF . . . . . Instrumental Response Function
$MAPbI_3$ . . . Methylammonium Lead Iodide
MHP . . . . . Metal Halide Perovskite
OFET . . . . . Organic Field-Effect Transistor
OLED . . . . . Organic Light Emitting Diode
P3HT . . . . . Poly(3-hexylthiophene)
PFO . . . . . Poly(9,9-dioctylfluorene)
PL . . . . . Photoluminescence
PLQE . . . . . Photoluminescence Quantum Efficiency
PTAA . . . . . Poly[bis(4-phenyl)(2,4,6-trimethylphenyl)amine]
SFG . . . . . Sum-Frequency Generation
SHG . . . . . Second Harmonic Generation
Si . . . . . Silicon
SPAD . . . . . Single Photon Avalanche Detector
TAC . . . . . Time-to-Amplitude Converter
TCSPC . . . . Time-Correlated Single Photon Counting
UV . . . . . Ultra Violet

1 Introduction

To address the current climate crisis, the development and improvement of new technologies and materials is decisive [1–4]. An effective response to the global issue of a changing climate is complex and multifaceted and needs to consider various interconnected aspects including climate research, socio-economical policies, material research or the human response [5, 6] (Fig. 1.1). To transition to a net-zero society without (or negative) green-house gas emissions, novel approaches for supplying sustainable energy are of key importance. Decarbonisation of current energy systems needs to be achieved in a context where future energy demand is projected to increase due to population increase and where energy services such as heating or transportation are increasingly electrified [7, 8]. In order to escape the current carbon lock-in [9] within the next decades, technologies such as solar cells and more efficient lighting play a critical role [1–4, 10, 11].

Organic semiconductors are in this context a rising and highly promising class of materials. They show semiconducting properties such as absorption and emission in the visible range, have a low dielectric constant and intermediate conduction and are predominantly carbon-based. In contrast to traditional non-organic semiconductors

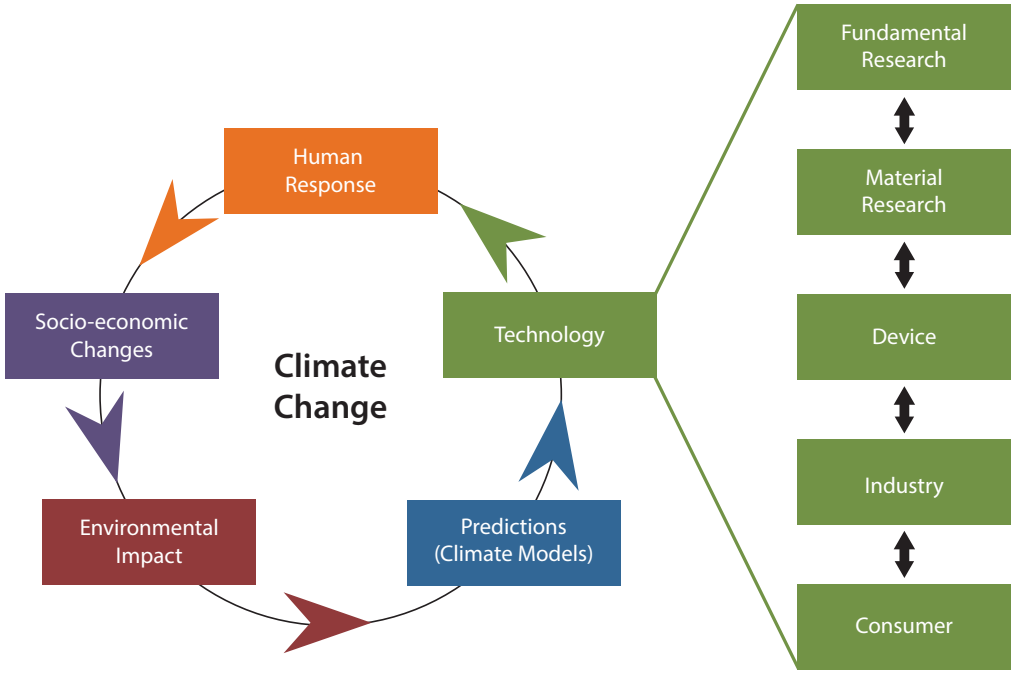


Figure 1.1: Schematic depiction of the interconnected aspects to address climate change with interrelated areas involved in developing new technologies. (Left part after [12].)

many of their material properties are not intrinsic but arise from injection of charges, doping and dissociation of photo-generated charges [13]. Organic semiconductors are well-suited for a range of applications as they posses tailorable electronic properties, offer potential for low-cost and large-scale production and are light-weight, flexible and robust [14, 15].

Organic semiconductors are roughly divided into two categories: small molecules and polymers, with the latter being the main focus of this thesis. The semiconducting properties of π-conjugated polymers stem from the molecular π orbitals being delocalised along the polymer backbone. Their discovery in the 1970s by MacDiarmid, Heeger and Shirakawa [16] was rewarded in the year 2000 with the Nobel prize [17]. Due to the designability and robust mechanical properties of the polymers, different applications such as organic LEDs (OLEDs) and light-harvesting technologies have been proposed and demonstrated since [15, 18, 19].

1. Introduction

The first OLED was presented by Tang and VanSlyke in 1987 [20]. Since then, considerable research effort has been undertaken (see inter alia [21–23]) and OLEDs are commercially in use today. They are commonly found in smartphones and computer or television displays. Another field of application for organic semiconductors are organic field effective transistors (OFETs) [19, 24–26]. Furthermore, conjugated polymers have been implemented in light-harvesting applications [27–29]. The principle idea of these systems is to mimic the processes of natural photosynthesis. A crucial point thereby is understanding and tailoring the energy transport dynamics of the photo-induced excitations. Comprehending natural light-harvesting processes has been an important motivation from the early development of theories on excitation energy transfer mechanisms [30].

Applications such as organic solar cells or OLEDs involve the conversion of light into energy or vice versa. An in-depth understanding of optical properties and of the dynamic processes upon photo-excitation in these materials is crucial for the development of efficient, well-working devices. Fundamental properties of luminescent organic semiconductors can be probed by optical measurements. Decisive electronic processes that determine the efficiency of a device occur at a variety of time-scales ranging from fs to ns. Therefore, a combination of steady-state and time-resolved optical measurements including ultrafast spectroscopy is well-suited to investigate optoelectronic properties of organic semiconductors and energy transfer processes.

This thesis presents an investigation of optoelectronic properties of organic semiconductors that show potential for applications in OLEDs, OFETs and solar cells. To this end, a range of steady-state and time-resolved measurement techniques were employed. The performed work adds to a better understanding of fundamental properties of these organic semiconductors, which is crucial for advancing future technology developments.

1.1 Thesis Structure

The structure of this thesis is as follows:

Chapter 2 provides an overview on photonic properties of organic semiconductors with a focus on π-conjugated polymers. Key to the experimental investigations of this thesis are a brief analysis of the interplay between morphology and photophysical properties including aggregate formation and a review of Förster resonant energy transfer (FRET) theory.

In **Chapter 3**, the experimental techniques used to investigate absorption and photoluminescence (PL) from polymer samples are outlined in detail. Polymer morphology was mainly investigated through steady-state PL measurements and Fourier-transform infra-red (FTIR) spectroscopy. Dynamic processes in polymers occurring upon photoexcitation were investigated by the time-resolved PL measurement techniques PL-upconversion and time-correlated single photon counting (TCSPC). For each of these techniques, the working principle is explained and the measurement set-up is described.

Chapters 4 and 5 present research on thin films of fluorene-based polymers which are highly promising for applications in OLEDs, OFETs and lasers. Recent advantages in the fabrication of Poly(9,9-dioctylfluorene) (PFO) thin films allow for reliable and wide tuning of the proportions of its two phases of polymer conformation. Based thereupon, the influence of the fraction of β-phase conformation present in a PFO thin film on photophysical properties was systematically investigated. The research questions addressed in these two chapters are:

- How does variation in β-phase content influence chain conformation and PL quantum efficiency (PLQE) in PFO thin films? (Chapter 4)
- How does a change in β-phase content affect FRET in PFO thin films? (Chapter 5)

Chapter 6 addresses parasitic light absorption in metal-halide perovskite (MHP) solar cells by organic semiconductor sun-facing charge transport layers (CTL), which

could be counteracted by efficient energy transfer to the MHP. To this aim, the energy transfer between a photo-excited front polymer layer and a MHP layer is experimentally observed and a model for the efficiency of the energy transfer is developed. The main research question asked thereby is:

- How can efficient energy transfer between a photo-excited organic semiconductor as CTL and a MHP layer be achieved as a function of CTL thickness, PLQE and absorption coefficient?

The focus of **Chapter 7** lies on film morphology of polymer layers within a metal-halide perovskite solar cell structure. Specifically, changes in aggregation are observed and discussed for the hole-transport layer material P3HT deposited on methylammonium lead iodide ($MAPbI_3$). The analysis is embedded in the wider discussion on the nature of aggregates in P3HT and the following research question is addressed:

- How does variation in film thickness and spin speed during sample preparation influence film morphology of P3HT films deposited on a $MAPbI_3$ layer?

Finally, **Chapter 8** summarises the key findings of this thesis and gives an outlook to possible further research.

2

Electronic Processes in Organic Semiconductors

Contents

2.1 Excitations in π-conjugated Systems 7
2.1.1 Molecular States 7
2.1.2 Absorption and Emission Spectra 9
2.1.3 Excitations 12
2.2 Aggregates in Polymeric Semiconductors 16
2.3 Förster Resonant Energy Transfer 17
2.3.1 Point Dipole Approximation by Förster 19
2.3.2 Refined Models of FRET 21
2.3.3 FRET in Restricted Geometries 24

This chapter provides the background for the experimental investigation and discussion of photonic properties of organic semiconductors in Chapters 4-7. The research presented in this thesis focuses on π-conjugated polymers. Their properties are therefore primarily considered here. Section 2.1 provides a brief overview of the fundamental physics involved in photo-exciting organic semiconductors. In Section 2.2, the nature of aggregates in polymeric semiconductors is discussed. Section 2.3 introduces Förster resonant energy transfer and outlines the theoretical framework of applying the theory to restricted geometries.

2.1 Excitations in π-conjugated Systems

The term *π-conjugated polymer*, or commonly abbreviated simply as *conjugated polymer*, refers to polymeric (Greek for "many parts") systems with alternating single and double bonds, which gives rise to a high degree of electron delocalisation [31]. Conjugated polymers show electrical activity upon photo-excitation [13]. This section addresses the nature of the excited states created in this process and the characteristics of the general electronic structure of organic semiconductors. An in-detailed description on this is for example found in the textbooks by Köhler and Bässer [13], Strobl [32] and Valeur and Barberan-Santos [33]. The first two subsections of this chapter are primarily based on these sources.

2.1.1 Molecular States

The electronic states of molecules differ in their nature and complexity from the electronic states of atoms or solids. A *molecular state* consists of several possible *configurations*, derived from *molecular orbitals*, where a configuration describes the distribution of the electrons within the molecular orbitals. One approach to obtain molecular orbitals is to approximate them as a linear combination of the underlying

atomic orbitals; A σ molecular orbital is composed of either two s atomic orbitals, one s and one p atomic orbital or two p_z (z-axis along the bond) atomic orbitals. Similarly, a π molecular orbital is formed from two $p_{x,y}$ atomic orbitals. Overlapping π molecular orbitals lead to the delocalisation of electrons, which is characteristic for conjugated polymers.

Of particular interest for understanding the excited states of a molecule are the *highest occupied molecular orbital (HOMO)* and the *lowest unoccupied molecular orbital (LUMO)*, in reference to the molecular ground state. For the case of conjugated polymers, the HOMO is a bonding π-(molecular)-orbital and the LUMO is an anti-bonding π^*-(molecular)-orbital.

The total wavefunction of a molecular state is usually treated as a product of electronic wavefunction (describing the electrons and their position relative to the nuclei in the system), spin wavefunction (describing the spin function of the individual electrons and the total resulting spin) and vibrational wavefunction (describing vibrational motion of the nuclei): $\Psi_{total} = \Psi_e \times \Psi_{spin} \times \Psi_{vib}$. This product approach holds only true because the *Franck-Condon principle* applies. It states that electronic transitions are considered to take place at a fixed internuclear separation, which is expressed through the configuration coordinate Q. An illustration of the Franck-Condon principle is given in Fig. 2.1. The principle is based on the electronic transition taking place on much shorter time scales than nuclear motion (i.e. molecular deformation) due to large differences in mass of the electron and the nuclei (*Born-Oppenheimer approximation*). On a larger time scale, the nuclei in return responds to this non-equilibrium position by vibrating. This is often treated in a harmonic oscillator framework. Therefore, a change in electronic state is usually accompanied by a change in vibrational level (so-called "vibronic transitions"). The principle breaks down for strong vibronic coupling.

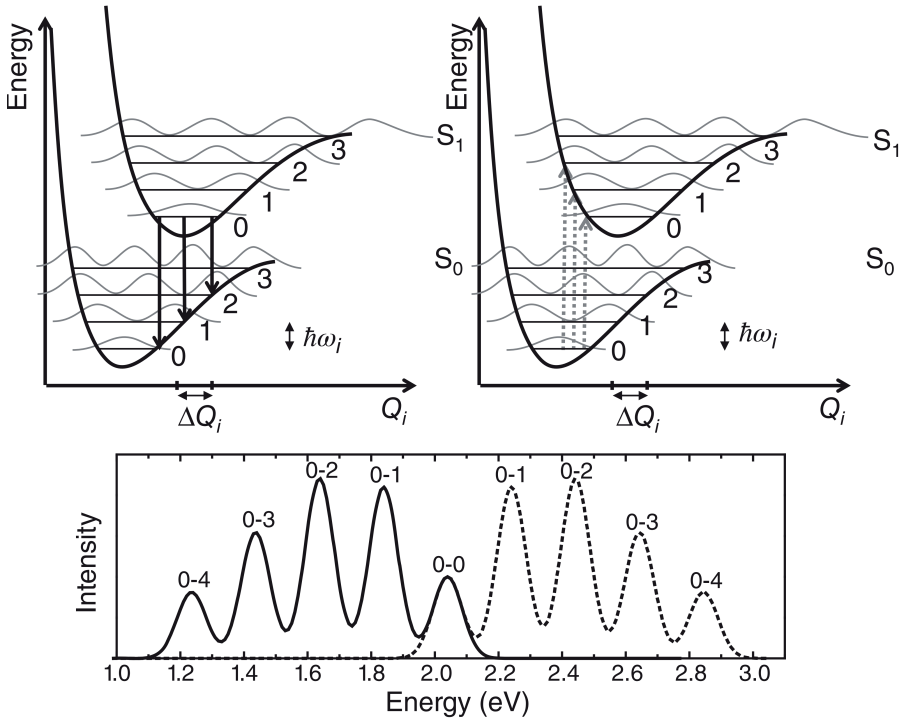


Figure 2.1: Franck-Condon principle depicted for transitions between molecular potentials as a function of configuration coordinate Q (top) and its implications for emission (left) and absorption (right) spectra (bottom). The principle implies that transitions happen vertically as a function of configuration coordinate and that the spectra show a vibronic progression. (Taken from Ref. [13], p.42. Copyright Wiley-VCH Verlag GmbH & Co. KGaA. Reproduced with permission.)

2.1.2 Absorption and Emission Spectra

Absorption and *emission* result from radiative transitions between molecular states. The rate of emission and absorption is governed by the electronic, vibrational and spin characteristics of the two involved molecular states. High transmission rates presuppose the involved electronic wavefunctions to be of the same spin parity and to have well overlapping and extended orbitals. The peak pattern in absorption and emission spectra is partially defined by the vibrational characteristics of the states through *vibronic progression* (see Fig. 2.1). The vibronic progression is characterised by the *Franck-Condon factor*, which is determined by the squared overlap integral of the vibrational wavefunctions and can further be expressed as

$$I_{0-m} = \frac{S^m}{m!} e^{-S} \tag{2.1}$$

for the case of a transition from the 0^{th} level of the ground state to the m^{th} vibrational level of an excited state. S thereby denotes the *Huang-Rhys parameter*, which quantifies the geometric reorganisation energy of an electronic transition:

$$S = \frac{1}{2} k \frac{\Delta Q^2}{\hbar\omega_m}, \tag{2.2}$$

where ΔQ is the displacement in configuration coordinate, k is the force constant and $\hbar\omega_m$ is the vibrational energy, which is based on a harmonic oscillator picture.

Symmetry considerations forbid specific transitions between molecular states. There are generally no transitions between states of different spin manifold (i.e. singlet and triplet states). However, singlet-triplet transitions can be enabled through spin-orbit coupling.

In addition to the radiative transitions, non-radiative transitions between the molecular states can occur. Non-radiate transitions are denoted as *internal conversion* if they take place without change of spin and *intersystem crossing* if both, singlet and triplet, spin states are involved. Furthermore, *vibronic relaxation* denotes the transition from a higher-lying vibrational level to the 0^{th} vibrational level of the electronic state.

Possible transitions are summarised in a Jablonski diagram as shown in Fig. 2.2. The electronic singlet and triplet states are depicted with their vibrational levels. Absorption takes place from the ground state of the molecule. *Fluorescence* occurs from the 0^{th} vibrational level (Kasha's rule) of the singlet state, whereas *phosphorescence* first involves intersystem crossing and occurs from 0^{th} vibrational level (again: Kasha's rule) of the triplet state. The electronic and vibrational states of a molecule are determined by its composition, structure and environment and the transitions between these states define absorption and emission spectra. Thus, examining these spectra is an important tool to gain information about the molecule and its configuration.

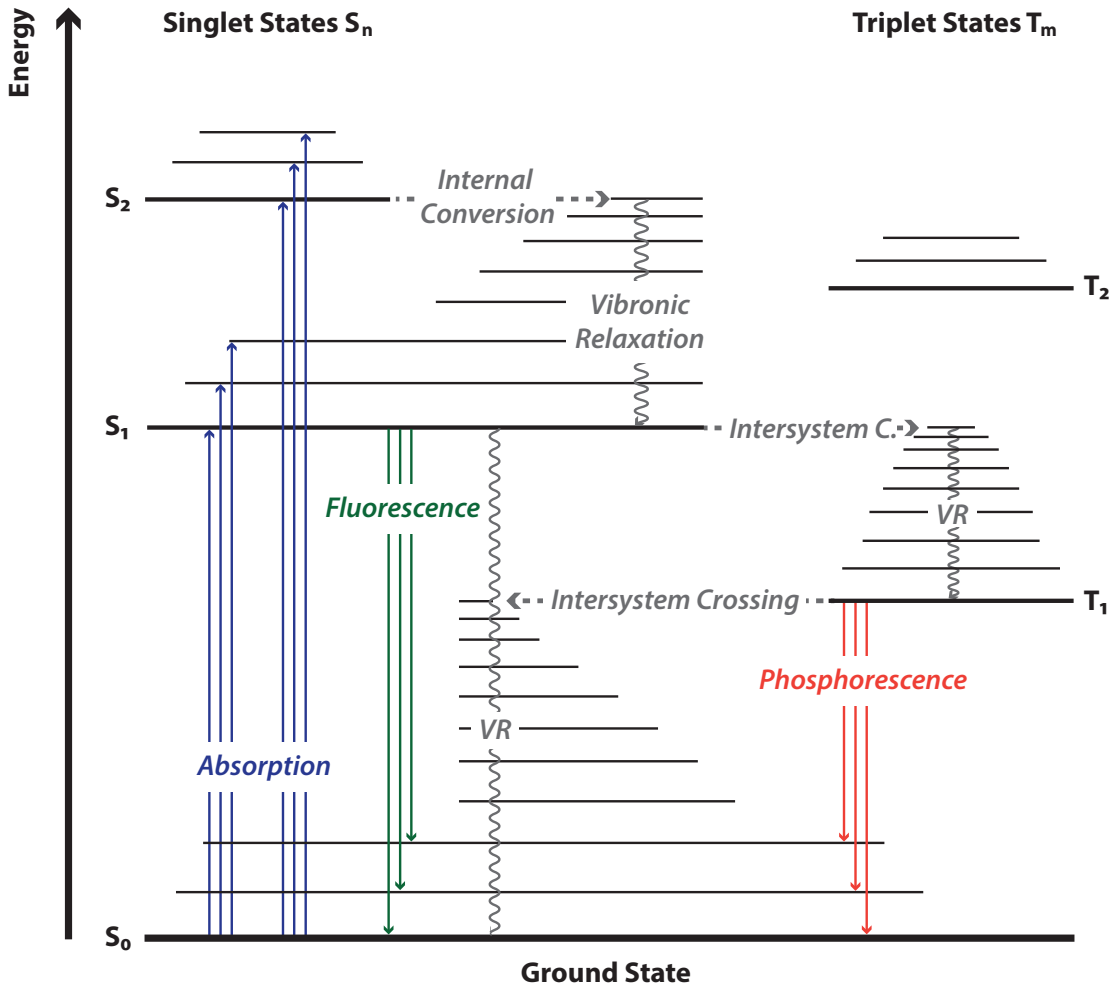


Figure 2.2: Jablonski diagram summarising possible transitions between the electronic states and their vibrational levels of a molecule. (After [13].)

In Fig. 2.1, absorption and emission spectra are depicted as mirror-images. In reality, this is rarely the case and the emission spectrum is red-shifted in reference to the absorption spectrum. The difference between the maxima observed in absorption and emission spectra is called *Stoke's shift*.

To this point, only a single molecule was considered and the various effects stemming from the presence of other molecules have been neglected. Importantly, however, the interplay of molecules with each other as well as with their environment also influence the shape of absorption and emission spectra. Two effects which are of particular importance for the discussion in latter chapters are aggregation and energy transfer, which are discussed below in Sections 2.2 and 2.3.

2.1.3 Excitations

Most considerations up until now generally hold for organic semiconductors. This section addresses conjugated polymers more specifically and provides a brief overview on the most common concepts used to describe excitations in π-conjugated systems that emerge for example through photo-excitation.

A common approach employed in the context of excitations in conjugated polymers is the *effective conjugation length*. An intuitive picture of this concept is for the polymer to be a "string of repeat units" [13]. Within this picture, the conjugation length is defined by the number of coherently coupled repeat units on which an excitation is delocalised, which is a measure of the extent of coherent coupling along the polymer chain [13].

The most simple model to interpret an absorption spectrum of π-conjugated oligomers is the *free electron/particle in a box model* in which the oligomer is treated

as a one-dimensional box with infinite barriers and zero potential inside [13, 34]. Using these boundary conditions, the energy levels become

$$E_N = \frac{h^2}{8m_e L^2} N^2 \tag{2.3}$$

where h denotes Planck's constant, m_e the mass of the electron, L the width of the potential well and N the number of involved π-electrons. Following this approach, the difference in energy, ΔE, between the highest occupied level (due to spin degeneracy this is N/2) and the lowest free level is

$$\Delta E = \frac{h^2}{8m_e d^2} \left[\frac{1}{N} + \frac{1}{N^2}\right], \tag{2.4}$$

where d denotes the difference between adjacent C molecules. This model has been extended by Hans Kuhn to account for the alternating single and double C-C bonds of the polymer backbone by introducing a sinusoidal potential inside the box [35]. His assumption leads to the following prediction for the energy gap between the levels:

$$\Delta E = \frac{h^2}{8m_e L^2} (N+1) V_0 \left[1 - \frac{1}{N}\right], \tag{2.5}$$

where V_0 is the amplitude of the sinusoidal potential. Kuhn shows that his model fits experimental data performed on different dye molecules [35]. However, this agreement is doubted by others [13], who highlight that the predicted vanishing excitation energy for an infinite polymer chain does not reflect reality.

This simple free electron approach does not account for any electron-electron interactions. The impact of their interaction can be addressed by using a one-electron *Hückel Hamiltonian* [13, 34, 36]. This method was for example used by Kohler [37] to include electron-electron interactions into his calculations and to obtain the absorption spectra of polyenes.

A different approach to model the electronic states in a molecule was proposed by Lewis and Calvin [38]: *Coupled oscillators*. The core idea of their model is to consider the polymer, which in their case was polyene, as a chain of coupled

oscillators. The C double bonds are treated as the oscillators and the C single bonds as the coupling between them. The thereby predicted relation of the wavelength λ of the first absorption maxima and the chain length (represented by N, which denotes the number of oscillators) is

$$\lambda^2 \;=\; k_0\, N \tag{2.6}$$

where k_0 is the force constant derived from the oscillators [34]. This behaviour was indeed observed for longer polyenes [38]. This model was later further refined by Werner Kuhn [39]. Torras *et al.* [34] have compared different excitation models for the lowest transition energy for Th-based oligomers and have found good agreement for the adapted coupled oscillator model.

The most widely used concept to describe excitations in conjugated polymers is the *(molecular) exciton* [34, 40–42]. An exciton is a bound electron-hole pair which can occur upon the absorption of a photon. Basic exciton theory neglects any interactions between molecules. Typically, excitons are discussed either as *Wannier excitons* or *Frenkel excitons*, which are both named after the author of their first description [13]. Wannier excitons [43] on the one hand are loosely bound electron-hole pairs with their "exciton radius" extending the molecule. Frenkel excitons [44] on the other hand denote tightly bound pairs of electrons and holes with a small "exciton radius". Both concepts allow for specific mathematical treatment of the excitation. The concept of Wannier excitons is for example applied to describe excitations in metal-halide perovskites that are investigated for solar cell applications [41]. Frenkel excitons have for instance been employed as a starting point to interpret the excited states in light-harvesting purple bacteria [42].

Torras *et al.* [34] have suggested that molecular excitons should additionally be categorised as *interchain* or *intrachain* in the context of conjugated polymers to distinguish whether the excitonic delocalisation is along the backbone of the

polymer (intrachain) or whether the exciton is delocalised between chromophores due to coupling between them (interchain). An exciton model based on intrachain excitons has been been implemented by Beljonne *et al.* [40] to study linear polyenes and oligothiophene single crystals. Their model was found to reproduce the optical features observed in these materials due to the presence of intrachain interactions.

The differentiation between intrachain and interchain is generally of great importance when discussing the diffusion of excitations and excitation energy transfer (see Section 2.3.2) after initial (photo)-excitation.

One further widely applied notion used to describe excitations in conjugated polymers is the *polaron* [45, 46]. If a charge is placed within a lattice, its surrounding neighbourhood will be polarised, which manifests itself as a lattice distortion. The quasi-particle polaron, which was originally introduced by Landau [45] for crystal lattices, therefore characterises a charge (electron or hole) with its surrounding polarised distortion. Within a band picture of electronic transitions, a distinctive feature of a polaron are two mid-gap states between the conduction and valence band gap and optical transitions can occur between these mid-gap-states and the conduction and valence band [32]. The concept has been adapted in the field of conjugated polymers, where the distortion now refers to intra-molecular or intra-chromophore bonds [13].

2.2 Aggregates in Polymeric Semiconductors

One important concept used to understand the relationship between photophysical observations and the morphology of assembled conjugated polymers are molecular *aggregates*. Originally developed by Kasha *et al.* [47] to understand absorption and emission in small molecules, the idea of aggregates has become very important for recent research on conjugated polymers [48–51]. The concept is based on interactions between the polymers, which can be of intrachain (through bond) or interchain (between polymer chains) nature, and their impact on the polymer assembly [48].

Two types of aggregates are commonly differentiated: H- and J-aggregates. The arrangement of the chromophores in relation to each other is thereby decisive for the type of aggregate that is likely to form: side-by-side (favouring interchain interactions) orientation leads to H-aggregation whereas head-to-tail (favouring intrachain interactions) orientation leads to J-aggregation [48]. Aggregate formation leads to changes in the electronic states of the polymer and thus influences absorption and emission spectra. The two key indications for aggregation observed in spectra are i) blue-shifted absorption for H-aggregates and red-shifted absorption for J-aggregates and ii) enhanced emission for J-aggregates and suppressed emission for H-aggregates [52].

H-aggregates have for example been observed for P3HT (poly(3-hexylthiophene)) thin films [53, 54], whereas J-aggregate behaviour has been reported in nanofibers of the same polymer [55]. Furthermore, the theory of aggregates in conjugated polymers has recently been extended to include so called “HJ-aggregates”, which take the competition between interchain and intrachain interactions and therefore between the formation of H- and J-aggregates into account [49, 56].

2.3 Förster Resonant Energy Transfer

Excitation energy transfer (EET) between an energy donor and an energy acceptor plays an important role in understanding photonic properties of organic semiconductors. EET occurs either radiatively by emission and re-absorption of a photon, which is also referred to as trivial transfer [13] or non-radiatively by quantum chemical coupling between a donor and an acceptor molecule or chromophore. Within non-trivial energy transfer, two cases, each named after the main contributor to the development of the theory, are distinguished: *Dexter-type* energy transfer which involves the exchange of an electron or a hole between the donor and the acceptor [57] and *Förster-type* energy transfer [30, 58, 59], which is based on interactions between the donor and the acceptor and does not involve an interchange of particles.

Energy transfer in π-conjugated systems from an excited donor molecule to an acceptor molecule in its ground state is usually discussed in the framework of Förster-type energy transfer [60–62]. After a short introduction, the focus of this section lies on summarising the original approximation by Theodor Förster (Section 2.3.1) and more recent models (Section 2.3.2) and adaptations (Section 2.3.3) of the theory used to investigate the rate of EET in different systems.

As a starting point for a quantum mechanical approach to determine k_{da}, the rate of energy EET from an energy donor to an energy acceptor, a modified *Fermi's Golden* rule can be used [61, 63]:

$$k_{da} = \frac{2\pi}{\hbar} |V_{da}|^2 J \tag{2.7}$$

where V_{da} denotes the matrix element of the coupling strength and J is the spectral overlap factor given by the experimentally measured and normalised fluorescence spectrum of the donor $I_d(\lambda)$ and the extinction coefficient of the acceptor $\epsilon_a(\lambda)$

$$J = \int I_d(\lambda)\epsilon_a(\lambda)\lambda^4 \, d\lambda. \tag{2.8}$$

A graphical illustration of the spectral overlap is given in Fig. 2.3.

Eq. 2.8 states that the rate of EET is determined by the overlap of the donor fluorescence and acceptor absorption spectra (no energy transfer occurs if there is no overlap) and by the matrix element of the donor-acceptor coupling. The nature of the coupling strength, however, is not yet specified by the expression. The matrix element V_{da} is defined as:

$$V_{da} = \langle \psi_f | \hat{H} | \psi_i \rangle \tag{2.9}$$

where $\hat{H}$ is the Hamiltonian describing the coupling of the initial and final state wavefunctions $\psi_{i,f}$. Neither the wave functions of initial and final states nor the exact form of the interaction Hamiltonian are trivial and need to be evaluated carefully since they reflect many-body problems in molecules.

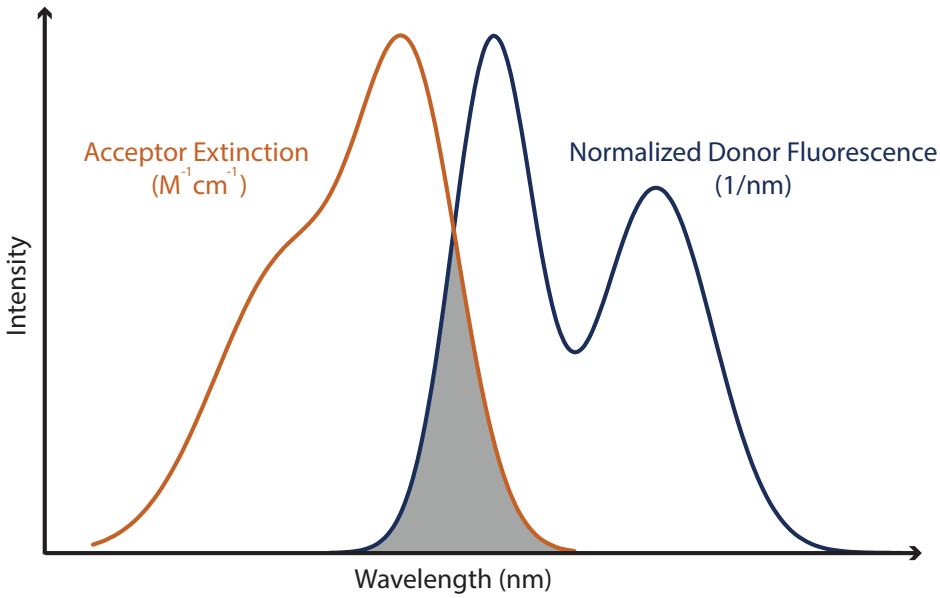


Figure 2.3: Graphical illustration of the spectral overlap between absorption extinction (orange) and normalised donor fluorescence (blue) using arbitrary scaling. The area for spectral overlap is depicted in grey. The actual overlap integral includes a factor of λ^4.

2.3.1 Point Dipole Approximation by Förster

Ground-breaking work on non-radiative and non-exchange-type EET was accomplished by Theodor Förster [30, 58, 59] whom the Förster resonant energy transfer (FRET) mechanism is named after [60, 64]. In his 1946 work with the translated title 'Energy migration and fluorescence' [58] Förster uses the assumption that the coupling interaction between donor and acceptor is of Coulombic dipole-dipole nature. Furthermore, he was first to notice the importance of taking into account the spectral overlap between donor fluorescence and acceptor absorption.

The idea of treating energy donor and acceptor molecules as interacting dipoles was earlier introduced by Jean and Francis Perrin [65, 66]. Concentration-dependent luminescence depolarisation effects in viscous solutions were experimentally observed [67, 68] and puzzled the field as the prevailing understanding of EET at the time of this observation could not satisfactorily explain the observed phenomena. Depolarisation occurred with increasing concentration of the molecules in the solution. This suggests that once the molecules are within a critical distance of each other, the excitation energy is transferred very effectively, which could not be explained by means of trivial transfer [64]. However, the interaction radii that were predicted by F. Perrin [66] to explain the effect by dipole-dipole based transfer did not agree with the concentrations at which the depolarisation was measured. Förster improved the approach and was able to reproduce the critical concentrations by considering the spectral overlap J between donor fluorescence and acceptor absorption [30]. Even if the emitting and absorbing molecules are identical, their emission and absorption peaks are shifted by the Stokes shift [13], which needs to be considered for EET events.

Using the notation introduced in Eq. 2.7, Förster's assumption of the coupling strength as Coulombic interaction between donor and acceptor and considering the

dipole term only, leads to the following expression for the coupling strength [30, 63]:

$$V_{da} = \frac{\mu_d \mu_a}{R_{da}^3} \kappa \tag{2.10}$$

where $\boldsymbol{R_{da}}$ denotes the donor-acceptor separation vector, $\boldsymbol{\mu_{a,d}}$ are the unitary transition dipole vector moments of the acceptor and donor respectively and

$$\begin{aligned} \kappa &= \boldsymbol{\mu_d} \cdot \boldsymbol{\mu_a} - 3(\boldsymbol{\mu_d} \cdot \boldsymbol{R_{da}})(\boldsymbol{\mu_a} \cdot \boldsymbol{R_{da}}) \\ &= 2\cos(\theta_d)\cos(\theta_a) + \cos(\phi)\sin(\theta_d)\sin(\theta_a) \end{aligned} \tag{2.11}$$

is the orientation factor accounting for the relative orientation of the transition dipole moments. κ takes values ranging from 0 for perpendicular arrangement and 2 for collinear alignment and a value of 2/3 for a random orientation of the dipoles [13, 61, 64]. For the definition of the angles see Fig. 2.4. Since the orientation factor vanishes for perpendicular arrangement, no FRET is expected in this case. Such behaviour was indeed observed by DeMember *et al.* [69] who studied EET between fluorene and p-dimethoxybenzene, which were attached to a rigid frame and thereby incorporated into one molecule in which perpendicular arrangement between donor and acceptor dipoles was achieved.

The rate of FRET can now be expressed in a simple form as

$$k_{da}(R_{da}) = \frac{1}{\tau_d}\left(\frac{R_0}{R_{da}}\right)^6 \tag{2.12}$$

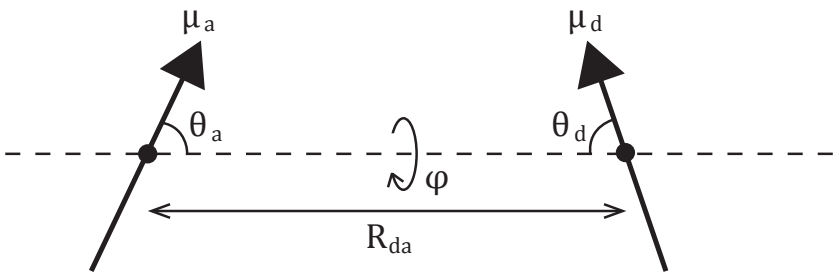


Figure 2.4: Illustration of the relative orientation of the dipole moments of the donor and acceptor $\mu_{a,d}$ and the angles as used to calculate the orientation factor κ as in Eq. 2.11. (In adaptation to Refs. [13, 61].)

where τ_d denotes the donor excitation lifetime in absence of the acceptor, R_{da} the donor-acceptor separation and

$$R_0 = \left(\frac{9 \ln(10) \kappa^2 \phi_d}{128 \pi^5 N_A n^4} \int I_d(\lambda) \epsilon_a(\lambda) \lambda^4 d\lambda \right)^{1/6} \tag{2.13}$$

is the *Förster radius*, which denotes the donor-acceptor separation at which there is equal probability for the excitation to spontaneously decay or to be transferred from the donor to the acceptor [58, 64, 70]. R_0 depends on the spectral overlap J, the orientation factor κ, the quantum yield of the donor fluorescence ϕ_d in absence of an acceptor and the refractive index n and is found to take on values in the range of 1 to 10 nm [64].

Förster's simple approximation is called *point-dipole approximation* [61, 63] since the involved molecules are represented by a point dipole fixed at the centre of the molecule. The approximation was originally developed in the context of solutions where the distance between the donor and acceptor is large compared to the size of the molecule [71] and has since been further developed.

2.3.2 Refined Models of FRET

The point-dipole approximation and formalism as introduced by Förster is widely used to explain and quantify energy transfer [64]. The model has been developed and adapted to account for more complex situations, such as different molecular shapes and a variety of sample geometries. Advanced models to simulate FRET for distinct molecular shapes have been introduced:

The *line-dipole model* is a refinement of the point-dipole approach, which was first implemented by Grage *et al.* [72] to model FRET in a thin polymer film. The principal idea of this approach is that the transition dipole moments of the donor and acceptor are not approximated to a point-dipole but are distributed on sub-dipoles throughout the molecule. The total transition dipole moments of the donor and acceptor are partitioned onto sub-dipoles through a sinusoidal function [63] such that

the polymer is represented by a one-dimensional, periodic but limited chain. The refined model has successfully been used to describe FRET for example along chains of thiophene polymers in solution [73] and in perylene-bisimide donor-acceptor systems arranged in linear and orthogonal geometry [74]. A comparison study by Beenken and Pullerits [63] contrasting four methods to model FRET including quantum-chemical approaches concludes that the line-dipole model can offer an "attractive compromise" between the accuracy of the model and the calculation effort needed.

A further extension to the line-dipole model was applied by Schmid *et al.* [75–77] to correct for the effect of excitonic self-localisation of the donor wavefunction along a π-conjugated molecule. Their work highlights the limitations of the line-dipole model (overestimating the coupling) as well as the point-dipole approximation (underestimating the coupling) in FRET modelling for well-defined supramolecular chains of extended conjugated molecules [75, 77]. Compared to the standard line-dipole model, the adapted line-dipole model uses a different wave function to calculate the electronic coupling, which allows for localisation of the donor or acceptor state. Parkinson *et al.* [78, 79] used a similar approach to model FRET in biomimetic molecular nanorings. They assumed the acceptor state on the nanoring to be localised over a number of porphyrin units and were able to simulate the experimentally observed independence of energy-transfer rates on nanoring size [78].

Another possibility to simulate FRET is to use quantum chemical methods, involving simulations at a quantum chemical level where the above introduced methods use approximations. An in-depth treatment can be found in [80]. The point dipole approximation averages away the local characteristics as size and shape of the two interacting molecules [81]. A method that gives a more atomically accurate picture is the *distributed monopole model* which was first implemented to simulate EET in chlorophylls [36]. In this model, the electronic coupling strength is evaluated based

on atomic transition "monopoles" positioned at the atomic centres [82, 83]. The "monopoles" are determined by quantum chemical calculations as the ZINDO (Zerner's Intermediate Neglect of Differential Overlap) method [84–86]. This approach has been implemented for example in rigid-rod conjugated polymers (polyindenofluorene chains endcapped with perylene monoimide derivatives) [87] and in a PHTP/2/5T host-guest system [88]. Interestingly, for the latter example it was also observed that the point dipole approximation reproduces the same results for the overall transfer rates, which was attributed to the sample geometry. The authors point out however that the point dipole approximation does not lead to the right interpretation as it overestimates interchain (as opposed to intrachain) transfer [88]. Beljonne *et al.* [40, 81] also applied the framework of the distributed monopole in their studies on intrachain and intrachain transfer mechanisms.

Krueger *et al.* [83] suggest the *density cube method* for an accurate molecular picture of the investigated system. They have used the method to investigate FRET in light-harvesting complexes LH2 of bacteria. While other methods only hold for separations between the molecules which are larger than the molecules themselves, their method can be used for any donor-acceptor distance. The key idea is to establish a grid of density cubes between which the Coulombic interaction is determined explicitly. For a sensible grid, the only limitation to this method is the precision of the wavefunctions used for ground and excited states of the molecule, which are calculated by quantum-chemical approaches.

A detailed understanding of FRET processes in conjugated systems also often includes accounting for the interplay between intrachain and interchain energy migration. Förster assumed energy transfer to happen in a one-step process after donor excitation. A more realistic model involves multiple steps, as for example

expressed by a random walk of the excitation prior to energy transfer, as was assumed in Refs. [72, 75, 87, 89].

There are different ways to distinguish between intra- and interchain transfer mechanisms: Nguyen *et al.* [90] have studied transfer rates of a conjugated polymer embedded in a silica nanostructure, which enabled a separation of components of interchain and intrachain EET. They found interchain transport to happen on a rapid picosecond time scale, whereas intrachain transport was found to occur at a few hundred picoseconds time scale. An alternative way to differentiate between the two mechanisms was implemented by Beljonne *et al.* [81] who investigated polyindenofluorenes with perylene end caps in solution and in film through time-resolved measurements and modelling of the transfer mechanisms. Comparing time-resolved measurements from both configurations enabled them to disentangle the contributions from intrachain and interchain transport. In solution, EET after photoexcitation is expected to primarily occur along the chain to the end caps whereas interchain mechanism are found to be prominent for films. In agreement with the work of Nguyen *et al.* [90], they observed fast intermolecular EET within a time scale of tens of picoseconds and much slower (nanoseconds) intrachain mechanisms. The slow process was attributed to the motion of the exciton along localised sections of the polymeric chain [81].

2.3.3 FRET in Restricted Geometries

Förster's original expression was derived for a 3-dimensional space (solution) with uniform donor and acceptor concentrations [59, 71]. As FRET has become an important tool for measuring nano-scale distances [91], the theory has been extended to different applications such as energy transfer in membrane systems [92], at polymer interfaces [93] or DNA probing [94] with a variation of sample geometries [93, 95–100].

Different theoretical approaches have been applied by several authors [95–100] to adapt and extend Förster's theory to consider the effect of varying spatial dimensions. Early work on FRET in lower dimensions was performed by Hauser *et al.* [95] who presented a theoretical treatment of FRET in one and two dimensions as well as analytical expressions for the time dependence of the acceptor fluorescence for non-interacting pairs of donors and acceptors restricted to different geometrical arrangements.

Wolber and Hudson [98] provide an analytical solution to FRET in two dimensions for the case of randomly distributed donors and acceptors in two separate planes at a fixed distance. Their general solution is widely applied in Biophysics primarily to describe energy transfer in bi-layer membrane systems [101–103].

The basis for further theoretical work was laid by two reports employing a two-particle model (interactions only between the donor-acceptor pair) and configuration averaging to derive analytical expressions for FRET in two cases: Huber *et al.* [96] developed a formalism to treat so-called "donor-donor transfer", in which FRET happens between two identical molecules. Blumen and Manz [97] presented a theoretical formalism for the case of FRET between two different molecules, called "direct trapping".

Based on these two articles, Baumann and Fayer [100] reported a unified treatment of the two cases. Their calculations are based on taking the configurational averaged probability $G(t)$ of finding an initially excited donor still excited at time t and integrating $G(t)$ over a continuous spatial distribution, which was performed for the case of intermixed donors and acceptors in two and three dimensions as well as for geometries of two-dimensional layers. $G(t)$ is linked to the donor fluorescence decay, which is a common experimental observable in investigation of FRET, through multiplication of $G(t)$ with $\exp(-t/\tau)$, where τ denotes the donor PL lifetime in absence of an acceptor. One of their main conclusions is that $G(t) \propto \exp(-t\ \theta)^{\Delta/6}$, where θ is a arrangement-specific scaling parameter and Δ denotes the spatial

dimension. This result has been successfully applied to experimental studies exploring FRET in lower dimensions [104–106].

A very similar, slightly more general expression for FRET was developed at the same time by Klafter and Blumen [99] ("KB-equation") to also take into account the effect of restricted geometries. They employ a dimensionality parameter β, which is linked to spatial dimensions as $\beta = d/6$ in case no further spatial restrictions apply but only dimensionality (β can also account for other geometrical restrictions), to describe the donor decay $I_d(t)$ as:

$$I_d(t) \;=\; e^{-t/\tau_d \;-\; p\;(t/\tau_d)^{\beta}} \tag{2.14}$$

where p is a parameter linked to the local acceptor concentration and is also depending on the dimensionality parameter β.

This formalism has been extended to also incorporate arbitrary distributions of donors and acceptors of which a derivation and overview is given in Refs. [93, 107]. As main result, the donor decay $I_d(t)$ as a function of time for energy transfer between donors and acceptors, integrated over their positions $\mathbf{r_d}$ and $\mathbf{r_a}$ within a restricted volume and heterogeneous donor and acceptor concentrations, $C_d(\mathbf{r_d})$ and $C_d(\mathbf{r_a})$, can be written as:

$$I_d(t) \;=\; e^{-t/\tau_d} \int_V C_d(\mathbf{r_d})\; \varphi(t, \mathbf{r_d})\; d\mathbf{r_d} \tag{2.15}$$

with:

$$\varphi(t, \mathbf{r_d}) \;=\; \exp\!\Big(-\int_V C_a(\mathbf{r_a})\; [1 - e^{-t\;\; k(|\mathbf{r_a}-\mathbf{r_d})|}]\; d\mathbf{r_a}\Big). \tag{2.16}$$

Equations 2.15 and 2.16 have been further specified for systems with planar symmetry [108, 109], spherical symmetry [109, 110] and cylindrical symmetry [111].

3 Experimental Methods

Contents

3.1 Steady State PL Spectra 28
3.2 PL-Upconversion 29
3.2.1 Operating Principle 29
3.2.2 Measurements 32
3.3 Time-Correlated Single Photon Counting 35
3.3.1 Operating Principle 35
3.3.2 Measurements 37
3.3.3 Time Resolution 37
3.4 Fourier Transform Infra-Red Spectroscopy 39
3.4.1 Operating Principle 39
3.4.2 Measurements 41

This chapter introduces the experimental techniques which were applied on various samples throughout this thesis. The chief aim of applying these techniques was to gain deeper insights into the fundamental photonic properties of organic semiconductors. The optical phenomena used for investigation are absorption and photoluminescence (PL). The experimental techniques which are based on these two phenomena can be categorised either as steady-state/time-integrated techniques or as time-resolved techniques. Steady-state PL measurements are described in Section 3.1. Steady-state absorption, for which Fourier-transform infrared (FTIR) spectroscopy was employed, is described in Section 3.4. Time-resolved spectroscopy in addition offers a powerful tool to study excitation lifetimes, radiative and non-radiative decay rates, spectral dynamics and energy transfer phenomena [112]. The time-resolved PL spectroscopy techniques used throughout this work are PL-upconversion, which is outlined in Section 3.2 and time-correlated single photon counting (TCSPC), which is described in Section 3.3. Together, these two time-resolved techniques enable investigation of a time range of 300 fs [113] to several ns [114].

3.1 Steady State PL Spectra

The time-integrated PL spectra presented in this thesis were recorded with the set-up shown in Figs. 3.2 and 3.4 (a more detailed description is given in Section 3.2.2.1). The sample is excited with pulsed laser light at a suitable wavelength within the ranges 690 to 1040 nm and 395 to 500 nm (frequency doubling). PL from the sample is focused onto a Jobin Yvon Triax 190 spectrograph, dispersed and subsequently collected with a nitrogen-cooled Jobin Yvon Symphony CCD (charge coupled device) silicon detector. Optical filters are added before the spectrograph, carefully selected for each case to ensure blocking of the excitation laser light but not the sample PL. An irradiance standard lamp (Seasoned Quartz Tungsten Halogen Lamp OL 245U from Precision Photometrics) with a known emission spectrum is used for spectral

calibration. The measured emission spectra are influenced by the optical filters and the wavelength dependent response of the spectrograph as well as the response of the CCD [33]. The PL intensity of the measured sample PL $I^{meas}_{sample}(\lambda)$ therefore needs to be corrected to $I^{corr}_{sample}(\lambda)$ as:

$$I^{corr}_{sample}(\lambda) = \frac{I^{0}_{lamp}(\lambda)}{I^{meas}_{lamp}(\lambda)} I^{meas}_{sample}(\lambda) \tag{3.1}$$

with the known lamp spectra $I^{0}_{lamp}(\lambda)$ and the lamp spectra measured under the sample measurement conditions $I^{meas}_{lamp}(\lambda)$.

3.2 PL-Upconversion

PL-upconversion spectroscopy enables ultrafast measurement of PL dynamics with a femtoseconds range time-resolution, allowing experimental investigation of energy transfer dynamics [78, 113, 114].

3.2.1 Operating Principle

The technique is based on frequency mixing in a non-linear dielectric material (optical gating) [115]. A sample is excited with an ultrafast laser pulse. The thereby emitted PL and a second synchronous "gate" pulse are overlapped within a non-linear crystal. This leads to the creation of sum-frequency photons, which are then recorded by a detector [112]. Since the frequency of the gate pulse is added to the signal from the sample PL, the signal is said to be "upconverted".

3.2.1.1 Non-linear Optics

The effects of sum-frequency generation (SFG) to upconvert the sample PL and of second harmonic generation (SHG) to double the laser output frequency rely on second order non-linear optics. The following discussion of their underlying physics is based on Refs. [112, 116, 117].

In standard treatment of optical processes, the electrical polarisation of a medium is assumed to be linearly dependent on the applied electric field E and is commonly written as:

$$P_{linear} = \epsilon_0 \chi E \tag{3.2}$$

where χ denotes the conventional electric susceptibility and ϵ_0 is the vacuum permittivity. For simplicity in notation, the direction of polarisation and of the applied electric field are here assumed to coincide. However, if strong electric fields are applied to the medium, as this is the case for high power laser pulses, higher powers of the electric field intensity start to dominate the expression for the polarisation response of the material, which thus can be written as a series expansion:

$$P_{non-linear} = \epsilon_0 \chi E + \epsilon_0 \chi_2 E^2 + \epsilon_0 \chi_3 E^3 + ... \tag{3.3}$$

whereby the tensor nature of the susceptibility is neglected and χ_i are the material dependent higher order susceptibilities. Expressing Eq. 3.3 explicitly for the case of two incident waves with frequencies ω_1 and ω_2, several second order terms appear as a function of ω_1 and ω_2 and give rise to a range of non-linear effects including SHG and SFG for a non-vanishing second-order susceptibility χ_2. Exhibiting a non-vanishing χ_2 requires for a material to be non-centrosymmetric which is for example the case for beta-barium-boronate (BBO) crystals.

SHG is applied to double the frequency of the laser beam. In this case, the incident waves are at the same frequency ω. SHG is driven by a 2ω term in the explicit expression of the second-order polarisation, implying that the re-radiated light from the non-linear medium includes a component at twice the fundamental frequency. Refractive index matching ($n_1 = n_2$) is required to avoid destructive interference of the 2ω-waves as they are created throughout the crystal. The refractive index n of a non-isotropic crystal is a function of polarisation of the incident light and the direction of propagation of the fundamental and secondary waves with respect to the

optical axis and each other. This is additionally a function of frequency. In practice, the polarisation of the fundamental wave has to be aligned to the optical axis of a uniaxial crystal. The exact angle of the crystal has to be carefully optimised for each desired wavelength to obtain efficient SHG.

For SFG, the decisive term in the non-linear polarisation is a function of $(\omega_1 + \omega_2)$, leading to the creation of sum-frequency photons in the non-linear material. To achieve SFG, the condition of phase matching needs to be satisfied:

$$\vec{k}_1 + \vec{k}_2 = \vec{k}_3 \tag{3.4}$$

where $\vec{k}_{1,2}$ denote the wavevectors of the incident light (sample PL and gate pulse, respectively for PL-upconversion) and $\vec{k_3}$ denotes the wavevector of the upconverted light. The phase matching condition is depicted in Fig. 3.1. For the corresponding wavelength λ_3, resulting from upconverting sample PL at λ_1 with a gate pulse at λ_2, Eq. 3.4 implies:

$$\lambda_3 = \left(\frac{1}{\lambda_1} + \frac{1}{\lambda_2}\right)^{-1}. \tag{3.5}$$

Similar to the case of SHG, the crystal orientation plays a crucial role and only a narrow range of wavelengths can be upconverted at a given crystal angle. For each experiment, this requires precise information about the sample PL and using the right non-linear crystal and setting its angle accordingly.

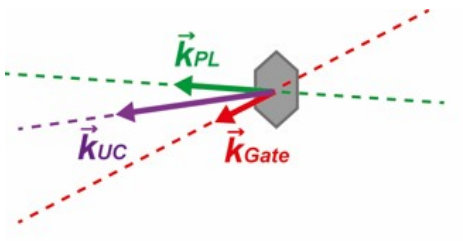


Figure 3.1: Phase matching condition to achieve SFG for the wavevectors of the sample PL $\vec{k}_{PL}$, the gate beam $\vec{k}_{Gate}$ and the resulting upconverted signal $\vec{k}_{UC}$ within a BBO crystal. Further criteria to obtain an upconverted signal are temporal and spatial overlap.

3.2.2 Measurements

3.2.2.1 Set-up

The set-up used for all PL measurements (steady-state PL spectra, TCSPC and PL-upconversion) is depicted in Fig. 3.2. In the following, the general set-up as used for PL-upconversion measurements is described. Adjustments made for the other measurement techniques are mentioned in the respective descriptions.

A wavelength-tunable mode-locked Mai Tai Ti:Sapphire laser at a repetition rate of 80 MHz with a pulse duration of 80 fs is employed as the light source. The light is directed to a beamsplitter, where the beam is split into a gate beam (red) and a pump or excitation beam (blue). A halfwave-plate before the beamsplitter allows for adjusting the power directed to each beam. The wavelength range of the Ti:Sapphire laser is 690 to 1040 nm and can be extended to 345 to 500 nm through frequency doubling with a BBO crystal (BBO1) in the pump beam path. After the BBO, a Glan-Thompson polarizor and a filter (F1) are used to block any residual light at the fundamental wavelength. The pump beam is then focused onto the sample position after passing a combination of halfwave-plate and Glan-Thompson polarizor, which enables excitation power adjustments as well as polarisation-dependent sample excitation and measurements.

Once the sample is excited, sample PL (green) is collected through off-axis parabolic mirrors, which are used to avoid chromatic and spherical aberrations and temporal dispersion [112, 118]. The sample PL is focused onto the upconversion BBO crystal (BBO2) and beforehand passes another filter (F2) to block any residual light from the pump beam.

The gate beam (red) after the beamsplitter is directed onto a movable delay stage. Again, a halfwave-plate and a Glan-Thompson polarizor, ordinarily set to vertical polarisation of the beam, positioned in the gate beam path before the delay stage can be used for polarisation-dependent measurements. Through moving the delay

stage within the direction of the beam and thereby prolonging or shortening the beam path, the temporal delay of the gate beam is controlled.

The gate beam and sample PL are both focused onto the upconversion BBO crystal (BBO2) in the upconversion box, which is mounted on a rotation stage to control its angle. Sum-frequency ("upconverted") photons are created when the gate and PL pulses overlap temporally and spatially at the correct wavelength-dependent crystal angle. Once this is achieved, the upconverted signal is filtered for residual light at wavelengths of sample PL and gate beam (F3 and slit) and then collected and dispersed in a spectrograph. Finally, the signal is detected by a nitrogen-cooled CCD silicon detector, set to the wavelength of the upconverted signal (see Eq. 3.5).

The fundamental limit of the time-resolution of the upconversion-system is the pulse duration. However, there will be temporal broadening due the finite width of the non-linear crystal used for "upconverting" the signal, which causes the group velocity to disperse [119]. The upconversion system used for this thesis has a time-resolution of approximately 300 fs [113].

3.2.2.2 Experimental Details

For the PL-Upconversion measurements, a BBO crystal of 1 mm thickness cut at a 35° angle was used. The mixing angle between the gate beam and the sample PL in the set-up is 12°. The phase-matching condition in Eq. 3.4 was met by rotating the BBO crystal mounted on a computer-controlled rotation stage. For PL delay measurements an angle scan (crystal angle versus signal strength) was taken and the rotation stage was set to the angle of maximum signal.

PL delay scans can be recorded scanning the time (i.e. moving the delay stage) forwards or backwards. Taking multiple scans in both scanning modes is beneficial: In addition to obtaining better accuracy of the measured data, it allows for monitoring of sample stability during the experiment (e.g. for effects of photo-oxidation).

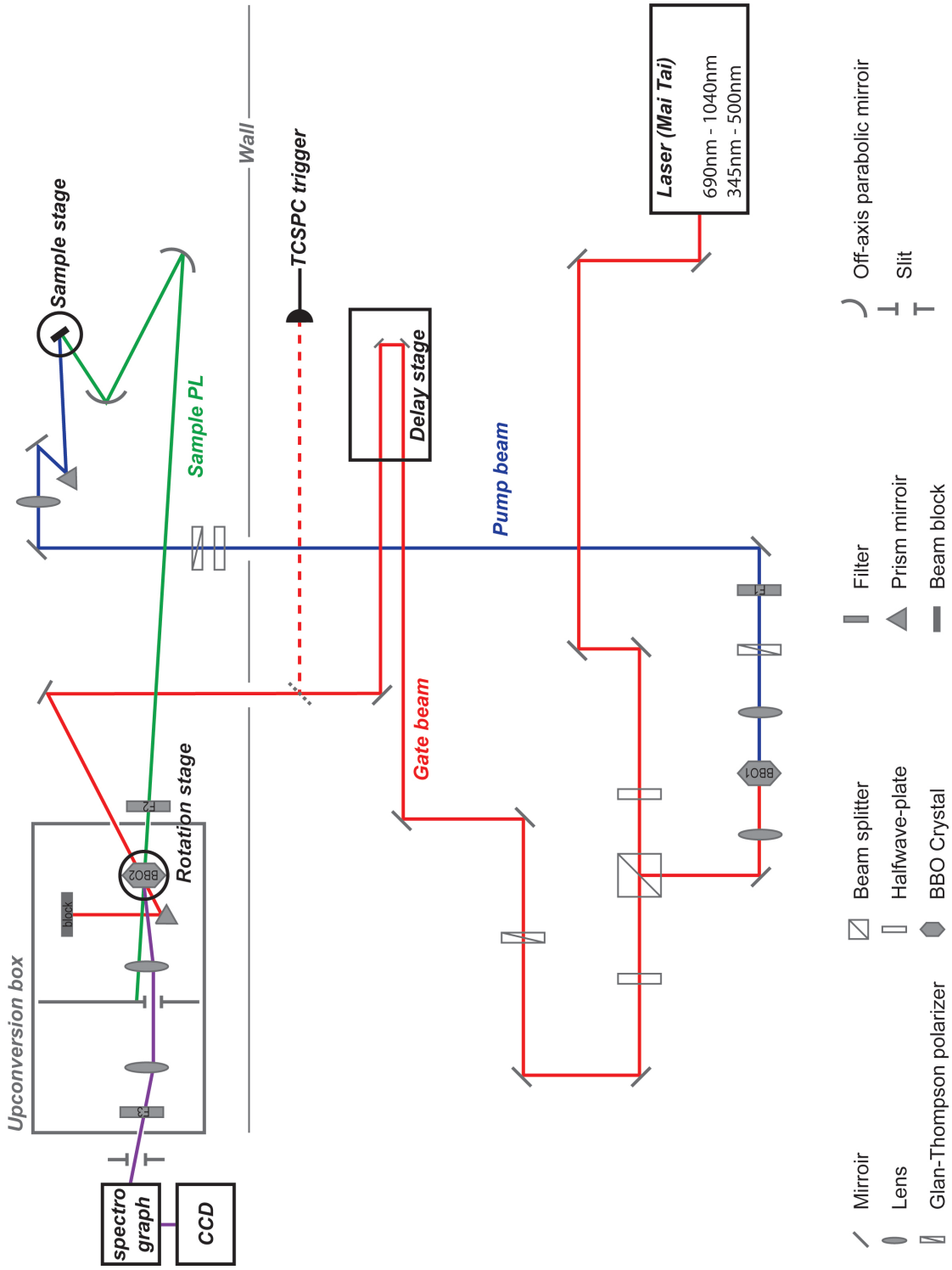


Figure 3.2: Schematic overview of the PL-Upconversion set-up. In-detail description is provided in the text.

3.3 Time-Correlated Single Photon Counting

TCSPC is an effective and well-established measurement technique to obtain information on wavelength-dependent PL dynamics at a timescale that ranges from tens of picoseconds to nanoseconds [33, 112, 120, 121].

3.3.1 Operating Principle

TCSPC is based on repetitively recording the time-delay between sample excitation and the emission of a single photon at a specific energy/wavelength by the sample resulting from the excitation. The histogram of photon counts versus time-delay represents the intensity of the PL decay following excitation as a function of time [33, 121]. In practice, the sample is excited with a pulsed light source and the time-delay between a reference trigger pulse from the light source and the arrival of a photon at the detector is recorded through a time-to-amplitude converter (TAC), which converts the time between start and stop pulse into voltage [120]. The reference trigger pulse and the arrival of a single PL photon therefore respectively act as start and stop signals. The general working principle of TCSPC is depicted in Fig. 3.3. Since the TCSPC technique relies on counting single photon events, photons are collected over a large number of pulse cycles to obtain significant data. The sample excitation is thereby kept low, such that at most one photon is registered per cycle to ensure a correct representation of the PL dynamics (typically 0.01 to 0.1 photon events per cycle [120]). The arrival of two emitted photons at the detector in one cycle would lead to an over-representation of the early photons in the decay statistics (so-called “pile-up effect”) [33, 112]. For the majority of pulse cycles, no photon is detected. Many systems therefore operate in a reverse start-stop configuration in order to avoid resetting the TAC in every cycle; the arrival of the photon at the detector starts the time measurement in the TAC and the next reference trigger pulse from the light source stops it [120].

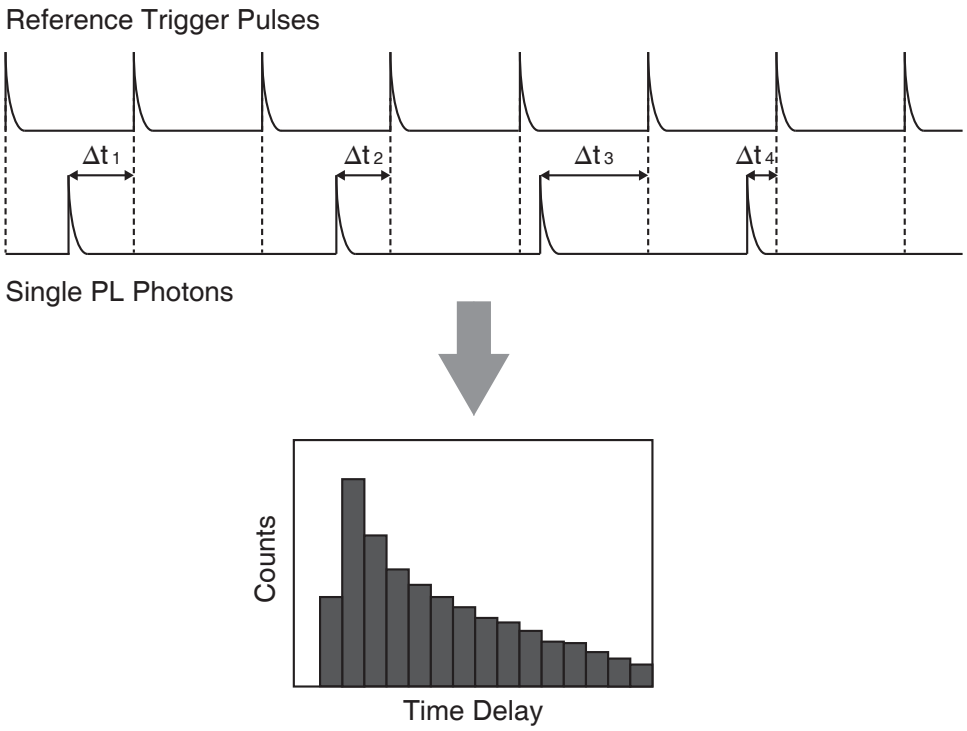


Figure 3.3: Principle of TCSPC measurements: The time-delay between single photons from the sample PL arriving at the detector and a reference trigger pulse is recorded over many cycles. The histogram of counts versus time-delay portray the PL dynamics. (Adapted from [112].)

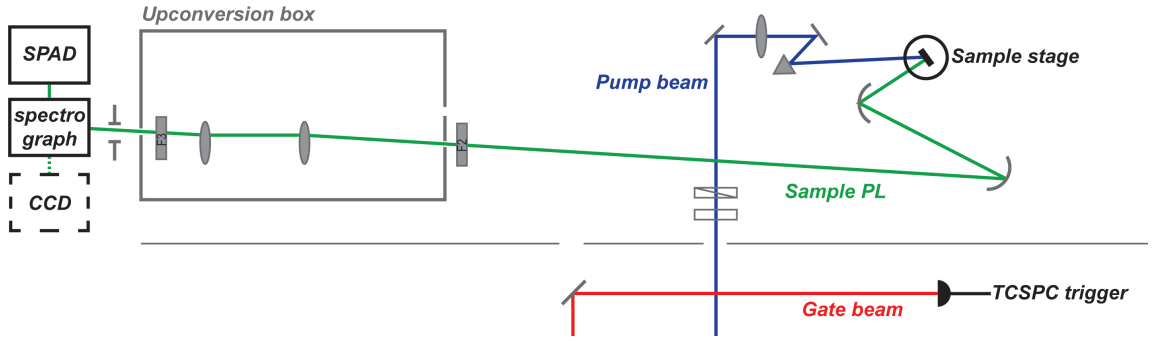


Figure 3.4: Part of the set-up (cf. Fig. 3.2, where also a full legend can be found) as adjusted for TCSPC (solid line after the spectrograph, signal going to the SPAD) or PL (dashed line after the spectrograph, signal going to the CCD detector). Description in the text.

3.3.2 Measurements

The part of the set-up (cf. Fig. 3.2) that is adapted for TCSPC is shown in Fig. 3.4. The gate beam, which is split off from the pulsed excitation laser beam, is redirected with a mirror to a pn-diode (battery-biased high speed silicon photodetector, Newport 818-BB-21) acting as the TCSPC reference trigger. The sample PL is directly focused onto the spectrograph and collected with a SPAD (Single Photon Avalanche Detector, PDM Series, PiqoQuant), which is highly sensitive and allows for the detection of single photons. Within the detector, the optical PL signal is converted into an electrical pulse and sent to the TCSPC module. As for steady-state PL measurements, filters are used to block light at the excitation wavelength before the spectrograph. Excitation and detection wavelengths were chosen for each experiment separately. The measurement time over which the counts versus time-delay were recorded was also adjusted for each sample. For luminescent polymers, such as the ones studied in Chapters 4 and 6, the measurement times range from tens of seconds to several minutes. For the weakly emitting porphyrin nanorings studied in Ref. [122], the measurement time was set to 8 h. Background scans were taken and subtracted for all measurements.

3.3.3 Time Resolution

The time resolution of a TCSPC system is identified by the instrumental response function (IRF), which can be measured by directly detecting the laser pulse and whose ideal shape would be a δ-function [121]. The time-resolution is influenced by the pulse width and temporal dispersion in the optical system, but most broadening of the IRF is caused by the transit time spread in the detector and timing jitter in the electronics [33, 120, 121]. The finite broadening of the IRF means that the measured decay distribution actually corresponds to the convolution of the fluorescence decay function with the IRF [120]. In practice, however, deconvolution is complex and is usually neglected for lifetimes that well exceed the width (understood as FWHM; full width

half maximum) of the IRF [120, 123]. The IRF of the system used for the TCSPC measurements throughout this thesis, measured at 810 nm, is depicted in Fig. 3.5.

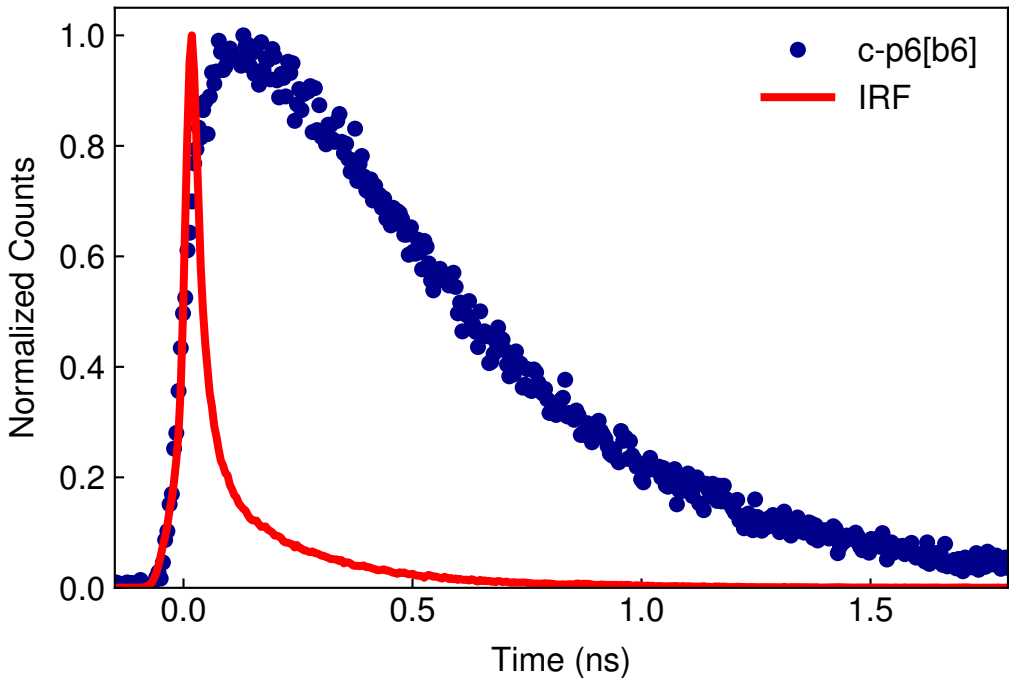


Figure 3.5: Normalised TCSPC traces from a six-porphyrin nanoring with butadiyne linkages (c-p6[b6], blue circles) plotted with the normalised system IRF (red line). The sample was excited at 810 nm and TCSPC traces were recorded at 1050 nm. The IRF of the TCSPC set-up was measured at 810 nm with a roughened quartz disk. Depicted data is taken from work published in [122].

3.4 Fourier Transform Infra-Red Spectroscopy

3.4.1 Operating Principle

FTIR spectroscopy is used to determine molecular absorption. The technique is based on creating interference between two light beams and on Fourier transformation for frequency decomposition of a raw signal. Most FTIR set-ups include a Michelson interferometer for the generation of interference. Within a Michelson interferometer, a collimated light beam is divided into two paths on which a path difference is introduced before the paths recombine again at which point interference between the two beams can result [124, 125].

The working principle of a FTIR with a Michelson interferometer and a sample compartment that allows for measurement of transmission and reflection from a sample by rotating the position of a mirror is depicted in Fig. 3.6. In a typical set-up, the division of the light beam into two paths is achieved with a beamsplitter, which partially reflects and transmits the incoming beam. One beam is directed to a movable mirror (in the direction of the light beam) to adjust the path difference and the other beam is directed to a fixed mirror [126]. The interference of the two reflected beams occurs at the beamsplitter. From there, the light with an intensity resulting from the interference is (partially) directed to the sample position [124]. After the sample, a detector registers the light intensity of either the sample reflected or transmitted light versus the position of the movable mirror. The thereby obtained spectral information stems from all wavelengths simultaneously [127]. By mathematically Fourier transforming the detected signal a spectrum of light intensity versus wavenumber is obtained [124, 125], from which sample absorption can be deduced as described in the following section.

The main advantages FTIR spectroscopy offers over dispersive spectroscopy are an improved signal-to-noise ratio and significantly faster spectra acquisition [127].

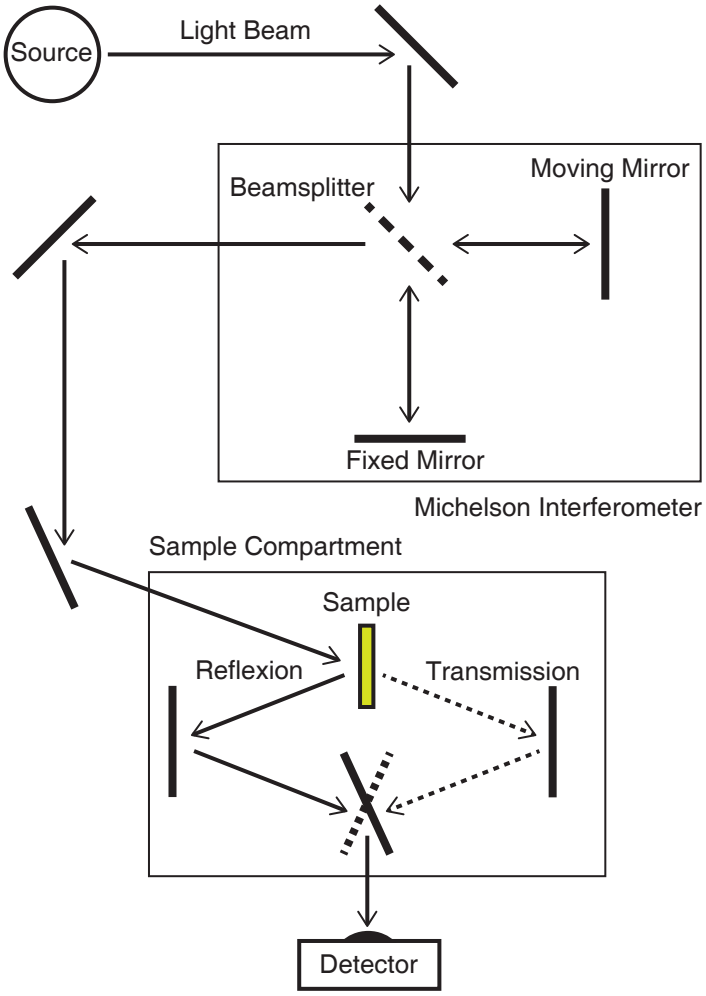


Figure 3.6: Schematic working principle of a FTIR with a Michelson Interferometer and a sample compartment built for reflection and transmission measurements. Description in the text. (Abstracted from the beam path of the Bruker VERTEX 80v FTIR system [126].)

3.4.2 Measurements

Employing a FTIR spectrometer, transmission and reflection measurements can be performed for each sample of interest, which are then used to obtain the sample absorption (absorbance/O.D.). For that purpose, the fractions of the total (100%) transmission and reflection are of interest, which are obtained through referencing. Total transmission is assumed for an empty sample position. Depending on the nature of the sample, this is achieved if only the sample holder (in case of a thick film) or the sample's substrate (in case of a thin film) or the sample's container (in case of a solution) is placed into the system. For total reflection, a mirror with known reflectivity is used. In addition to the referencing, the measured reflection from the empty sample position and the measured transmission from the mirror are used to correct for any background light. Fractional transmission (T) and reflection (R) of the sample are then obtained as:

$$T = \frac{T_{sample} - T_{mirror}}{T_{empty} - T_{mirror}} \quad \text{and} \quad R = \frac{R_{sample} - R_{empty}}{R_{mirror} - R_{empty}}, \tag{3.6}$$

where $T_{sample/empty/mirror}$ are the measured transmissions from the sample, the empty sample position and the mirror, respectively and $R_{sample/empty/mirror}$ the corresponding measured reflections. The (napierian) absorbance is obtained from $T(\lambda)$ and $R(\lambda)$ as a function of wavelength λ as:

$$A(\lambda) = -\ln \frac{T(\lambda)}{1 - R(\lambda)}. \tag{3.7}$$

The referencing and correction for background light does not take into account any light scattering from the sample. If light scattering from the sample becomes relevant, measurement techniques that use an integrating sphere need to be considered. A different experimental system with an integrating sphere was used for the absorption measurements presented in Chapter 4.

The specific system that was used to obtain the absorption spectra presented in Chapters 6 and 7 was a Bruker VERTEX 80v FTIR spectrometer with a CaF_2 beamsplitter. A tungsten halogen lamp and a deuterium lamp were used as light sources. For detection, a gallium phosphide (GaP) and a silicon (Si) diode detector were employed. For referencing of the transmission, a silver and an aluminium mirror with specified reflectivity were placed in sample position: the UV-protected silver mirror (Thorlabs) in combination with the tungsten halogen lamp and the silicon detector and the UV-enhanced aluminum mirror (Thorlabs) in combination with the deuterium lamp and the GaP detector. As reflection reference, a z-cut quartz substrate was used.

4

Influence of β-phase Content on Chain Conformation in PFO Films

Contents

4.1 Background and Motivation 44
4.2 Sample Preparation 47
4.3 Experimental Details 49
4.3.1 Absorption 49
4.3.2 PL 50
4.3.3 PLQE 50
4.3.4 TCSPC 50
4.4 Results 51
4.4.1 Absorption 51
4.4.2 Time-Integrated PL 56
4.4.3 PLQE and Decay Rates 59
4.5 Discussion 63
4.6 Summary and Conclusion 68

Reproduced in part from work published by Eggimann et al. in Ref. [114].

4.1 Background and Motivation

One widely explored polymer in the context of promising semiconducting conjugated polymers is PFO (poly(9,9-dioctylfluorene) $(C_{29}H_{42})_n$, chemical structure depicted in Fig. 4.1), a member of the family of fluorene-based polymers that have found widespread use in a range of applications including organic light emitting diodes (OLEDs) [128–130], transistors [131], and lasers [132, 133]. PFO features desirable photo- and electroluminescence [129, 134, 135] as well as high optical gain and respectable charge-carrier mobilities [136].

PFO is known to adopt two distinct phases, namely the disordered "glassy" phase and the more crystalline β-phase [137–141] which differ by the angles adopted between neighboring fluorene units. For the glassy phase, these angles vary randomly within a large spread of possible values with an average value of 135°, while they take a set value of 180° in the β-phase, corresponding to a coplanar, extended and more rigid chain conformation [138, 141]. The two phases of PFO with their difference in torsion angles between the flourene units are depicted in Fig. 4.1. An important role for the formation of the two phases is played by the alkyl side chains (C_8H_{17}, c.f. Fig 4.1) on the polyfluorene backbone and the van der Waals interactions between them as their arrangement around the backbone is decisive for the formation of either the glassy or the β-phase within PFO [142].

Inclusion of polymer chains that have adopted β-phase conformation appears to have a beneficial impact on optoelectronic properties of PFO films, including for example improved spectral stability for emission [143] and efficient photoluminescence (PL) [130, 135].

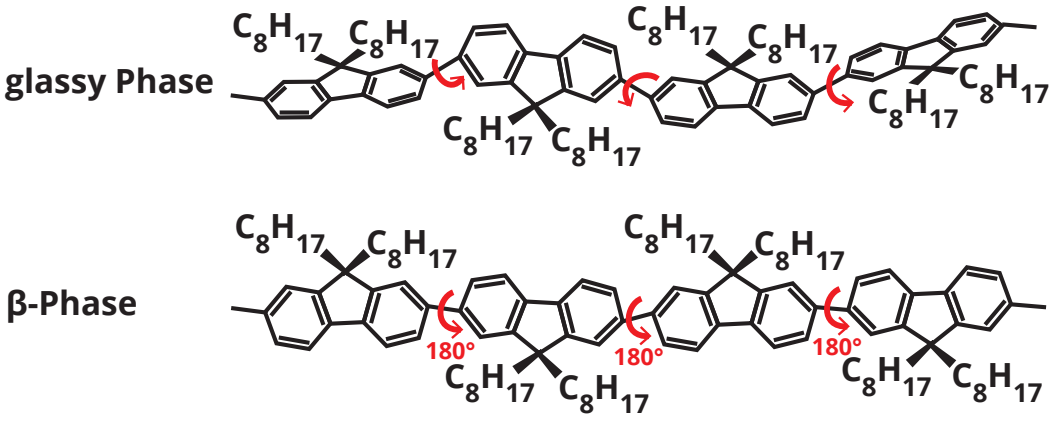


Figure 4.1: Chemical structure of poly(9,9-dioctylfluorene) $(C_{29}H_{42})_n$ adapting glassy (top) and β- (bottom) phase. The torsion angles between the fluorene units (depicted with sidechains) vary randomly for the glassy chain conformation and take a value of 180° in β-phase chain conformation (depicted in red).

High photoluminescence quantum efficiency (PLQE) is an essential requirement for the efficient use of conjugated polymers as light emission materials in display, lighting, and laser applications. A better understanding of the fundamental material properties determining PLQE is therefore of great importance. PFO provides a versatile platform for such studies in the wider context of polyfluorenes, given the variation in polymer chain conformations that can be induced and explored. The introduction of some β-phase extended chain segments in PFO films has been found to improve emission performance [129, 130, 134, 135]. Moreover, it has been observed that the PLQE of PFO films strongly depends on the fraction of β-phase chain segments contained [130, 135], with a record high PLQE measured for modest fractions ($\sim$ 5-15%) of β-phase [130, 135, 144]. Possible factors suggested for the dependence on β-phase content include alterations in film microstructure [145, 146] and chain conformation, changes in the energy transfer mechanisms [144, 147, 148] and their potential interplay [149]. However, these studies suffer from the use of different preparation methods employed along a series of films within a given range of β-phase fractions, which may have resulted in an undesirable influence of altered microstructure and defect content on

PLQE [135]. The use of one single preparation technique throughout the series is therefore crucial to clearly isolate and investigate the effect of β-phase content on optoelectronic properties. For the study presented here, this is achieved by employing a novel technique proposed by Zhang *et al.* in 2017 [130], which uses paraffin oil as an additive to the solutions of polymer in toluene from which thin films are produced via spin casting.

In this chapter, effects of the fraction of β-phase chains present in PFO thin films on the nature of the electronic states of the polymer, chain conformation and PLQE are explored. To ensure consistency of results, the PFO films with varying content of β-phase were prepared through one single preparation method. Changes in the electronic states and film microstructure are probed by examining emission and absorptance spectra of films with varying β-phase fraction. The main question addressed in this chapter is: ***How does variation in β-phase content influence chain conformation and PLQE in PFO thin films?***

4.2 Sample Preparation

For the studies in Chapters 4 and 5, a series of thin films of PFO with varying content of β-phase chain segments was prepared[1]. For the fabrication process, a technique proposed by Zhang *et al.* [130] was applied, which uses paraffin oil as an additive to the solutions of polymer in toluene from which thin films are spun cast. The small amounts of paraffin allow tuning of the fraction of β-phase content in the film (here: between 0% and 25.6%). Importantly, this method enables the fabrication of a series of PFO films with considerably varying β-phase content through one single technique. Such an approach is decisive for the comparability of measurements from films with a range of β-phase content, which has been identified as a concern in previous studies [135].

The polymer was received from Cambridge Display Technology and has a peak molecular weight of $M_p = 133\,000\,\mathrm{g\,mol^{-1}}$. The PFO thin film samples were deposited on pre-cleaned quartz substrates by spin-coating at a speed of 2000 rpm for the duration of one minute. Both, solutions and substrates, were pre-heated at 80 °C for 5 minutes immediately prior to deposition. Following deposition, the substrates were annealed for 1 minute at 120 °C to remove any traces of solvent. The β-phase chain segment fractions were tuned from 0% (all glassy phase) to 25.6% (as demonstrated in Ref. [130]) by adding 100 µL aliquots of increasing concentration (0 to 80 µL per mL) of paraffin oil (Edwards Ultragrade 19) in toluene solutions to 1.9 mL portions of a baseline 13.5 mg per 1 mL PFO in toluene solution. This procedure yields mixtures with 0 to 0.4 vol% paraffin oil.

Film thickness was measured[1] for each film using a Dektak profilometer (Table 4.1). The percentage of β-phase chain segments in the films is also listed in Table 4.1 and has been determined[1] for each sample from the film thickness and from weighted (in

[1] PFO sample fabrication, thickness measurements and β-phase determination were performed by Florian Le Roux.

order to correct for different oscillator strength) integrated absorptance contributions from the glassy- and β-phase chain segments [139, 150] (cf. Section 4.4.1).

In between measurements, the films were kept in a nitrogen filled glovebox. To ensure the stability of the samples over the time span they were investigated, PL measurements were performed after each experiment. The spectral shape of the PL differs considerably with changing β-phase content (cf. Section 4.4.2) and was therefore considered as a good indicator for conformational changes within the films that may have occurred over time. The films containing some β-phase ($\geq$ 6.4%) phase showed good stability and no changes under measurement conditions (i.e. laser illumination) were observed. For the PFO films containing zero to very low ($\leq$ 0.5%) β-phase (henceforth called "glassy films"), it was observed that the PL spectra showed contribution of β-phase chain segments after a few hours of low-fluence laser illumination at 405 nm. In order to circumvent this problem, the long measurements for the glassy sample in Chapter 5 was performed on a fresh sample and therefore only data from measurements for which the PL shape before and after the measurement agrees are presented here. Sample 4 was partially damaged after the PLQE measurement. Consequently, no time-resolved could be measured for this sample.

Table 4.1: Overview of samples with β-phase content and thickness t.

Sample Name	**β-phase** (%)	**t** (nm)
Sample 1	0	131
Sample 2	ca 0	139
Sample 3	0.5	130
Sample 4	6.4	125
Sample 5	7.4	122
Sample 6	10.9	126
Sample 7	12.4	134
Sample 8	14.0	134
Sample 9	18.6	137
Sample 10	22.4	130
Sample 11	24.5	125
Sample 12	25.6	135

In addition to the 12 samples presented above, the same method was used to fabricate samples with higher β-phase content. However, vol% of paraffin oil in excess of 0.75 vol% led to the fabrication of soft polymer films whose large surface roughness and poor consistencies made the films unsuitable for optical measurements. This threshold might be attributed to a quantity of paraffin oil in solution large enough to hinder the spin-coating process. An intermediate 13th sample with a β-phase content of 33.4% was the last sample to allow suitable measurements. While already showing a significant increase in thickness (161 nm) compared to the other twelve samples, it presented a surface of sufficient quality to still permit optical measurements. The measurements from this sample are in agreement with the overall trends for increasing β-phase content of the study presented below; red-shift of the emission and absorption peak, lower Huang Rhys parameter, high PLQE (0.71), increase in radiative decay rate, slight increase in non-radiative decay rate (in line with the trend for the other samples of the series).

4.3 Experimental Details

In this section, the experimental details of the methods used to investigate the PFO β-phase series are outlined. The techinques are described in more details in Chapter 3.

4.3.1 Absorption

Absorption spectra were recorded[2] with a dual-beam Shimadzu UV-2600 spectrophotometer equipped with a diffuse reflectivity (integrating sphere) attachment, allowing the absorption spectra to be corrected for reflection and scattering losses. Transmittance T, specular reflectance sR and diffuse reflectance dR were recorded

[2]Absorption spectra were recorded by Florian Le Roux.

over a wavelength range of 300 to 500 nm in steps of 1 nm. The absorptance A is obtained from the data as:

$$A = 1 - (T + sR + dR) = 1 - T - R_{tot}. \tag{4.1}$$

4.3.2 PL

Time-integrated PL spectra were measured on the system described in Section 3.1. The samples were kept under vacuum and were excited at a wavelength of 380 nm with a power of 4 µW, an excitation spot area of roughly 0.1 mm^2 and an integration time of 3 s was used. The spectra are corrected for the instrumental response of the system.

4.3.3 PLQE

PLQE was measured[3] using a Jobin Yvon Horiba Fluoromax 4 spectrofluorometer equipped with a diffusely reflecting integrating sphere (Quanta-phi). The excitation wavelength was set to 390 nm. The experimental and calculation methods used here were identical to the ones presented in Ref. [135].

4.3.4 TCSPC

The PL lifetimes and decay rates were determined by TCPSC using the set-up described in Section 3.3. The samples were excited at a wavelength of 405 nm (glassy sample) or 432 nm (samples containing some β-phase, further discussion below) at a power of 200 µW and an excitation spot area of roughly 0.1 mm^2. The excitation decay was observed at 425 nm (for the excitation at 405 nm only), 438 nm, 450 nm and 464 nm. The samples were kept under vacuum during the experiment.

[3] PLQE was determined by Florian Le Roux.

4.4 Results

In this section, absorption, steady-state PL, PLQE and decay rates from the PFO series are presented and carefully analysed. The analysis methods of the data are outlined and in some cases and a short discussion on the chosen experimental settings or the data evaluation is added to provide necessary context for the interpretation of the data in Section 4.5.

4.4.1 Absorption

The resulting absorbtance spectra of the PFO films with varying β-phase are shown in Fig. 4.2. The absorptance spectra of PFO are considered to be a linear superposition of contributions from glassy phase and β-phase chain segments in the films. The disordered glassy-phase chain segments contribute a broad absorption peak centered at around 380 nm, whereas the contribution of the on a molecular level more geometrically confined β-phase chain segments is manifested as a much narrower 0-0 peak around 430 nm followed by a vibronic progression [137]. At low β-phase content, the peak develops as a shoulder on the red edge of the total absorption and becomes more distinct with increasing β-phase content in the film.

4.4.1.1 β-Phase Fraction and Absorptance Spectra

The absorption data were used to determine the percentage of chain segments in β-phase conformation, $\beta_{fraction}$. A brief derivation of the corresponding expression is given in the following, which is based on Refs. [33, 135, 150]. $\beta_{fraction}$ is defined as

$$\beta_{fraction} = \frac{c_\beta}{c_\beta + c_g}, \tag{4.2}$$

where c_β and c_g are the concentrations of the β-phase and glassy-phase chain segments in the film, respectively. Concentration c and absorption are linked through the Beer-Lambert law for absorption, which is expressed in terms of the molar extinction coefficient $\epsilon(\lambda)$ and the sample thickness t as:

$$I(\lambda) = I_0(\lambda)\ 10^{-\epsilon(\lambda)\ c\ t}, \tag{4.3}$$

where $I_0(\lambda)$ and $I(\lambda)$ denote the intensities entering and leaving the film in the absorption experiment. The molar extinction coefficient $\epsilon(\lambda)$ is related to the (napierian) absorption coefficient $\alpha(\lambda)$:

$$\epsilon(\lambda) \;=\; \frac{\log_{10}(e)}{c}\;\alpha(\lambda), \tag{4.4}$$

which is obtained from the experimental data at each recorded wavelength λ as:

$$\alpha \;=\; -\frac{1}{t}\;\ln(\frac{T}{1-R_{tot}}). \tag{4.5}$$

A spectral integration of the molar extinction coefficient over wavenumbers ν provides the oscillator strength f:

$$f \;=\; const \times \int \epsilon(\nu)\,d\nu \;= \frac{const'}{c} \times \int \alpha(\nu)\,d\nu \;=\; \frac{const'}{c} \times SA, \tag{4.6}$$

which is a measure of the strength of the electronic transition underlying the absorption process. SA denotes the spectral area and is by the above equation defined as $SA \;=\; \int \alpha(\nu)\,d\nu$. Using the oscillator strength, the concentrations in Eq. 4.2 can be rewritten in terms of the spectrally integrated areas and the oscillator strength of the glassy phase and the β-phase chain segments, $SA_{g,\beta}$ and $f_{g,\beta}$. The constant term from Eq 4.6 cancels out and by expanding the equation with f_β we arrive at the following expression for the β-phase fraction:

$$\beta_{fraction} \;=\; \frac{SA_\beta}{\frac{f_\beta}{f_g} \times SA_g + SA_\beta}. \tag{4.7}$$

The oscillator strengths of the glassy phase and β-phase chain segments differ in value. Their ratio has been derived by Huang et al. [150] using time-dependent density functional theory to be $\frac{f_\beta}{f_g} = 1.08$, which is used here.

Therefore, to obtain the fraction of β-phase chain segments for each film, the contributions of the glassy phase and of the β-phase chain segments to the total absorption of the film need to be separated. This is achieved by scaling the absorption spectrum of a glassy film with comparable thickness (termed “glassy equivalent”,

abbreviated "ge") to the total absorption spectrum of the investigated film at wavelengths below 350 nm. In the wavelength range of 300 to 350 nm, the contribution of β-phase chain segments to the total absorption has been found to be negligible [137, 144]. It is therefore assumed that the total absorption in this wavelength range stems from glassy-phase chain segments only and that each glassy chain absorbs the same amount of energy. By introducing the scaling factor F, the following equations can be written for the absorption coefficients:

$$\alpha_{ge} = \alpha_g \times (1 - F) \tag{4.8}$$

$$\alpha_{tot}^{300-350} = \alpha_g^{300-350} \times (1 - F), \tag{4.9}$$

where α_g, α_{ge} and α_{tot} denote the glassy, glassy equivalent and total absorption coefficients and the superscript in Eq. 4.9 refers to the wavelength range in which the equation holds. Eq. 4.9 was fitted[4] to the absorption data in the wavelength range from 300 to 350 nm to obtain the scaling factor F. In a next step, the "glassy spectral area" SA_g is determined from Eq. 4.8 and the definition of SA. Additonally, the "β-phase spectral area" SA_β is determined by subtraction of SA_g from the total spectral area. Then, Eq. 4.2 is used to determine the β-phase fraction for each film. The resulting values are given in Table 4.1.

The total absorptance spectrum and the contributions from the glassy-and β-phase are shown in Fig. 4.4 for each β-phase containing sample individually. The β-phase absorptance as a function of β-phase percentage in the film is depicted in Fig. 4.3. The β-phase main-peak dispersal ranges from 425 to 433 nm, showing a red-shift (towards higher wavelengths) with increasing β-phase content.

[4]The β-phase fractions as used here (in accordance with Ref. [114]) were fitted by Florian Le Roux, who also initiated the use of Eqs. 4.8 and 4.9. The numbers were validated using the orignial absorption data by the author of this thesis.

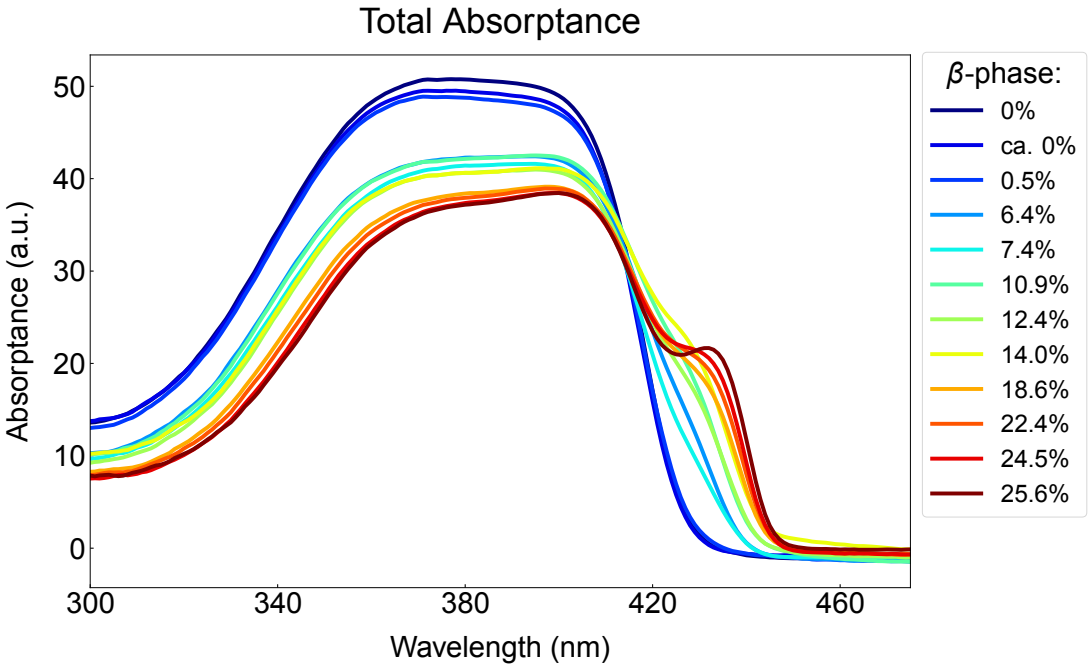


Figure 4.2: Absorptance spectra for all films. The spectra are a superposition of contributions from the glassy-and β-phase chain segments. The spectra are corrected for spectral and diffuse reflectance.

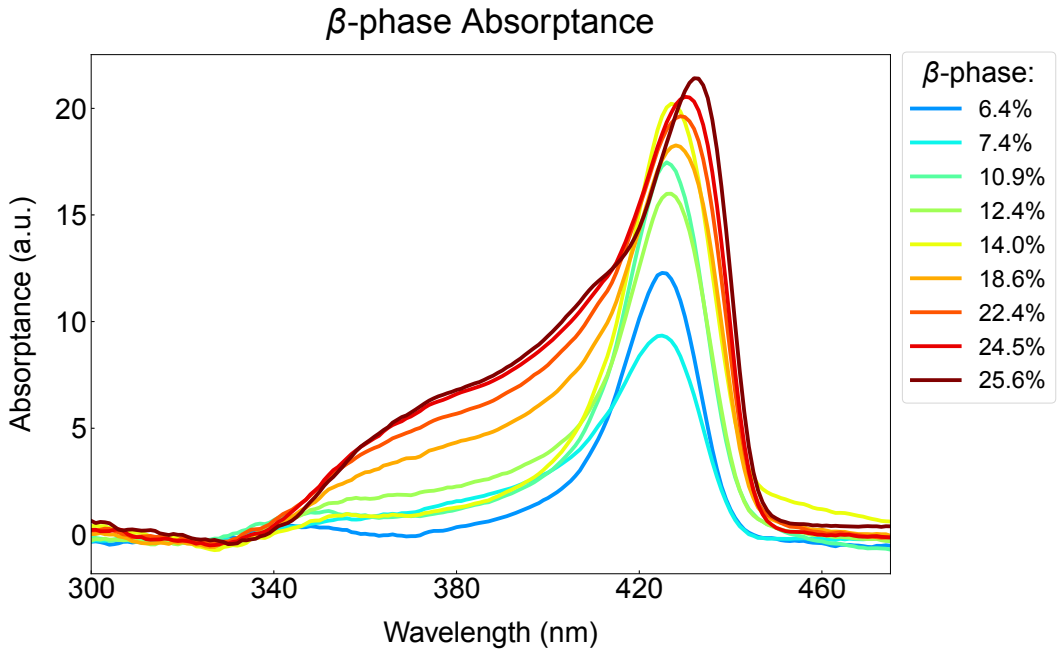


Figure 4.3: β-phase absorptance spectra of the films containing some ($\geq$ 6.4%) β-phase chain segments. The spectra were obtained by subtraction of the contribution of the glassy chain segments from the total absorptance, using the fitting method described in the text.

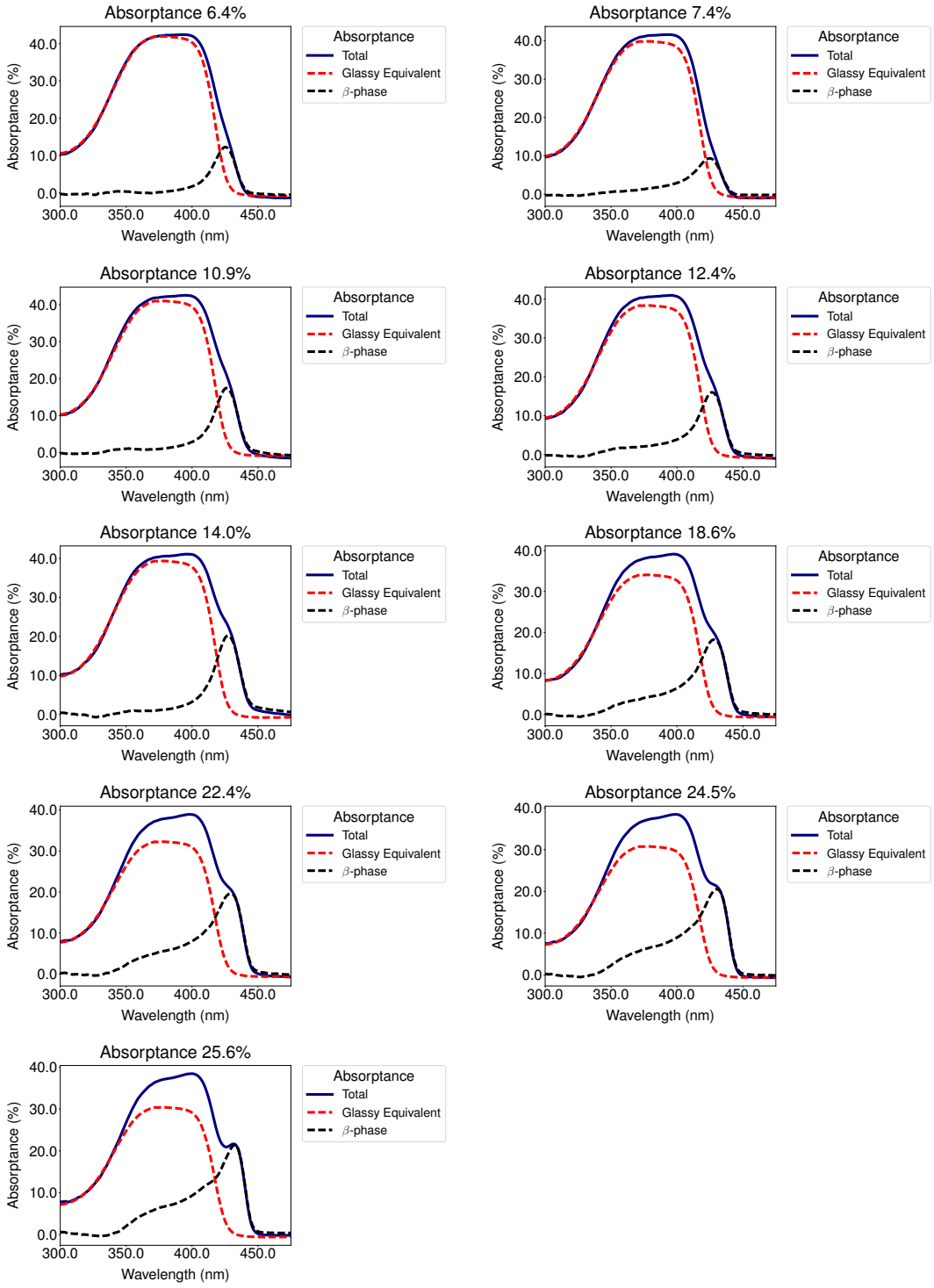


Figure 4.4: Total absorptance spectra (blue) and contributions of the glassyphase (red) and of the β-phase (black). The decomposition procedure is described in the main text of the SI. The spectra are presented for each sample containing some ($\geq 6.4\%$) β-phase. The β-phase content of the sample is indicated in the respective heading.

4.4.2 Time-Integrated PL

The normalised PL spectra are shown in Fig. 4.5. The PL spectra of the glassy ($\leq 0.5\%$ β-phase content) films feature vibronic peaks located at 426 nm, 451 nm and 480 nm. The films containing some ($\geq 6.4\%$ β-phase content) β-phase chain segments show emission peaks around wavelengths of 437 nm, 465 nm and 496 nm.

4.4.2.1 PL Peak Position

The peaks red-shift with increasing β-phase content. This shift is quantified in Fig. 4.6. The peak position of the 0-0 peak shifts by 5 nm from 435 nm to 440 nm as the β-phase fraction increases from 6.4% to 25.6%. Fig. 4.6 also shows that the shift occurs not only for the 0-0 but also for the 0-1 vibronic peak, ruling out self-absorption as the main cause of the shift as the films do not absorb at these wavelengths (cf. Fig. 4.2 for the absorption spectra).

4.4.2.2 PL Peak Narrowing

In addition to the shift in peak position, the PL peaks become spectrally narrower with increasing β-phase content. Fig. 4.7 shows the averaged FWHM of the 0-0 peak and the 0-1 peak as a function of β-phase variation. These data were acquired by fitting a sum of Gaussian peak profiles to each of the peaks. As the inset of Fig. 4.7 shows, the 0-0 peak of the glassy films is much broader than the 0-0 peak of the β-phase films. The 0-0 peak of the glassy samples stems from emission from disordered chain segments and is therefore expected to be broader than the 0-0 peak of the β-phase films, which stems from emission from the geometrically more rigid β-phase chain segments. Again, observing the narrowing not only for the 0-0 but also the 0-1 peak indicates that the peak narrowing with increasing β-phase content is not mainly caused by self-absorption.

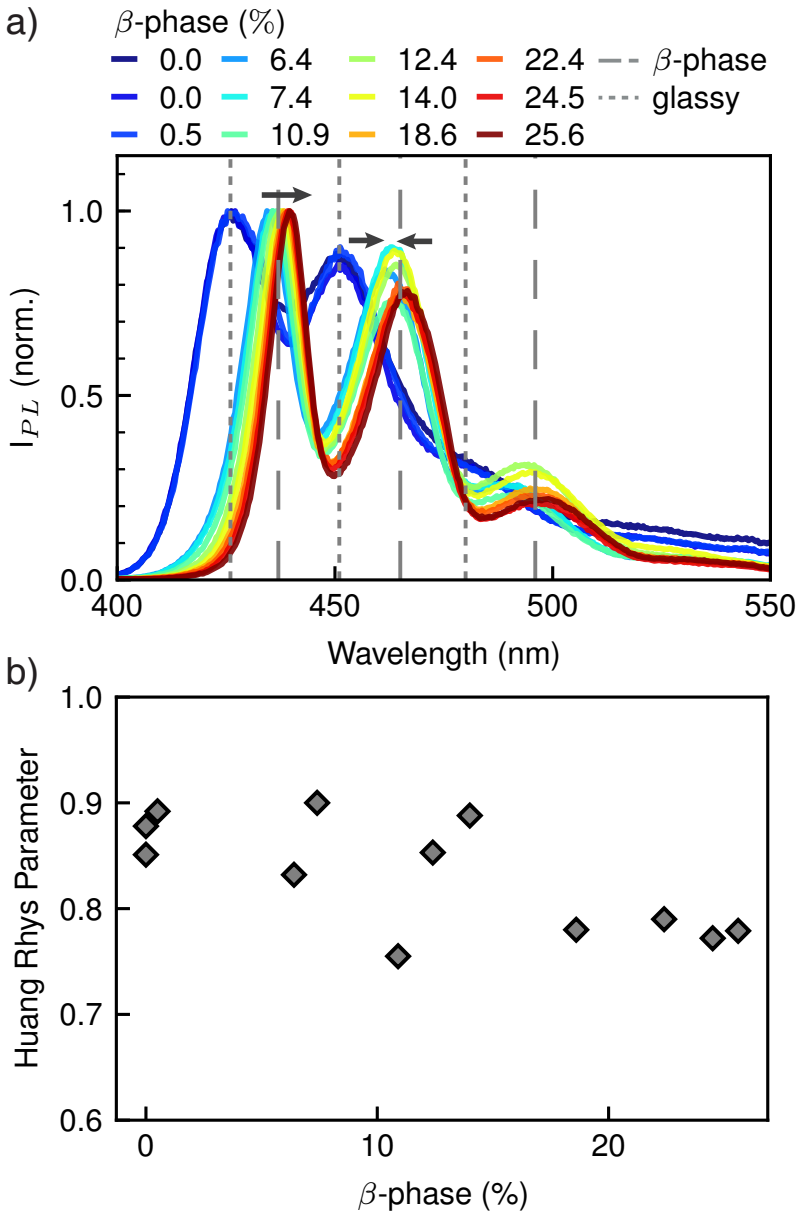


Figure 4.5: a) Normalised time-integrated PL spectra for PFO films containing different fractions of β-phase chains ranging between 0% and 25.6%. The approximate positions of the vibronic emission peaks of the glassy and the β-phase are indicated by the dotted and dashed lines, respectively. All films were excited with light of wavelength 380 nm and intensity 200 µW. The arrows indicate the observed red-shift and the peak narrowing as the β-phase fraction increases. b) Huang Rhys parameter, obtained from the ratio of the 0-0 and 0-1 PL peak heights.

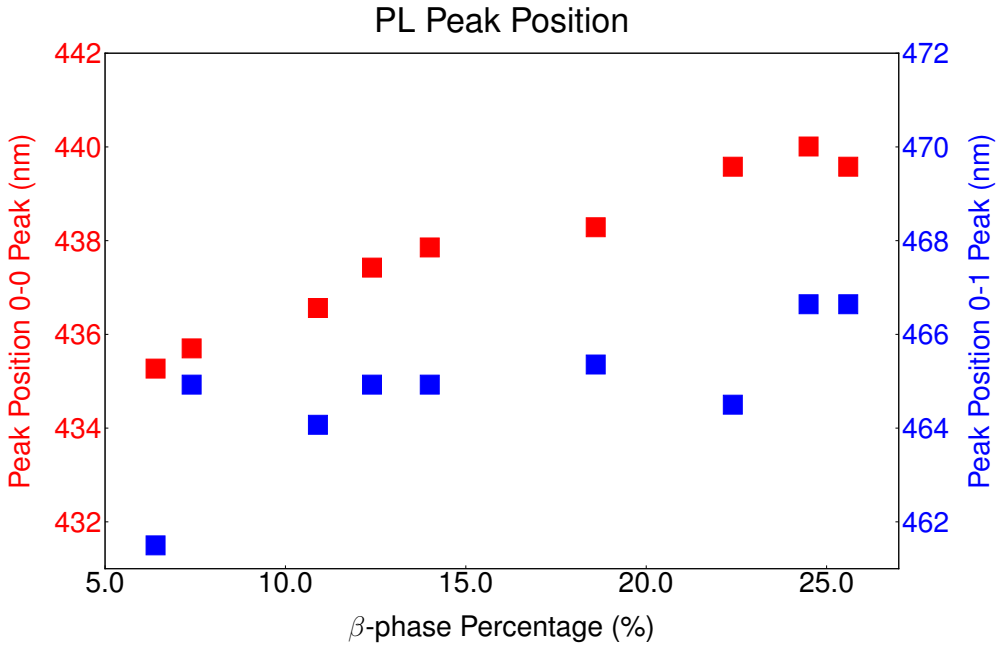


Figure 4.6: Position of the β-phase PL peaks (0-0 peak in red, 0-1 peak in blue) as a function of β-phase percentage. Both peaks show a red-shift with increasing β-phase percentage.

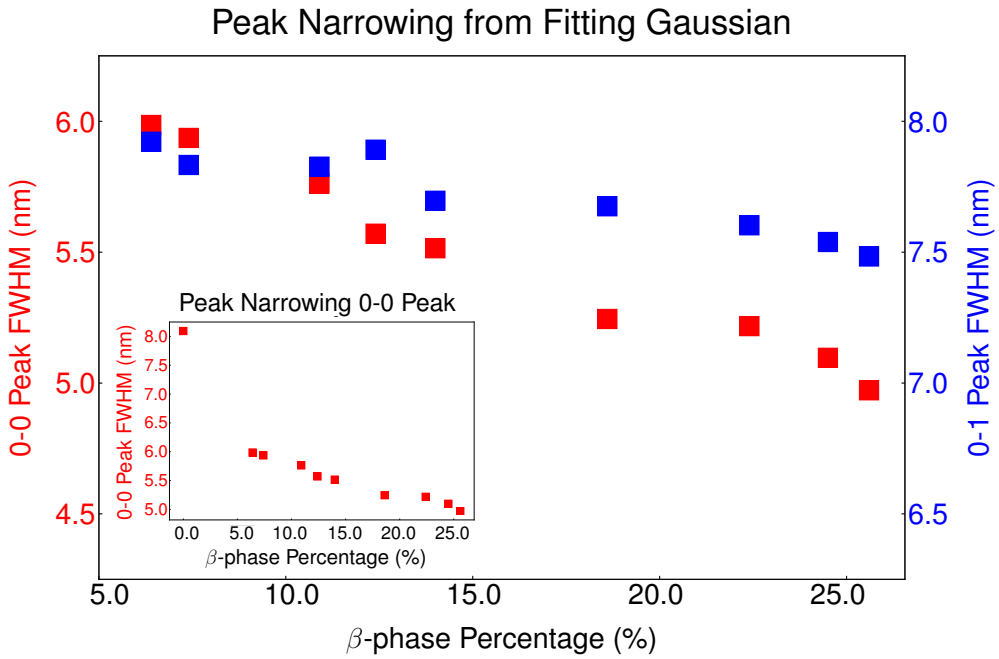


Figure 4.7: FWHM of the β-phase 0-0 (red) and 0-1 (blue) PL peaks as a function of β-phase percentage, obtained by fitting of a sum of Gaussian peak profiles to each peak. Both peaks narrow with increasing β-phase percentage. The inset shows the peak width of the 0-0 peak including the glassy film.

4.4.2.3 Huang-Rhys Parameter

Fig. 4.5b depicts the Huang Rhys Parameter S for the films with varying β-phase. The Huang-Phys Paramenter is related to the conformational relaxation energy in the excited state. It can be seen as a measure of geometric reorganisation energy upon an electronic transition ($S \propto \Delta Q^2$, the square of the displacement in conjugation coordinate). The parameter can be assessed as $S = \frac{I_{0-1}}{I_{0-0}}$ from the ratio of the peak intensities I_{0-1} and I_{0-1} of the 0-0 and 0-1 transitions, which are associated with the C-C stretch vibration replica.

For each sample, the Huang-Rhys parameter was deduced from the intensity ratio of the 0-0 and 0-1 PL peaks. The peak heights were graphically extracted from Fig. 4.5a. It is worth to note here, that at low temperatures the 0-1 peak of the PFO PL is known to consist of two spectrally overlapping peaks [151]. However, at higher temperatures, only one peak can be observed and as they are no longer distinguishable. However, this does not change the here discussed trend. The Huang-Rhys Parameter decreases with increasing β-phase content of the films.

4.4.3 PLQE and Decay Rates

PLQE and decay rates are depicted in Fig 4.8. To extract the natural lifetimes τ, a single exponential time decay $e^{-(t-t_0)/\tau}$ was fitted to the measurement data from 0.5 ns to 2 ns, where t_0 is chosen for each sample to be at 50% signal strength in the rise of signal upon excitation. Exemplary fits are shown for all samples in Fig. 4.10 for a detection wavelength of 450 nm. From the lifetimes τ and PLQE, the total, radiative and non-radiative decay rates k_{tot}, k_{rad} and k_{nonrad} are calculated for each sample using the following set of relations:

$$\begin{aligned} k_{tot} &= 1/\tau \\ k_{tot} &= k_{rad} + k_{nonrad} \\ k_{rad} &= PLQE \times k_{tot}. \end{aligned} \tag{4.10}$$

Emission from samples containing β-phase (even a small amount) stems overwhelmingly from β-phase chain segments, regardless of the excitation wavelength, because the transfer of excitation energy from glassy phase to β-phase chain segments is ultrafast and complete. This conclusion is experimentally supported by the observed dominance of β-phase spectral features in the time-integrated PL compared to the absorptance (cf. Figs. 4.2 and 4.3) and by the ultra-fast (picoseconds time scale) energy transfer, which is completed before significant photon emission has occurred (cf. Chapter 5). Therefore, the β-phase can be excited in two ways: i) direct excitation (at 432 nm) and ii) excitation through energy transfer from the glassy-phase chain segments (at 405 nm). Both excitation wavelengths should yield the same PL-lifetimes. Analyzing the data, a slight disagreement in lifetimes for the two excitation wavelengths (405 nm and 432 nm) was initially noted. However, this discrepancy was resolved upon illuminating some of the samples alternatively from the back through the quartz substrate. On these samples 4 measurements were performed for each detection wavelength: exciting at 405 nm and 432 nm from the front as well as through the back. In doing so, it was found that the PL lifetimes for i) 432 nm front illumination, ii) 405 nm back illumination and iii) 432 nm back illumination yield the same results for PL lifetimes and only the 405 nm front illumination results in slightly different PL lifetimes. On the basis of this result, the observed differences in PL lifetimes from front and back illumination at 405 nm can be attributed to the presence of impurities/traps at the surface of the PFO films. At the wavelength of 405 nm the penetration depth is shorter than at 432 nm, making the 405 nm excitation more prone to surface impurities. No difference in PL lifetimes was observed when illuminating the samples at 432 nm from front and back. Accordingly, the excitation wavelength was chosen to be 432 nm (direct excitation of β-phase) and the samples were excited from the front. For all measurements, the detection wavelength does not alter the resulting PL lifetime. (c.f. Fig. 4.9), therefore, an average over all detection wavelengths was taken for Fig. 4.8.

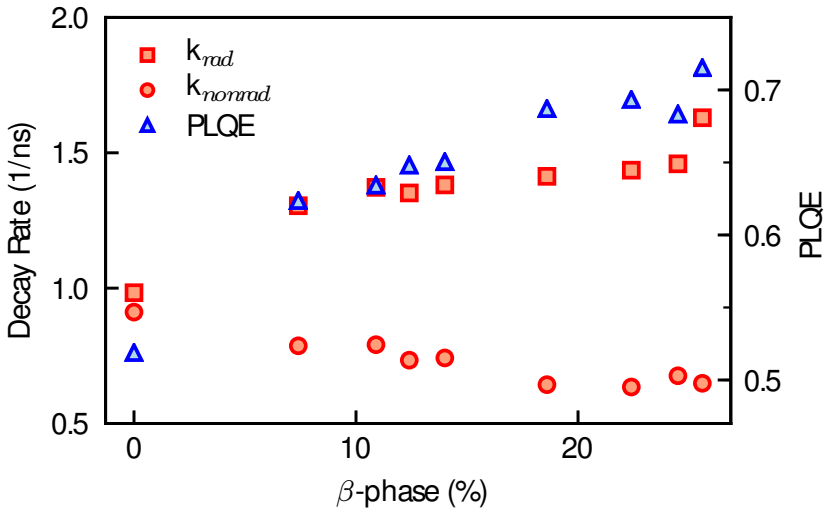


Figure 4.8: PLQE (blue triangles, right axis), radiative (red squares, left axis) and non-radiative (red circles, left axis) PL decay rates. The rates were deduced from the PL lifetimes measured by TCPSPC and the PLQE values.

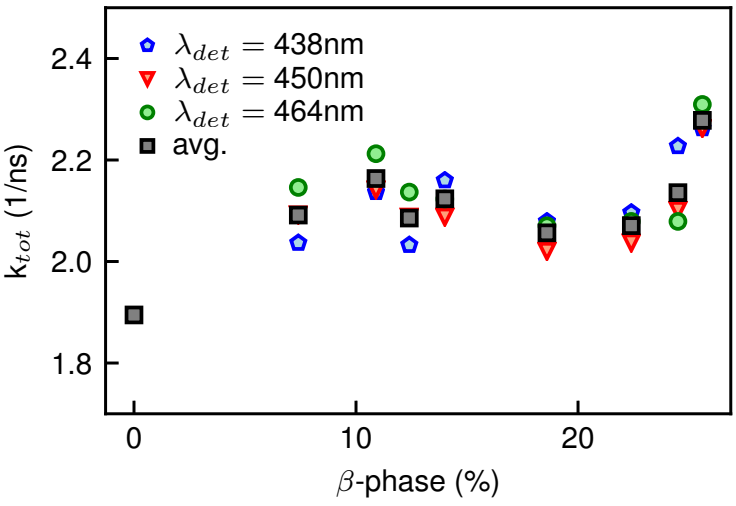


Figure 4.9: Total decay rate for each sample obtained by a mono-exponential fit to TCSPC data. The rates calculated for the different detection wavelengths (blue pentagons: 438 nm, red triangles: 450 nm, green circles: 464 nm) and an average over these wavelengths (black squares) are shown.

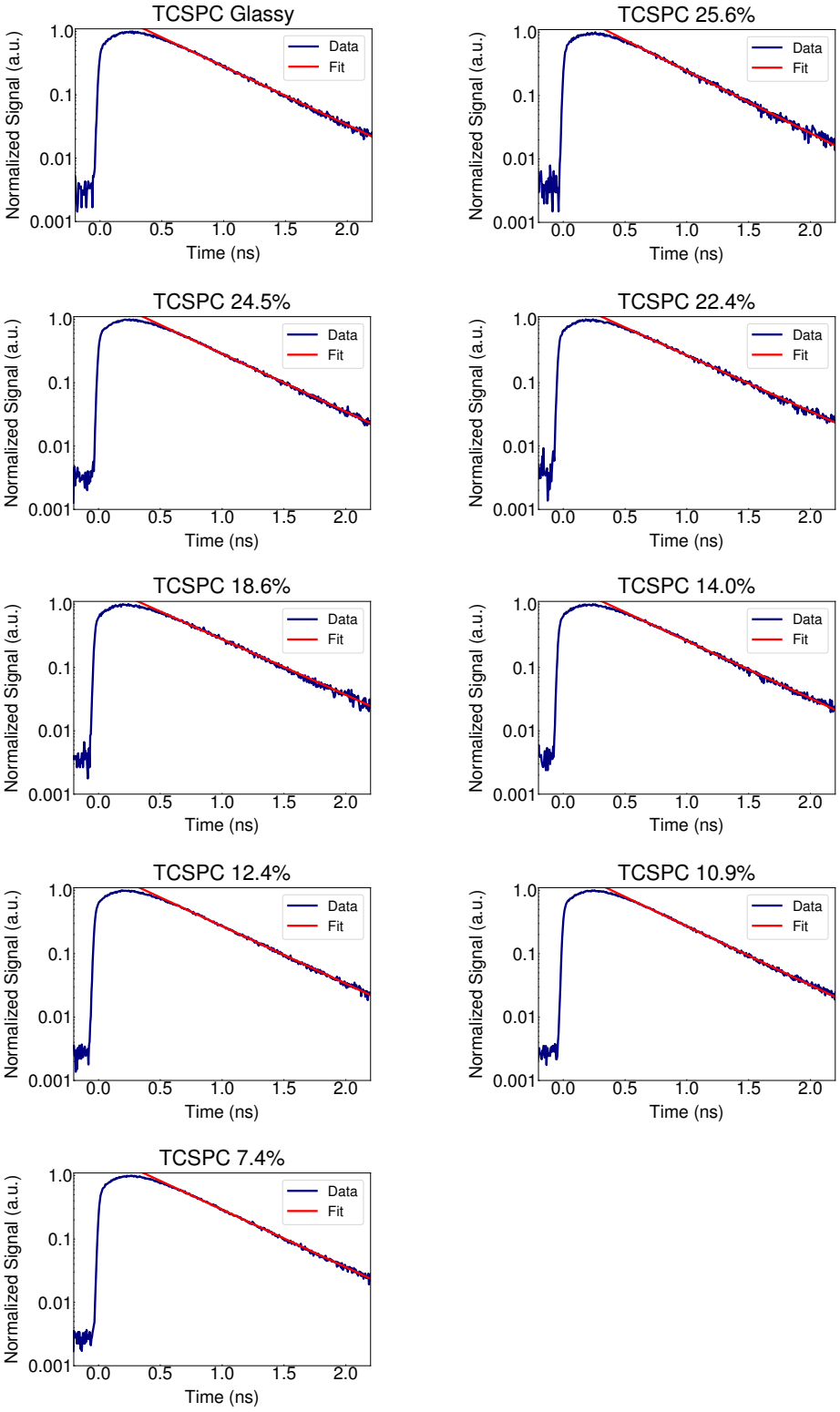


Figure 4.10: Experimentally determined PL lifetime decay (blue) and mono-exponential fits (red, fitted to 0.5 to 2 ns). The β-phase content of each sample is indicated in the respective heading. The lifetime decay was measured at 450 nm.

4.5 Discussion

This chapter addresses the question: "How does the β-phase content influence chain conformation of PFO thin films?", to which careful examination of the emission and absorption spectra can provide answers. Absorption and emission reflect the electronic states of a polymer, which in turn are affected by conformational changes. Additionally, due to the importance of achieving high PLQE in possible PFO-based devices, the effect on PLQE is of great interest. The structure of this discussion section is therefore as follows: In a first section, the steady-state PL spectra are examined, in a second section an interpretation of the absorptance spectra is given and in a third section, decay rates and PLQE are discussed.

The normalised steady-state PL spectra for the PFO film series are shown in Fig. 4.5a. PL was collected following illumination with 380 nm-wavelength light, which predominantly excites the glassy phase. It is evident, however, that the emission only resembles the spectrum expected for the glassy phase of PFO if no substantial ($\leq 0.5\%$) β-phase is detectable in the corresponding absorptance spectra. For all films containing $> 0.5\%$ β-phase, the PL spectra are dominated by the red-shifted emission from the β-phase. This observation is in accordance with previous findings [135, 151] and suggests almost complete channeling of excitations from the glassy to the β-phase after photoexcitation.

The observed peak positions are consistent with previous reports [130, 135, 151], with the β-phase emission peak around 437 nm assigned to the $S_1 \rightarrow S_0$ 0-0 vibronic transition [135, 137, 151].

Interestingly, closer examination of the PL spectra dominated by β-phase emission reveals that all vibronic peaks shift to the red with increasing fraction of β-phase chain segments in the film. The peak position of the 0-0 peak shifts by 5 nm from 435 nm to 440 nm as the β-phase fraction increases from 6.4% to 25.6% (cf. Fig. 4.6). Even though shifts in PL peak position with β-phase content have been observed

previously [130, 135, 145], they have not yet been considered in detail [130, 145] and were considered to be an artefact caused by self-absorption and/or changes in microstructural heterogeneity [135]. As mentioned in the result section, self-absorption as the main cause of the red-shift may be ruled out, as these shifts are also present for the 0-1 vibronic peaks, which are located at wavelengths at which the films do not absorb and shifts are also observed in the corresponding absorptance spectra (cf. Fig. 4.3). Instead, the peak shift can be attributed to a change in the electronic states with increasing β-phase content. In addition to the peak shift, the vibronic emission peaks are found to become spectrally narrower with increasing β-phase content in the film (cf. Fig. 4.7). Both the shift of the emission peaks to lower energies and the decrease in spectral broadening are suggested to arise from an increase in conjugation length and a more delocalised excited state [13, 152]. Planarisation [153] and an increase in oligomer length [154] in π-conjugated poly- and oligomers have been shown to result in red-shifted emission, which is a consequence of a highly delocalised excited state that is also less susceptible to energetic disorder arising from variations in conjugation length. Hence, the observations from the PL spectra suggest that the β-phase chain segments become more planar and/or include more repeat units with increasing β-phase fraction in the film.

Further support for this conclusion comes from the associated trend in the Huang-Rhys parameter (S) as a function of β-phase fraction shown in Fig. 4.5b. A decrease in S with increasing β-phase content is found, which signifies a decrease in displacement from the ground-state equilibrium to the lowest excited-state geometry, with respect to the configuration coordinate associated with the C-C bond separation. Upon photoexcitation, the C-C bond alternation changes along the polymer backbone as π-electrons are re-distributed in a way that planarises the backbone in the excited state. As a result, more planar geometries may yield smaller changes in conjugation coordinate upon excitation (decreased S). Studies of phenylenevinylene oligomers [155] and fluorene oligomers [156], have indeed shown that chain planarisation leads to

enhanced electronic delocalisation and a concomitant reduction in configurational coordinate change per oscillator strength, resulting in a decrease in S with increasing oligomer length. It can therefore be concluded that as the β-phase content in PFO films is increased, β-phase chain segments exhibit a more planar geometry and comprise a higher number of fluorene units associated with increased effective π-conjugation.

Absorptance spectra are shown in Figs. 4.2 and 4.3. Some of the trends observed in the absorptance spectra are similar to those in emission, with the 0-0 absorption peak of the β-phase fraction clearly red-shifting with increasing β-phase fraction (Fig. 4.2). However, whereas all β-phase emission spectra show a well-defined vibronic progression, the absorptance spectra seem to have broader emission beyond the 0-0 peak, and for the lower β-phase fractions only the 0-0 peak is well-resolved (Fig. 4.3). Compared to other studies [130, 135], the main peak of the β-phase absorptance is slightly blue-shifted and the resolution of the vibronic progression and the appearance of the β-phase peak in the total absorption are seen at higher β-phase contents only. The latter could be caused by the blue-shift of the peak, as there is more overlap with the broad glassy absorption peak at lower wavelengths.

A possible reason for the apparent broadening of the β-phase absorption spectra lies in the method by which these were determined, which is commonly used across the field. The method relies on the subtraction of the "glassy equivalent" absorptance spectrum from the total absorptance of a film containing some β-phase (outlined in more detail in Section 4.4.1). A slight distortion in the obtained absorptance spectrum of a mixed film might arise if the reference spectrum, the "glassy equivalent" absorptance spectrum, does not fully accurately represent the actual glassy phase absorption of the mixed film, which contains some β-phase. The subtraction of this reference spectrum may lead to slight distortions in the resulting β-phase spectrum. There are two possible reasons for this to be the case. First, polymer chains in a particular conformation or local environment may be more likely to convert to

β-phase, which means that the sub-set of unconverted glassy-phase chains left differs from the ensemble found in an all glassy film. Second, the presence of β-phase in the film might introduce strain on the glassy phase, slightly shifting its energetic landscape. Given the dependence of β-phase presence on strain and local order, both of these scenarios are plausible. Such differences would be most prominent at the onset of the glassy phase absorption, where changes in energetic disorder will lead to a sharpening or broadening of the onset.

Additionally the spectral deconvolution method might introduce a small inaccuracy on the β-phase percentage. However, the trend of increasing β-phase percentage is very clear and small deviations will not change any of the discussions and conclusions presented in this and the following chapter.

As an alternative, these effects may results from small random fluctuations in the torsion angle between fluorene units within the β-phase, which have been shown to result in broadening in the absorption spectrum [157, 158]. Both explanations highlight a strong dependence of the optical properties on film microstructure and therefore also emphasise the possibility that these properties may depend significantly on the preparation methods used [159].

The possibility to enhance the PLQE of PFO thin films by tuning the β-phase fraction [135] provides a motive to further study the variation in PLQE for a set of samples with systematically varying fraction, as prepared here. PLQE and decay rates are plotted in Fig. 4.8. The radiative decay rate increases as a function of increasing β-phase while the non-radiative rate decreases. The PLQE shows an increasing trend with increasing β-phase content in the film, with the PLQE value of 0.72 deduced here for the 25.6% β-phase sample being the highest PLQE value reported for a PFO film at the date of the publication of this study [114].

A change in PLQE with varying β-phase fraction has been observed previously [130, 135, 144], with some authors [130, 135] finding an increase with increasing β-phase

content, followed by a decrease in PLQE at a β-phase content in excess of $\sim 10\%$, while others [144] reported no initial increase but still a decrease at higher β-phase fractions. While the reasons for such trends in PLQE as a function of β-phase content in PFO films were not fully explained in these studies, it has been assumed that both the β-phase fraction itself and the degree of dispersal of the β-phase chain segments within the glassy phase may play an important role [135]. Thus film microstructure, which may also depend on the film preparation method, will influence the photophysical properties of PFO films. A range of PLQE values were obtained by different authors [130, 135, 144] using different batches of polymer handled in different ways to prepare films and using different measurements. This suggests that it is not only the β-phase percentage in the film that determines photophysical properties but that indeed the dispersion and arrangement of the β-phase chain segments may influence the observed trends with β-phase fraction.

In contrast to the above mentioned PLQE studies, the here presented study employs a single method for the preparation of a series of PFO films with varying β-phase content. The changes observed can therefore be assumed to be closer to the intrinsic conformational changes for varying β-phase content resulting from this method. In particular, the increase in radiative and decrease in non-radiative decay rate may be closely linked to the planarisation and enhancement in conjugation length which is observed with increasing fraction of β-phase. With increasing conjugation length of the β-phase segments an enhancement of oscillator strength is expected while planarisation of the backbone may lead to a reduced intersystem crossing rate, possibly caused by the resulting decoupling of p- and 2s-orbitals, as reported for other π-conjugated molecules. [160]. Therefore, the enhancement of the PLQE with increasing β-phase content may be directly linked with the accompanying conformational changes of the β-phase segments.

4.6 Summary and Conclusion

In this chapter, the influence of the fraction of β-phase chains present in PFO thin films on the nature of the electronic states and the chain conformation of the polymers was investigated. Importantly, consistency amongst PFO films was ensured by employing the same fabrication technique to obtain a wide range of β-phase fractions within the films. This enabled the realisation of an analysis of different photophysical properties on a series of comparable films with considerably varying β-phase content for the first time. Such comparability is of great importance to gain more fundamental insights into the photophysical properties of PFO thin films as these properties are highly sensitive to film microstructure and therefore to film preparation.

Reaching high PLQE is decisive for using PFO in device applications. All PFO films fabricated for this study exhibited high (> 0.6 for the films containing β-phase) PLQE, peaking at a value of 0.72 at 25.6% β-phase content.

With increasing β-phase content, the emission peaks of the β-phase were observed to red-shift and to narrow while the associated Huang-Rhys factor decreases. These findings suggest that the conformation of β-phase segments changes with increasing fraction, adopting a more planar structure and/or including a larger number of repeat units, likely enhancing the value of the PLQE. The insights obtained from this systematic study deepen the understanding of the fundamental photophysical properties of PFO films, which is essential for the further development of light-emitting materials and applications.

5

Energy Transfer in PFO Films with Varying β-phase Content

Contents

5.1 Background and Motivation 70
5.2 Experimental Details 71
5.3 Results and Analysis 72
5.3.1 Calculating Förster Radius from PL Dynamics 72
5.3.2 Calculating Förster Radius from Donor Emission and Acceptor Absorption Spectra 82
5.4 Discussion 88
5.5 Summary and Conclusion 93

Reproduced in part from work published by Eggimann et al. in Ref. [114].

5.1 Background and Motivation

The two phases of the blue-emitting conjugated polymer PFO, namely the disordered "glassy" phase and the more crystalline β-phase, differ on a microscopic level by their chain conformation [137–141]. These are distinct phases which interact with each other through energy transfer (ET) [151, 161]. While the absorption spectrum of PFO films typically reflects the sum over the distinct spectral contributions from glassy- and β-phase conformations present, the emission spectrum is consistently dominated by contributions from the β-phase, even for relatively minor inclusions (cf. Figs. 4.2 and 4.5a). This observation led Ariu *et al.* [140, 151] to the conclusion that, following excitation, energy is transferred efficiently from glassy-phase chain segments to β-phase chain segments. Such ET was indeed found to occur on a sub-picosecond time scale for a PFO film with roughly 25% β-phase content by Khan et al. [161] who used ultrafast PL spectroscopy to resolve the ET process. ET in PFO has since been a subject of further study for example focusing on the role of exciton diffusion [147, 162], on phase intermixing within the films [147] as well as on theoretical modelling to affirm the applicability of Förster resonant ET (FRET) [148]. The work presented in this chapter contributes to this field with a conclusive investigation of the dependence of such ET on β-phase content for a set of films with a reliably and widely tuned range of β-phase fractions.

To unravel how β-phase content and associated conformational changes (discussed in Chapter 4) impact the ET from glassy phase to β-phase chain segments, the dynamics of such transfers was directly observed and is presented and analysed in terms of Förster theory and compared to results from steady-state measurements. The central question addressed in this chapter is: ***How does a change in β-phase content affect FRET in PFO thin films?***

5.2 Experimental Details

This section contains a brief overview of the measurements performed to investigate ET in PFO films. The preparation of the PFO thin film samples with varying β-phase (purely glassy and 7.6% to 25.6% β-phase) is illustrated in Section 4.2 of the previous chapter. The measurements performed for the discussion in this chapter were steady-state PL and absorption measurements (outlined in Section 4.4.1 and Section 4.4.2) and PL-upconversion spectroscopy of which the experimental details are given in the following.

PL-upconversion spectroscopy enables ultrafast measurement of PL with a femto-seconds range time-resolution, allowing experimental investigation of fast ET dynamics [161, 163, 164]. The technique is described in more details in Section 3.2. All samples were excited with frequency-doubled laser light at 405 nm with an excitation pulse generated by a mode-locked Ti:Sapphire laser at a repetition rate of 80 MHz, having a pulse duration of 80 fs and an excitation spot area of roughly 0.1 mm^2. The gate beam for PL-upconversion was at the initial wavelength of 810 nm. The signal was detected at the upconverted wavelength of 276 nm, which corresponds to the signal stemming from sample PL at 419 nm. For PFO PL at 419 nm, the main contribution is expected to be from the PL decay of the glassy phase [161]. The samples were kept under vacuum to avoid photo-oxidation. For each sample, four decay traces were consecutively recorded, with the time delay swept forwards for the first and third measurement and backwards for the second and forth measurement to monitor and ensure sample stability during experimentation. The presented decay traces correspond to the average of the four scans.

5.3 Results and Analysis

In this section, the analysis of ET in PFO thin films in terms of Förster theory is outlined and the results from the corresponding measurements are presented. FRET is based on dipole-dipole interactions between an energy donor (here, glassy-phase chain segments) and an energy acceptor (here, β-phase chain segments). The formalism is used to express the rate of ET in terms of the Förster radius R_0, which is defined as the distance between donor and acceptor at which excitation ET from the donor to the acceptor is as likely to happen as any other de-excitation of the donor. [59, 71]. The Förster radius can be obtained through a range of measurements and considerations [64]. Here, the Förster radius is determined from i) time-resolved PL decay (Section 5.3.1) and ii) the spectral overlap between donor emission and acceptor absorption (Section 5.3.2).

5.3.1 Calculating Förster Radius from PL Dynamics

As the first step, time-resolved PL measurements were used to determine R_0 from the PL decay originating predominantly from the glassy phase. The derivation of the expression for R_0 is outlined and its parameters are discussed in Section 5.3.1.1. The results from the measurement of the PL transients are presented in Section 5.3.1.2.

5.3.1.1 Theoretical Background and Derivation of the Expression for the Förster Radius

Time-resolved PL data can be used to obtain the Förster Radius R_0. The expression for R_0 is derived by considering an ensemble of donors and acceptors, which are assumed to be evenly distributed in space. An average is taken over all possible ETs from a donor to an acceptor, assuming that the ET is governed by dipole-dipole interactions [30, 33, 59, 163, 165] (more detailed derivation below):

$$R_0 = \left(\frac{3}{2\pi^{\frac{3}{2}}} \frac{\sqrt{\tau_d}\gamma}{c_\beta} \right)^{1/3} \tag{5.1}$$

where τ_d denotes the excitation lifetime of the donor, here the glassy-phase chain segments, γ relates the Förster radius to the donor emission and is determined from the PL transients (cf. Eq. 5.19) and c_β is the density of β-phase chromophores. These parameters are examined in more detail in the following:

Excitation lifetime, τ_d: The excitation lifetime of the glassy phase chromophores was obtained from TCSPC measurements (see Section 4.4.3) by fitting a monoexponential decay curve to the data and was found to be $\tau_d = 526\,\text{ps}$. τ_d represents the total lifetime rather than the radiative lifetime only.

Analysis of the PL-upconversion transients, γ: The parameter γ captures the effective rate with which ET occurs and is obtained from analysis of the donor emission decay dynamics. Here, a brief derivation of the equations used for the analysis of the PL transients is given, which is based on Refs. [59, 163, 165–167]: If interactions between the excitations can be neglected (i.e. low-density regime), the following rate equations for the number of excited donors/acceptors $n_{d/a}$ characterise the ET dynamics:

$$\frac{dn_d}{dt} = G_d(t) - \frac{1}{\tau_d} n_d(t) - k_{da}(t) n_d(t) \tag{5.2}$$

$$\frac{dn_a}{dt} = G_a(t) + k_{da}(t) n_d(t) - \frac{1}{\tau_a} n_a(t). \tag{5.3}$$

Here, $G_d(t)$ represents the direct excitation rate of the donors and $G_a(t)$ refers to direct excitation of acceptor molecules, $\tau_{d/a}$ are the excitation lifetimes of the donor/acceptor and $k_{da}(t)$ is the ET rate. The rate equations as presented in Eqs. 5.2 and 5.3 hold for ET from a donor to an acceptor ensemble in general. The nature of the ET is determined by the transfer rate $k_{da}(t)$. For Förster-type ET, which assumes that the ET is governed by dipole-dipole interactions, and in the case of an even spatial distribution of the acceptors in 3 dimensions can be written as [163, 165]:

$$k_{da}(t) = \frac{\gamma}{\sqrt{t}}, \tag{5.4}$$

with

$$\gamma \;=\; \frac{2\pi^{\frac{3}{2}}}{3}\,\frac{c_a}{\sqrt{\tau_d}}\,R_0^3. \tag{5.5}$$

Here, c_a denotes the acceptor concentration and R_0 is the Förster radius. ET from a fixed donor to a single acceptor in close proximity will occur at a faster rate than to a single acceptor located further away, which leads to the apparent time-dependence (slowing down over time) of the acceptor ensemble-averaged $k_{da}(t)$. Using the initial conditions $G_{d/a}(t) = N_{d/a}\,\delta(0)$ (delta-like excitation at $t = 0$) and $n_{d/a}(0) = 0$ (no excited donors/acceptors at $t = 0$) the rate equations are solved by:

$$n_d \;=\; N_d\,\exp(\frac{-t}{\tau_d} - 2\gamma\sqrt{t}) \tag{5.6}$$

$$n_a \;=\; N_a'\,\{\Psi(\frac{\gamma}{\vartheta} + \vartheta\sqrt{t}) - \Psi(\frac{\gamma}{\vartheta})\}\,\exp(\frac{-t}{\tau_a}), \tag{5.7}$$

where the following notation has been introduced,

$$\vartheta \;=\; \sqrt{|\tau_d^{-1} - \tau_a^{-1}|}, \tag{5.8}$$

$$N_a' \;=\; N_a \;+\; N_d\,\sqrt{(\pi)}\,\frac{\gamma}{\vartheta}\,\exp(\frac{\gamma}{\vartheta})^2 \tag{5.9}$$

and $\Psi(x)$ denotes the error function:

$$\Psi(x) \;=\; \frac{2}{\sqrt{\pi}}\int_0^x e^{-y^2}\,dy. \tag{5.10}$$

The PL intensity data is modelled as a sum of contributions from both, glassy phase and β-phase chain segments:

$$I_{PL} \;=\; C_d\,n_d \;+\; C_a\,n_a. \tag{5.11}$$

Here, in addition to the excited donor/acceptor populations $n_{d/a}$, the excitation and detection wavelengths influence the strength of the contributions to the PL intensity from each of the two phases, accounted for by C_d and C_a. Khan et al. [161] have argued that at 419 nm the β-phase emission is negligible. However, close examination

of the PL data from the PFO thin films (cf. Fig. 4.5a) indicates a small but non-negligible contribution from the β-phase chain segments at 419 nm, which is therefore included into the analysis. As a further assumption in ET studies, direct excitation of the acceptor molecules is often neglected according to an assumption that the acceptor concentration is small or that the acceptor does not absorb at the excitation wavelength. There is however a considerable amount of acceptors (β-phase chain segments) present in the PFO films, which absorb at 405 nm (cf. Fig. 4.3) because of the vibronic progression (0-1, 0-2 peaks) above the 0-0 peak. Therefore, direct excitation of the acceptors is included in the derivation, although it is still expected to be only a small contribution.

To derive an expression for $I_{PL}(t)$, it is further useful to note that the PL lifetimes $\tau_{d,a} >> t$ over the timescales t of the ET measurements (i.e. measurements of the PL transients) as the excitation lifetimes of the donor (glassy phase) and the acceptor (β-phase) are of the order of ns, whereas the ET dynamics are investigated on a ps timescale. Mathematically, this assumption is expressed as $\tau_{d,a} \rightarrow \infty$ and Eqs. 5.2 and 5.3 rewrite as:

$$\frac{dn_d}{dt} = G_d(t) - k_{da}(t)n_d(t) \tag{5.12}$$

$$\frac{dn_a}{dt} = G_a(t) + k_{da}(t)n_d(t). \tag{5.13}$$

Adding these two equations results in

$$\frac{dn_d}{dt} + \frac{dn_a}{dt} = G_d(t) + G_a(t) \tag{5.14}$$

and for $t > 0$

$$\frac{dn_d}{dt} + \frac{dn_a}{dt} = 0, \tag{5.15}$$

which is solved by

$$n_d(t) + n_a(t) = \text{const}, \tag{5.16}$$

implying that the total number of excited donors plus excited acceptors does not change over time, which is to be expected as it has been assumed that there are no decay pathways for the excitation ($\tau_{d,a} \rightarrow \infty$) other than transferring from the donor to the acceptor. Using the initial conditions, this also implies const$= N_d + N_a$. Eqs. 5.12, 5.13, and 5.16, are thus solved by:

$$n_d = N_d \exp(-2\gamma\sqrt{t}) \tag{5.17}$$

$$n_a = N_a + N_d\,(1 - \exp(-2\gamma\sqrt{t})) \tag{5.18}$$

and the total PL intensity $I_{PL}(t)$ then takes the following form:

$$I_{PL}(t) = A \exp(-2\gamma\sqrt{t}) + B, \tag{5.19}$$

where $A = (C_d - C_a)\,N_d$ and $B = C_a\,(N_d + N_a)$. The PL intensity $I_{PL}(t)$ shows a square root dependence on time, which accounts for the shape of the PL transients and is characteristic for FRET in a spatially random three-dimensional distribution of donor and acceptor dipoles (see discussion below). Fitting Eq. 5.19 to the transients hence allows for the extraction of γ, from which R_0 may be determined through Eq. 5.1 for every PFO film containing a given β-phase fraction.

To provide further argumentation for using Förster theory and therefore the $\sqrt{t}$-term in Eq. 5.19, the transient data from which the constant offset B was subtracted are plotted in a Kohlrausch-Williams-Watts (KWW) representation in Fig. 5.1. In a KWW representation, the logarithm of the ratio of the initial PL intensity I^0_{PL} and the PL intensity as a function of time $I_{PL}(t)$ is plotted versus time on a log-log scale [168]. PL intensity, which represents the surviving exciton population at a time t and therefore the excitation decay at that instant, is assumed to follow a power law with the exponent α:

$$I_{PL}(t) = I^0_{PL}\, e^{(-t/t_0)^\alpha}. \tag{5.20}$$

The slope of a KWW plot thus represents the value for the exponent α. A slope of $\alpha = 0.5$ was fitted in Fg. 5.1 which fits the data well and supports the $\sqrt{t}$ fit and therefore the use of Förster theory for the analysis.

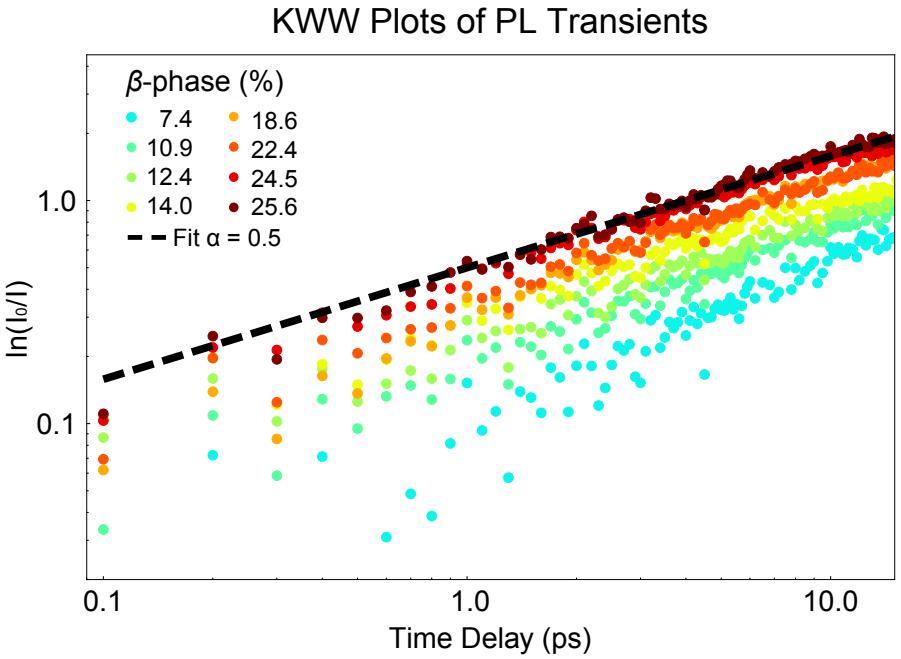


Figure 5.1: KWW plot of the PL-upconversion transient data (colored dots) with the constant offset I_β^0 subtracted. Colors indicate the β-phase percentage in the film. A line with slope $\alpha = 0.5$ is fitted to the data (dashed line).

Density of β-phase chromophores, c_β: The density of β-phase chromophores is estimated as (cf. Eq. 4.2):

$$c_\beta = \frac{\beta_{fraction}}{1-\beta_{fraction}} c_g, \tag{5.21}$$

where $\beta_{fraction}$ denotes the fraction of total chromophores in β-phase, which has been obtained from absorption data (see Section 4.4.1). c_g is the chromophore density in glassy spun-cast film, which was determined by Stevens et al. to be $2 \times 10^{19}\,\mathrm{cm}^{-3}$ [169]. Other authors [161] have at this point also introduced a factor to account for the changes in chromophore density in an all glassy film compared to a film containing some β-phase chromophores. However, this is already incorporated into the initial calculation of $\beta_{fraction}$, as a change in glassy chromophore numbers is taken into account when the fraction of β-phase chromophores is calculated (see discussion in Section 4.4.1).

5.3.1.2 Results from Time-Resolved Data

Eq. 5.19 was fitted to the transient data to obtain γ, A and B. For the sample containing 7.4% β-phase, the amplitude A was limited to obtain a sensible fit (discussion below). The fits for each sample, together with the data, are displayed in Fig. 5.2, showing that the experimental data can be well described using Eq. 5.19.

To examine the sensibility of the fits, the ratio of the fitting parameters A and B (cf. Fig. 5.3), defined through Eq. 5.19, was further investigated. A rough estimate of B/A can be done from absorption and PL spectra. The absorption spectra reflect how much of the initial excitation is absorbed by glassy phase and by β-phase chain segments (N_a and N_d) at the excitation wavelength. Fig. 4.3 shows that the higher the β-phase fraction the more is absorbed by β-phase chain segments, leading to an increase in B/A. The PL spectra shown in Fig. 4.5a contain information on C_a and C_d. Due to the red-shift in PL, C_a decreases with increasing β-phase, leading to a decrease in B/A. The effects from changes in PL and absorption spectra with varying β-phase fraction on B/A therefore compete. For the fitting process, a rough estimate of B/A from the absorption and PL spectra was performed and the estimated values

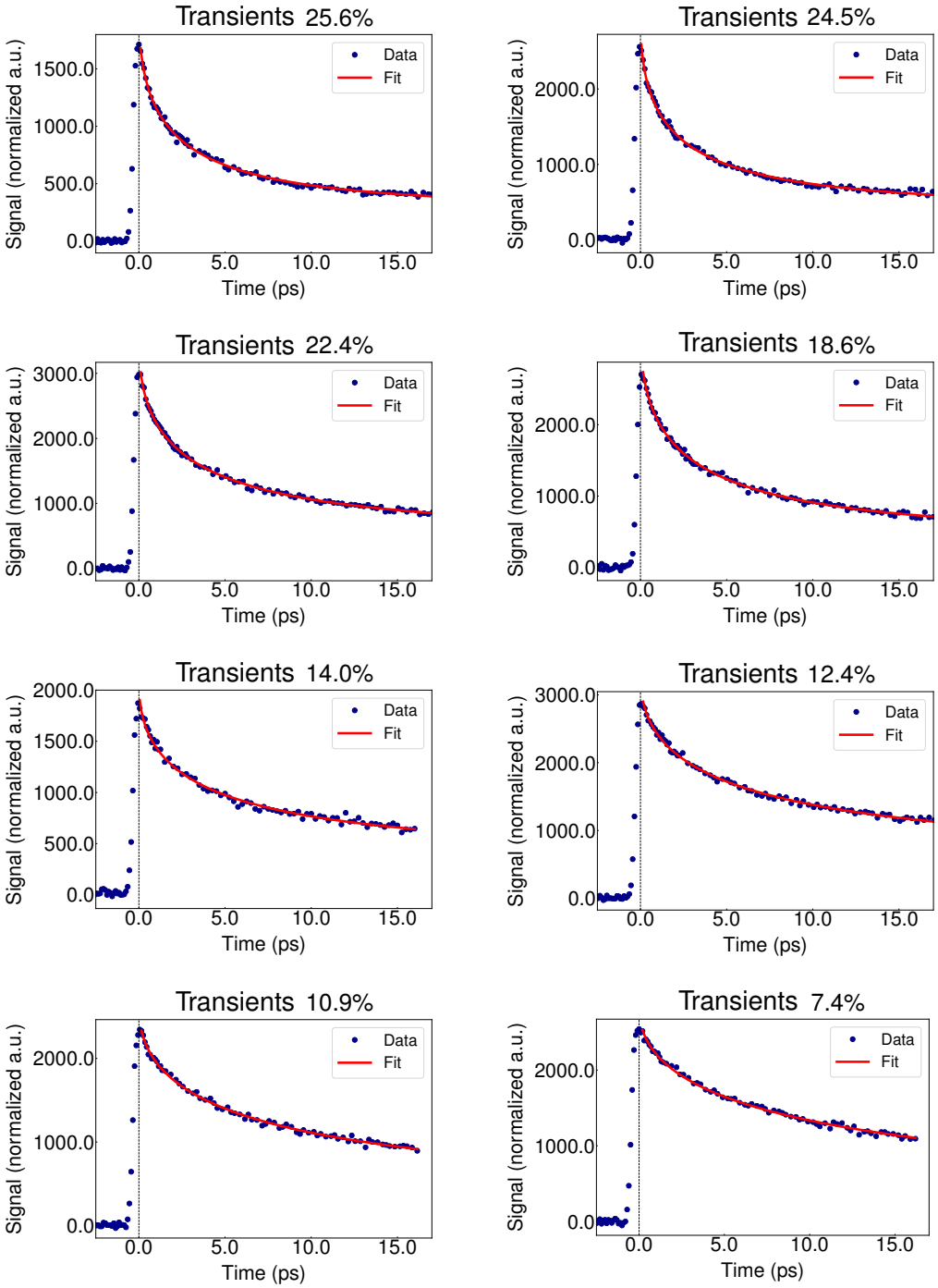


Figure 5.2: PL-upconversion transients for each measured sample with varying β-phase (β-phase content indicated in respective header). Experimental data in blue and a fit of Eq. 5.19 to the data in red.

indeed agree with the range of values in Fig. 5.3b. Only for sample 5 (7.4%), the amplitude A was limited to a realistic maximum value during the fitting process to obtain a sensible value for B/A.

Fig. 5.3a shows the PL transients together with the corresponding fits and the extracted variation of γ is shown in Fig. 5.3b as a function of β-phase fraction. As expected, γ tends to zero for low β-phase fraction; no ET occurs in a purely glassy-sample. An approximately linear relationship between γ and increasing β-phase content in the film is observed. The resulting Förster radii are noted in Table 5.1. A decreasing trend with increasing β-phase percentage is found. The magnitude of R_0 values obtained here from transient data is in agreement with the work of Khan et al. [161], who determined $R_0 = 8.2 \pm 0.6\,\text{nm}$ from PL-transients for one sample containing roughly 25% β-phase, using however a different sample preparation method and a different method to estimate the β-phase content and the chromophore densities.

Table 5.1: Förster radii from PL transients obtained by Eq. 5.1.

β-phase (%)	**R_0** (nm)
7.4	8.05
10.9	7.54
12.4	7.47
14.0	7.63
18.6	7.29
22.4	6.67
24.5	6.82
25.6	6.74

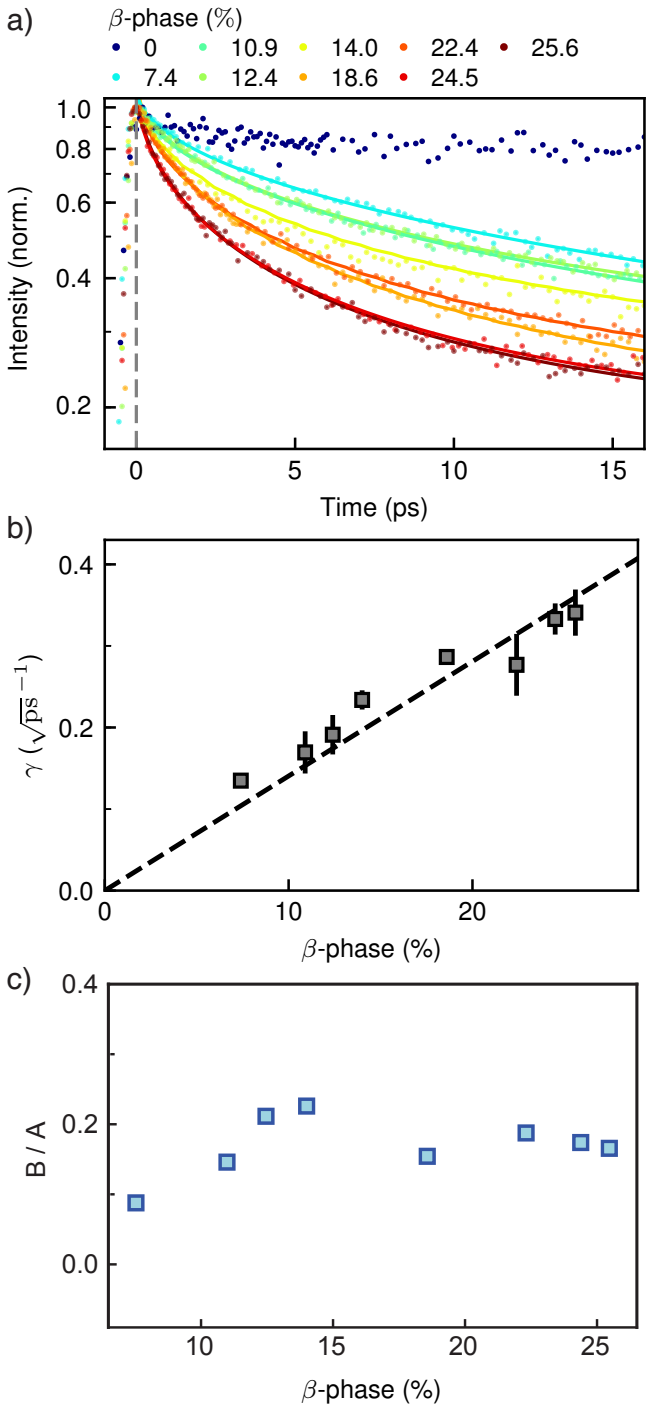


Figure 5.3: a) Normalised transients of PL emitted at 419 nm from PFO films with varying β-phase content and detected by PL-upconversion following excitation at 405 nm, plotted with a fit obtained by using Eq. 5.19 based on Förster theory. b) Fitting parameter γ reflecting the ET dynamics from glassy to β-phase, plotted as a function of β-phase percentage. The dashed line is a guide to the eye and represents a linear variation through the origin. c) The fitting parameters B/A obtained from fitting Eq. 5.19 to the transient data.

5.3.2 Calculating Förster Radius from Donor Emission and Acceptor Absorption Spectra

In a second step, the Förster radius is determined from spectral overlap between the donor emission and the acceptor absorption. A brief discussion of the expression used to calculate R_0 is given in Section 5.3.2.1. The theoretical background for the expression is outlined in more detail in Chapter 2. The results from the calculation of R_0 from time-integrated data are depicted in Section 5.3.2.2.

5.3.2.1 Expression for the Förster Radius

The Förster radius can be determined from time-integrated emission and absorption spectra. The expression to calculate R_0 is derived for through-space resonant ET based on Coulombic point dipole-dipole interactions between the energy donor and the energy acceptor and takes the following form [33, 58, 64]:

$$R_0 = \left(\frac{9 \ln(10) \kappa^2 \phi_D}{128 \pi^5 N_A n^4} \int I_D(\lambda) \epsilon_A(\lambda) \lambda^4 d\lambda \right)^{1/6}, \tag{5.22}$$

or in terms of units [64, 70]:

$$\frac{R_0}{\text{nm}} = 0.02108 \left(\frac{\kappa^2 \phi_d}{n^4} \left[\frac{J}{\text{mol}^{-1}\text{dm}^3\text{cm}^{-1}\text{nm}^4} \right] \right)^{1/6}, \tag{5.23}$$

where N_A is Avogadro's constant, κ denotes the geometric orientation factor of the donor and acceptor dipoles, ϕ_d is the PLQE of the glassy sample, n the refractive index and J is the overlap integral between donor (glassy-phase chain segments) emission dynamics and acceptor (β-phase chain segments) absorption spectra in units of $\frac{\text{dm}^3\text{nm}^4}{\text{mol cm}}$ in order to obtain R_0 in nm. These parameters, which are used to calculate R_0 are briefly discussed in the following:

Geometric orientation factor κ: Accounting for the relative geometric orientation of the donor and the acceptor dipoles, κ is defined as follows:

$$\kappa = \vec{\mu_d} \cdot \vec{\mu_a} - 3(\vec{\mu_d} \cdot \vec{R_{da}})(\vec{\mu_a} \cdot \vec{R_{da}}), \tag{5.24}$$

where $\vec{R_{da}}$ is the normalised vector along the donor-acceptor separation direction and $\vec{\mu_a}$ and $\vec{\mu_d}$ are the directions of the transition dipole moments of the acceptor and donor, respectively. κ takes values ranging from 0 for mutually perpendicular arrangement to 2 for collinear alignment [13]. For the calculation of R_0, $\kappa = 0.845 \times \sqrt{2/3}$ was used corresponding to a random, but fixed orientation of donors and acceptors randomly placed in the film [163, 170, 171]. The choice of κ is further discussed in Section 5.4.

PLQE, ϕ_d: Including the PLQE of the glassy sample (donor) in the expression for R_0 and using the total lifetime when calculating the Förster radii from PL-dynamics in Eq. 5.1 ensures that the results are comparable. This means that the Förster radius is referring to the distance at which ET is as likely to occur as any other de-excitation of the donor (as opposed to the distance at which energy transfer is as likely to happen as any other radiative de-excitation, which is sometimes used for the calculation of the Förster radius and is termed "effective Förster radius").

Refractive index, n: The PFO films were assumed to have a refractive index of $n_{eff} = 1.6$, which is a typical value for π-conjugated polymers [172–176]. This factor is kept constant for all samples and therefore does not influence any observed trends.

Overlap integral, J: Energy conservation requires that donor fluorescence and acceptor absorption overlap for the excitation ET to be possible. J describes the overlap of the normalised donor fluorescence I_d and the molar extinction coefficient ϵ_a of the acceptor [13, 64]:

$$J = \int I_d(\lambda)\epsilon_a(\lambda)\lambda^4 d\lambda. \tag{5.25}$$

The overlap between normalised emission from the glassy phase and absorption from the β-phase in the PFO thin films with varying β-phase content is schematically depicted in Fig. 5.5.

The molar extinction coefficient $\epsilon(\lambda)$ was calculated from the acceptor (β-phase) absorption $\alpha(\lambda)$ as:

$$\epsilon(\lambda) \;=\; \frac{\log_{10}(e)}{c_{\beta_{molar}}}\,\alpha(\lambda), \tag{5.26}$$

(for a detailed discussion see Section 4.4.1). The molar density of the β-phase chain segments $c_{\beta_{molar}}$ is obtained as (cf. Eq. 5.21 for c_β):

$$\begin{aligned} c_{\beta_{molar}} &= c_\beta \div N_A \\ &= 0.03321 \;\times\; \frac{\beta_{fraction}}{1-\beta_{fraction}} \;\times\; \mathrm{mol\,L^{-1}}. \end{aligned} \tag{5.27}$$

Careful analysis is necessary to ensure the use of the right units. I_d is a unit-less quantity, ϵ_a has units of $\frac{\mathrm{dm^3}}{\mathrm{mol\,cm}}$ if the film thickness is entered in cm and the molar concentration in $\frac{\mathrm{mol}}{\mathrm{L}}$. The resulting molar extinction coefficients ϵ_a as a function of wavelength for the samples with different β-phase content are displayed in Fig. 5.4. Here, the unit $\frac{\mathrm{dm^3}}{\mathrm{mol\,cm}}$ is to be understood as per mol PFO molecules in a thin film.

In order to obtain the normalised donor fluorescence I_d, the PL spectrum of the glassy sample (cf. Fig 4.5a) was normalised to the integrated area below the emission curve. This was achieved by using a spline-interpolation on the data and approximating the integral as

$$\sum_{i=1}^{N} f(x_i)\;\Delta x, \tag{5.28}$$

using steps of $\Delta x = 0.0001\,\mathrm{nm}$. This parameter was thoroughly tested to ensure that the approximation of the integral converges as Δx becomes smaller (convergence is achieved at much higher values of Δx).

The value of the overlap integral J was then calculated by approximating the integral as a sum as well, where $d\lambda$ was taken in 1 nm steps corresponding to the resolution of the absorption data.

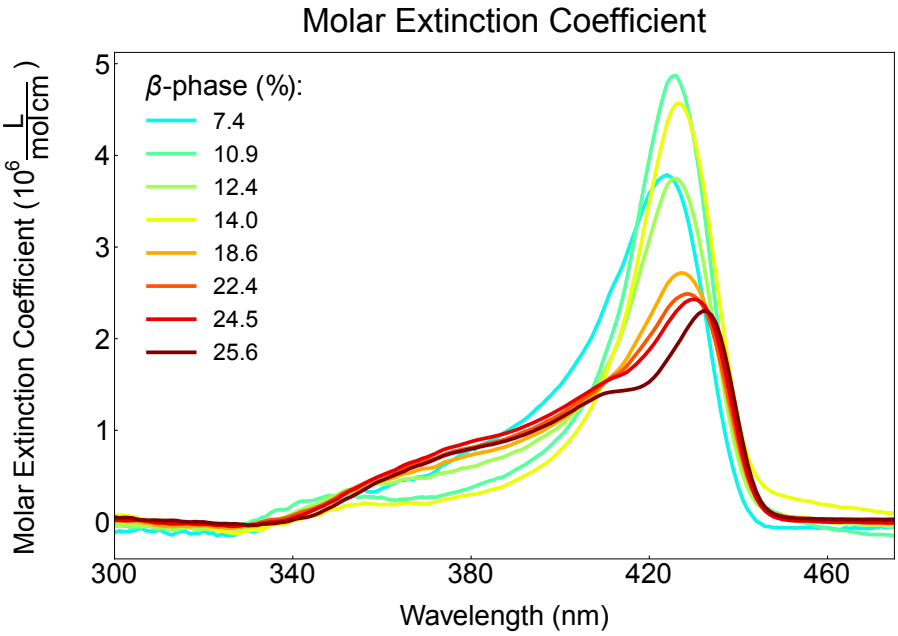


Figure 5.4: Molar extinction coefficient of the β-phase samples, obtained from the β-phase absorptance spectra (cf. Fig. 4.3) using Eq. 4.4. The ϵ_a for each sample was used to calculate the overlap integral to determine the Förster radius as a function of β-phase content in the PFO films.

5.3.2.2 Results from Time-Integrated Data

The resulting Förster radii are displayed in Table 5.2. There is a weakly decreasing trend for R_0 with increasing β-phase content. The β-phase peak of the molar extinction coefficient red-shifts with increasing β-phase content causing a reduction of the overlap as the 0-0 peak of the β-phase absorption shifts to wavelengths longer than that of the 0-0 peak of the glassy phase absorption (cf. Fig. 5.5). This small reduction in the overlap integral hence leads to a slight decrease in the calculated Förster radius with increasing β-phase fraction (see red diamonds, Fig. 5.6).

The Förster radii resulting from both, PL transients and spectral overlap are shown in Fig. 5.6. The values obtained from transient data were found to be higher than the values calculated from spectral overlap for all values of β-phase content in the PFO thin films. This observation is discussed in Section 5.4.

Table 5.2: Förster radii obtained from absorption and emission spectra.

β-phase (%)	**R_0** (nm)
7.4	5.92
10.9	6.18
12.4	5.96
14.0	6.2
18.6	5.75
22.4	5.7
24.5	5.68
25.6	5.62

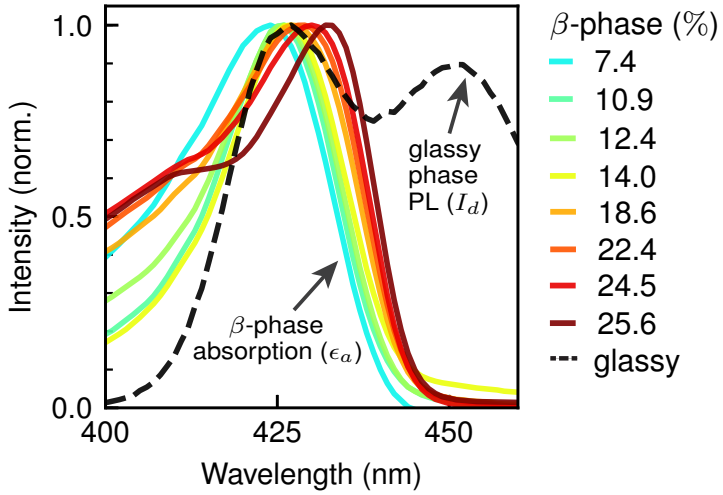


Figure 5.5: Overlap between the normalised emission (fluorescence, I_d) of the glassy phase and absorption (molar extinction coefficient, ϵ_a) of the β-phase in thin films of PFO, shown for a range of different β-phase fractions.

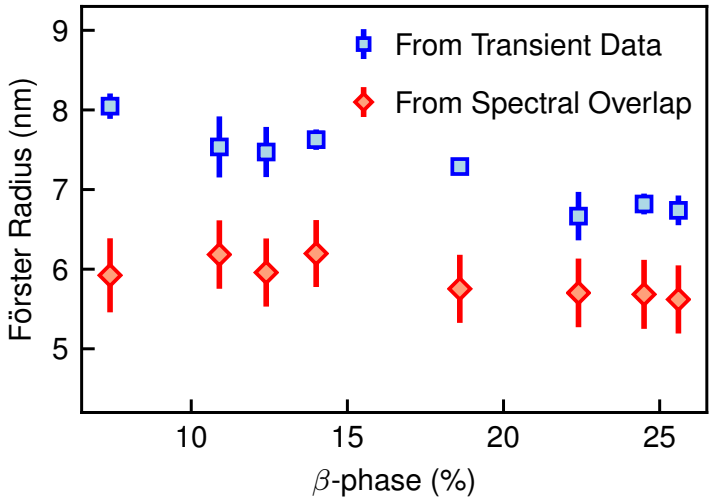


Figure 5.6: Förster radii for ET between glassy and β-phase chains in PFO, plotted as a function of β-phase percentage. Values were derived from transient data (blue squares); and from the spectral overlap between glassy phase (donor) emission and β-phase (acceptor) absorption (red diamonds).

5.4 Discussion

The discussion focuses on comparing the Förster radii obtained from spectral overlap and PL transients, which are displayed in Fig. 5.6 and noted in Tables 5.2, 5.1 Additionally, the β-phase dependence of FRET is addressed.

The apparent Förster radius was first derived from direct measurements of the PL decay transients, reflecting the actual transfer dynamics that may include additional processes, such as exciton diffusion within the host preceding the ET. Second, R_0 was calculated from the spectral overlap between donor emission and acceptor absorption according to standard Förster theory, which takes into account dipole-dipole coupling between donor and acceptor only. Both methods have separately been applied to PFO [147, 161, 162] but at the time of this study, a comparison of the two approaches had not yet been done. Contrasting the values of R_0 from both methods yields insights into the extent to which exciton diffusion and possible arrangement of the transition dipoles influence the ET in the films, which is discussed below.

The structure of this section is as follows: First, the results from both methods are briefly discussed separately. Second, the values of R_0 from the two different calculation approaches are compared and the difference is examined. Third, a link is made to the findings of Chapter 4.

The PL transients from the films with varying β-phase content are shown in Figs. 5.2 and 5.3a. The amount of β-phase in the film determines the PL intensity decay rate. For the film containing only the glassy phase of PFO, the PL intensity was observed to be near constant over the first 17 ps of the excitation decay, which is in agreement with TCSPC measurements showing a PL lifetime τ_g on the order of ns (see Section 4.4.3 for measurement of τ_g) and the assumption that $\tau_g >> t$ over the timescales t of the ET measurements, used in the derivation of Eq. 5.19. In contrast, the presence of β-phase segments leads to a rapid ET from the glassy phase segments as evident from the fast decay of the PL collected near the peak emission of the glassy

phase. The rapid ET is consistent with observations reported in other studies for individual PFO thin film samples containing a specific β-phase fraction [151, 161].

Eq. 5.19 was fitted to the PL transients to obtain the parameter γ, which is depicted in Fig. 5.3b. The approximately linear increase in γ represents a more rapid PL decay indicating faster ET from glassy chain segments to β-phase chain segments for higher β-phase fractions. The Förster radius is derived from the fitted PL data through Eq. 5.1 taking into account both, γ and the concentration of β-phase chain segments in the films c_β, resulting in the slightly decreasing trend for R_0 with increasing β-phase content displayed in Fig. 5.6 (blue squares).

By extracting the value of R_0 from the transient PL data, a systematic investigation on how varying β-phase fractions in PFO thin films affect the ET becomes possible. Such an investigation is virtually impossible to carry out from simple analysis of the PL emission spectra alone given that transfer of excitations from the glassy to the β-phase clearly occurs with close to 100% efficiency even when only small percentages of β-phase are present (cf. Fig. 4.5a).

Using steady-state absorption and emission measurements, Eq. 5.23 was used to determine the values of R_0 as function of β-phase present in the film, depicted as red diamonds in Fig. 5.6. The Förster radius decreases with increasing β-phase fraction as the β-phase absorption peak red-shifts and the spectral overlap is decreased as seen in Fig. 5.5.

For both calculation methods therefore, the value of R_0 decreases with increasing β-phase content. These correlations confirm that the changes in spectral overlap indeed cause R_0 to decline as the percentage of β-phase is increased, signifying that the resonance condition for the ET between glassy- and β-phase chain segments alters with varying β-phase content. However, despite the good agreement between general trends in R_0 as a function of β-phase content in the film, the actual values of R_0 derived from the PL transients are found to be substantially higher than expected

from the spectral overlap. Two possibilities for this discrepancy are discussed in the following, which are i) the diffusion of excitons within the glassy matrix prior to ET and ii) local alignment or correlation between transition dipole moments.

For the former mechanism, a dynamic migration of excitons within the glassy matrix may bring them effectively into closer proximity to β-phase segments than would be estimated from the β-phase segment concentration alone. In the calculation of R_0, ET is assumed to occur from an acceptor that was directly excited by the laser. An additional multiple-step exciton diffusion on or in-between glassy-phase chain segments (donors) prior to the ET will increase the effectively experienced Förster radius [13, 177, 178] by first allowing excitations to diffuse to within the capture radius of an acceptor. Exciton diffusion is captured in the PL dynamics only and can therefore account for the higher values of R_0 obtained from the PL transients as compared to the values of R_0 deduced from spectral overlap. Exciton diffusion either occurs between segments on the same polymer chain (intrachain) or between chains (interchain), which both increase the Förster radius. Exciton diffusion in PFO films has also been observed elsewhere [144, 147, 148, 162] and is therefore highly likely to contribute to the enhancement of Förster radii effectively experienced. It is noteworthy, that on-chain as well as interchain exciton diffusion processes are expected to be sensitive to small variations in chain conformation and film microstructure [149, 159, 179], highlighting the susceptibility to details of film preparation methods [180, 181].

As a second possible contribution, the difference in R_0 could be caused by some degree of local alignment between the donor and acceptor dipoles, i.e. the glassy- and β-phase chain segments. The transition dipoles have been assumed to be oriented randomly in the calculation of R_0 from spectral overlap, using a value of $\kappa = 0.845 \times \sqrt{2/3}$ for the geometric orientation factor. This value was derived

by Maksimov and Rozman [170] for fixed donors and acceptors in random positions and with randomly orientated transition dipole moments within a solid. However, the second assumption will not hold if some alignment or correlation between the orientation of adjacent chains exists. In the limiting case that all transition dipoles of donors and acceptors are oriented parallel to each other (still assuming random positions), the geometric orientation factor would take a value of $\kappa = 0.943 \times \sqrt{2/3}$ [170], which would increase R_0 by 0.2 to 0.25 nm. However, such a slight increase is too small to account for the much larger differences that were observed between the values of R_0 derived from PL transients and those expected from spectral overlap calculations as shown in Fig. 5.6 and listed in Tables 5.1, 5.2.

Such alignment of donor and acceptor dipoles would also require a degree of local ordering, which is unlikely to be substantial inside these thin polymer films. For example, there is no evidence that isolated domains of locally aligned chains form but observation of well-intermixed glassy and β-phases in PFO films has been reported [146, 147]. Well-intermixed phases are also in agreement with the complete ET observed here as no glassy phase steady-state PL is observed for the films containing some fraction of β-phase (cf. Fig. 4.5a). It is theoretically possible that a glassy chain segment formed adjacent to a β-phase segment as part of the same chain exhibits a local correlation between transition dipole orientation. However, intrachain ET will be less efficient than interchain transfer, because of the closer proximities in the latter case. Either way, such local correlations between dipole orientations will only give rise to minute increases in the expected Förster radii, making it unlikely that they can account for the observed boost in R_0 deduced from spectral overlap. Therefore, the enhancement of the observed ET must originate from the assistance of exciton diffusion within the glassy phase prior to ET as discussed previously.

Finally, a brief comparison to the previous chapter is appropriate as both studies were conducted with the same set of PFO thin film samples. In Chapter 4,

planarisation, extension of β-phase chromophores and an increase in PLQE with increasing β-phase fraction in the PFO thin films film were found. However, while both the PLQE (cf. Fig. 4.8) and the ET parameter γ (cf. Fig. 5.3b) similarly increase with β-phase content of the PFO film, these two trends are not directly linked and ET is not more efficient with increasing β-phase. As the PL spectra of the PFO films (cf. Fig. 4.5a) show, the ET efficiency is close to 100% even for films containing a low percentage of β-phase as no glassy phase emission can be detected. Therefore, while the speed of transfer increases with increasing β-phase fraction, almost all excitations still transfer from the glassy to the β-phase before they are able to recombine for all films with varying β-phase content. The rise in PLQE with β-phase fraction is therefore governed exclusively by the planarisation and extension of β-phase chromophores as the fraction of β-phase in the film is increased, as discussed in Chapter 4 and is not influenced by ET.

One more detail should be considered: In the discussion of the β-phase absorption spectra, possible small distortions in the β-phase absorption spectra stemming from the commonly used method of β-phase determination were mentioned. It is therefore sensible to comment on whether such small distortions would influence the calculation of the Förster radii from spectral overlap between glassy phase emission and β-phase absorption. The calculation of R_0 mostly includes the 0-0 peak of the β-phase absorption, which is sufficiently red-shifted from the absorption onset of the glassy phase, where any slight distortions in determining the β-phase absorption would be prominent. Thus no influence on R_0 is expected.

5.5 Summary and Conclusion

This chapter focused on investigating how the fraction of β-phase chains present in PFO thin films affects Förster resonant energy transfer from glassy- to β-phase chain segments. To this end, a series of well-comparable PFO thin films with varying β-phase content was studied and the Förster radius, which is a distance measure for energy transfer, was obtained from measurements of the PL dynamics as well as from steady-state absorption and emission measurements.

Resonant energy transfer from the glassy- to the β-phase chain segments in PFO films does not become more efficient, but is an overall faster process with increasing β-phase content. By comparing the values of the Förster radii obtained from spectral overlap calculations to those extracted from measurements of transient PL dynamics, the Förster radius was found to be enhanced by exciton diffusion within the glassy phase occurring prior to energy transfer.

A major benefit of the study presented in this chapter is the use of a well-defined series of PFO films with a wide range of β-phase fractions, fabricated through a single processing method. This consistency is decisive to allow for the fundamental investigation into how energy transfer in PFO films is affected by the conformational changes occurring with increasing β-phase content.

6

Energy Transfer between Layers of Photoexcited Organic Semiconductor and Metal Halide Perovskite

Contents

6.1 Background and Motivation 95
6.2 Sample Preparation 97
6.2.1 Substrate Cleaning 97
6.2.2 $MAPbI_3$ Layer 97
6.2.3 Polymer Layers 98
6.3 Absorption and PL Spectra 100
6.3.1 F8BT 101
6.3.2 Super Yellow 103
6.3.3 P3HT 105
6.3.4 PTAA 106
6.3.5 $MAPbI_3$ 108
6.4 PLQE 109
6.5 PL Lifetimes 111
6.6 Fluorescence Decay and ET Efficiency Model 112
6.6.1 FRET in Two-Layer Geometry 114
6.6.2 PL Decay Modelling 117
6.6.3 Calculation of ET Efficiency 122
6.7 Discussion 126
6.8 Summary and Conclusion 131

Reproduced in part from work submitted for publication by Eggimann et al. in Ref. [182].

6.1 Background and Motivation

Metal halide perovskite (MHP)-based solar cells offer great potential as active layers in solar cells owing to favorable optoelectronic properties such as band-gap tunability [183, 184], high charge-carrier mobilities [185], low exciton binding energies [41] and high defect tolerance [186]. Immense progress towards commercialisation has been made with lab-scale perovskite-based solar cells presently reaching efficiencies of up to 25.2% [187]. One important challenge in this area is the optimization of the charge-transport layers (CTL)s [188–190]. CTLs have become an essential component of perovskite device architectures because the facile migration of mobile ions within the MHP prevents reliable doping, meaning that the conventional p-n junction approach may prove too difficult to accomplish for MHP layers [191, 192]. Current state-of-the-art devices use organic semiconductors as CTLs which offer many benefits such as easy tailorability, low-cost and large-scale fabrication [14, 15, 190] and surface passivation for significantly improved charge extraction at the electrodes [188, 191]. A variety of different organic semiconductors, including π-conjugated polymers are employed, particularly in multijunction MHP devices. Importantly, the general architecture of these solar cells means that a CTL is usually the first semiconductor in the device to interact with light [193, 194]. One issue that has been highlighted in this context is parasitic absorption of light in the CTL, which can reduce device performance [195–199] by lowering the amount of light that reaches the MHP to generate charge-separated electrons and holes. It is therefore of great importance to understand the interplay between the incoming light, the organic semiconductor layer and the MHP.

Parasitic absorption of sunlight by a front CTL will lead to efficiency losses as some of the incoming energy does not reach the MHP layer. It may affect both front

CTLs in single-junction devices, and those embedded amidst more complex tandem architectures. However, efforts to reduce such effects have to date mostly focused on simply choosing CTLs with low absorption coefficient in the visible region of the spectrum. This approach severely restricts the choice of semiconductors available, which is undesirable, given that CTLs also need to comply with a large number of other requirements, including sufficiently high charge-carrier mobilities and correct energetic band alignment with the conduction band or the valence band of the active MHP layer. Interestingly, an additional material space may be opened if parasitic absorption by the organic semiconductor can be counteracted by subsequent energy transfer (ET) to the MHP. As part of this mechanism, light first creates a bound electron-hole pair (exciton) in the molecular CTL, whose oscillating electronic dipole moment then couples with the electronic transitions available in the MHP. Radiationless transfer may then occur from the CTL to the MHP, converting an exciton in the CTL into an electron-hole pair in the MHP, which is extracted as photocurrent through the respective CTLs. In this context, Förster resonant ET (FRET) offers a widely used tool for quantifying the efficiency of ET as the theory has been extended to a wide range of applications and sample geometries, [93, 95–100]. For the design of molecular CTLs in MHP solar cells, an understanding of the ET between the photoexcited organic semiconductor and the MHP layer is clearly of great importance, however an in-depth investigation was still outstanding at the time of this study.

In this chapter, possible ET between a photoexcited organic semiconductor and MHP are investigated by combining experimental data with FRET theory. The efficiency of ET between a photoexcited organic semiconductor layer and a MHP is modeled based on experimental observation of ET between layers of different π-conjugated polymers and methylammonium lead iodide ($MAPbI_3$). Thereby, the following question is addressed: ***How can efficient energy transfer between layers of organic semiconductor and metal halide perovskite be achieved?***

6.2 Sample Preparation

Four different polymers (Super Yellow, F8BT, P3HT and PTAA) were deposited on $MAPbI_3$ layers on quartz substrates ($MAPbI_3$:quartz) and on z-cut quartz substrates directly through dynamic spin-coating from solution. For each sample, 40 µL of the polymer solution were deposited on pre-cleaned quartz substrates for the polymer-only films and on evaporated $MAPbI_3$ (see Section 6.2.2) for the polymer-$MAPbI_3$ films. The spin speed was varied for each sample to achieve a difference in thickness (see below for each sample separately and Table 6.1 for a thickness overview), the spin process duration was kept at 45 s for all samples. All steps apart from the cleaning of the substrates were carried out under nitrogen atmosphere. The films were kept in a nitrogen glovebox before and in between measurements. Film thickness was measured using a DEKTAK profilometer and was cross-checked with the absorption data. The error of the film thickness value is estimated from repeated measurements on different spots on the films to be of the order of 10% of the determined film thickness.

6.2.1 Substrate Cleaning

The z-cut quartz substrates were cleaned with Hellmanex solution followed by a thorough rinse with deionized water. The substrates were then washed with acetone, isopropanol and ethanol. In a last cleaning step, the substrates were plasma etched in O_2 for 10 minutes.

6.2.2 $MAPbI_3$ Layer

$MAPbI_3$[1] layers were fabricated using thermal evaporation (see Ref. [200]). In brief, MAI and PbI_2 were placed in separate crucibles and the substrates were mounted

[1] The $MAPbI_3$ layers as well as P3HT and PTAA films were fabricated by Dr J. Patel.

on a rotating substrate holder to ensure uniform film deposition. The temperature of the substrates was kept at 21 °C throughout the deposition. The chamber was evacuated to reach a high vacuum ($\sim 10^{-6}$ mbar), before heating of the PbI_2 and the MAI. The substrates were then exposed to the vapor with an average deposition rate of 0.4 Å s^{-1}. The rates of both the MAI and PbI_2 were monitored using a quartz crystal microbalance. The thickness of the $MAPbI_3$ thin film was set by controlling the exposure time of the substrates to $MAPbI_3$ precursor vapor. Three film thicknesses of $MAPbI_3$ were used in this work: 450 nm (F8BT and Super Yellow samples), 260 nm (PTAA and P3HT control samples), 65 nm (P3HT samples).

6.2.3 Polymer Layers

6.2.3.1 F8BT

F8BT $(C_{35}H_{42}N_2S)_n$ (poly(9,9-dioctylfluorene-alt-benzothiadiazole)) with an average molecular weight of $M_w > 20\,000$ (CAS number 210347-52-7) was purchased from Sigma-Aldrich. The "thick" F8BT samples used for this study were spin-coated from a solution of F8BT in anhydrous toluene with a concentration of 10 mg mL^{-1} at a spin speed of 2000 rpm, the "thin" samples from a solution with a concentration of 5 mg mL^{-1} of F8BT in anhydrous toluene at 5000 rpm.

6.2.3.2 Super Yellow

Super Yellow light-emitting PPV copolymer with $M_w \geq 1\,300\,000$ (CAS number 26009-24-5) was purchased from Sigma-Aldrich. The Super Yellow samples were spin-coated from a solution of 5 mg mL^{-1} of the polymer in anhydrous toluene, the "thick" sample at a spin speed of 1000 rpm, the "thin" sample at 3000 rpm. An additional sample was spin-coated at 4000 rpm, which was of comparable thickness with the sample spin-coated at 3000 rpm. All measurements from this sample were in excellent agreement with the data presented henceforth of the 3000 rpm sample.

6.2.3.3 P3HT[1]

A solution was prepared containing P3HT (Poly(3-hexylthiophene-2-5-diyl), purchased from Sigma Aldrich (CAS number 104934-50-1), dissolved in anhydrous toluene at a concentration of 15 mg mL^{-1}. The solution was then deposited on the quartz directly, or on the $MAPbI_3$ thin film on quartz by dynamic spin coating with 2000 and 6000 rpm for the "thick" and "thin" films, respectively. The films were prepared on a thin $MAPbI_3$ (65 nm) layer on a z-cut quartz substrate to be able to separate absorption components from the polymer and the $MAPbI_3$. Additionally, two control samples of different P3HT thickness were prepared on a 260 nm $MAPbI_3$ film, showing the same photo-physical behaviour than the films on the thinner $MAPbI_3$ layer on quartz.

6.2.3.4 PTAA[1]

A solution was prepared containing PTAA (Poly[bis(4-phenyl)(2,4,6-trimethylphenyl) amine]), purchased from LUMTEC (CAS number 1333317-99-9), dissolved in anhydrous toluene at a concentration of 15 mg mL^{-1}. The solution was then deposited on the quartz substrate directly or on the $MAPbI_3$ layer by dynamic spin coating with different spin speeds. The spin speeds used were 2000 rpm and 6000 rpm for the "thick" and "thin" films, respectively.

Table 6.1: Thickness of the "thick" and "thin" polymer layers.

	F8BT	**Super Yellow**	**P3HT**	**PTAA**
thin polymer : quartz	30 nm	30 nm	42 nm	23 nm
thick polymer : quartz	80 nm	60 nm	77 nm	55 nm
thin polymer : $MAPbI_3$: quartz	25 nm	23 nm	40 nm	35 nm
thick polymer : $MAPbI_3$: quartz	78 nm	50 nm	92 nm	100 nm

To discern the efficiency of the ET between a photoexcited polymer layer and the underlying $MAPbI_3$, i.e. how much of the energy from incoming light undesirably absorbed by the polymer is transferred to the $MAPbI_3$ layer, first the photophysical properties of polymer films deposited on a $MAPbI_3$ layer are investigated. To this end, first, absorption, PL, PLQE and PL decay measurements are presented in sections 6.3-6.5. Second, the ET efficiency is modelled, which is outlined Section 6.6.

6.3 Absorption and PL Spectra

This section presents the absorption (O.D.) and PL spectra from the different polymers deposited on a quartz substrate directly and on top of a $MAPbI_3$ layer on a quartz substrate ($MAPbI_3$:quartz), as well as the absorption and PL spectra from the $MAPbI_3$ layers themselves.

Absorption spectra were calculated from background light corrected reflection (R) and transmission (T) as $-\ln(T/1-R)$. The spectra were base-line corrected for scattering. Reflection and transmission were measured with the FTIR spectrometer (see Section 3.4). As light sources, a tungsten halogen lamp (NIR source) and a deuterium lamp were used and different spectral ranges were detected with a gallium phosphide (GaP) and a silicon (Si) diode detector. Absorption spectra using different source/detector combinations are shown as one setting does not cover the full range from the low wavelength absorption of the polymers to the higher absorption edge of the $MAPbI_3$. The source/detector combination is indicated for each measurement individually in the figure caption.

All PL spectra are corrected for spectral response with a known lamp spectrum, also accounting for any filters used. Excitation wavelength and fluence are listed for each polymer individually in Table 6.3.

The thickness of the polymer layers is referred to as “thick” and “thin” as introduced in Section 6.2. Actual thicknesses are given in Table 6.1.

6.3.1 F8BT

Absorption spectra of the F8BT films on quartz and on $MAPbI_3$:quartz are shown in Fig. 6.1. Fig. 6.2 shows the corresponding relative and normalised PL spectra. Reduced PL intensity is observed for the thin F8BT sample on $MAPbI_3$:quartz. No significant changes in PL lineshape were observed for the films of different thickness of F8BT.

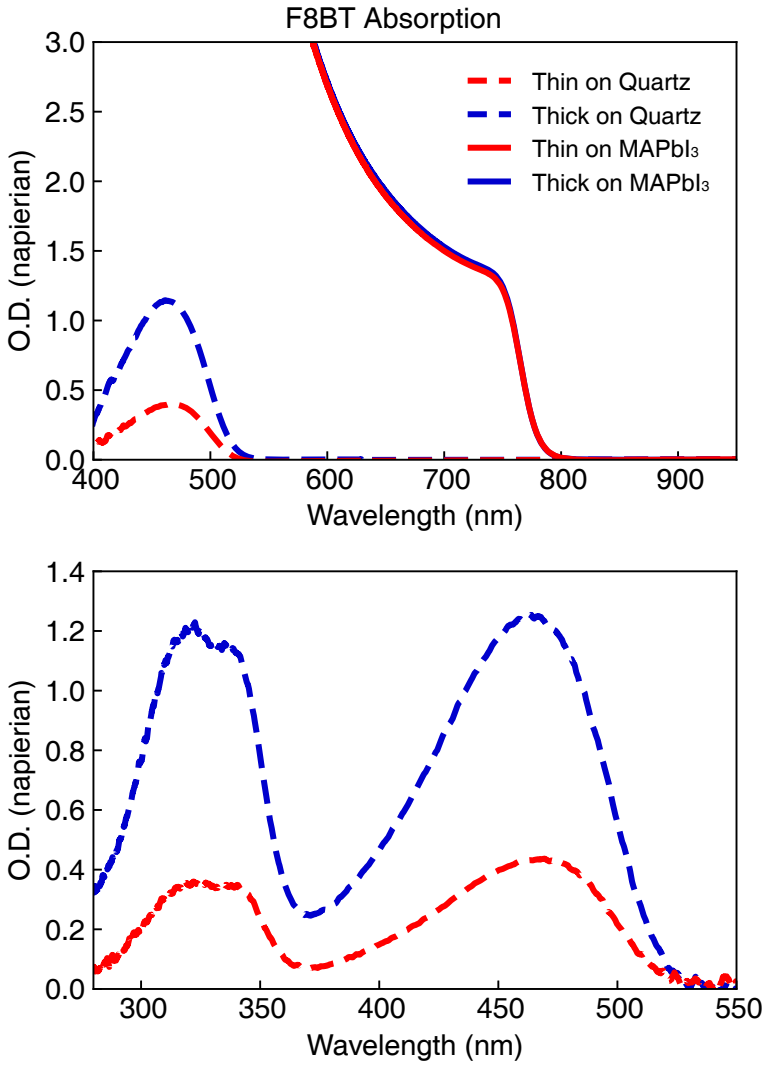


Figure 6.1: Top: Absorption of thin (red) and thick (blue) F8BT films on quartz (solid line) and on $MAPbI_3$:quartz (dashed line) substrates, measured with NIR source and Si detector. Bottom: Absorption of thin and thick F8BT films on quartz substrates, measured with Deuterium lamp and GaP detector.

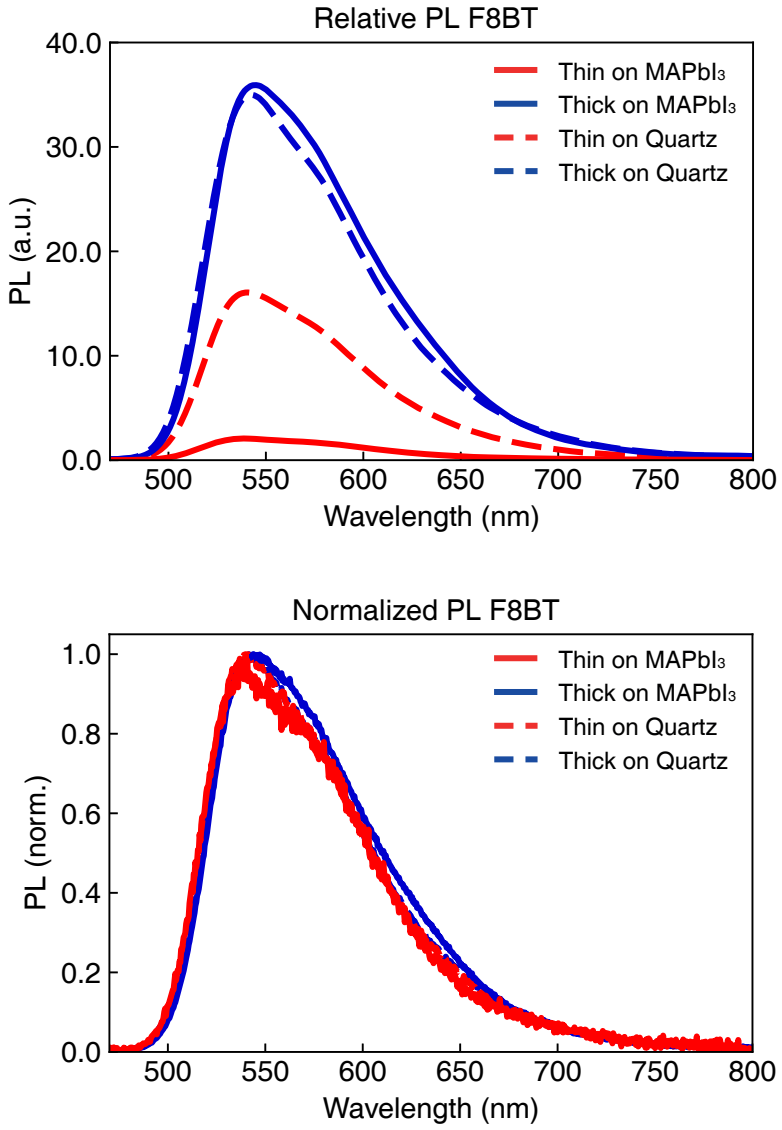


Figure 6.2: PL spectra from F8BT for thick (blue) and thin (red) films on quartz (dashed line) and on $MAPbI_3$ (solid line). Top: Relative intensity of the PL. Bottom: Normalised PL Spectra.

6.3.2 Super Yellow

For the thick and thin Super Yellow films on quartz and on $MAPbI_3$:quartz, absorption spectra are shown in Fig. 6.3 and PL spectra are shown in Fig. 6.4. For the thin sample on $MAPbI_3$:quartz, reduced PL intensity is observed. The PL lineshape shows slight changes for the thin and thick films on $MAPbI_3$:quartz, which might stem from small thickness-dependent morphological differences of the material when deposited on $MAPbI_3$.

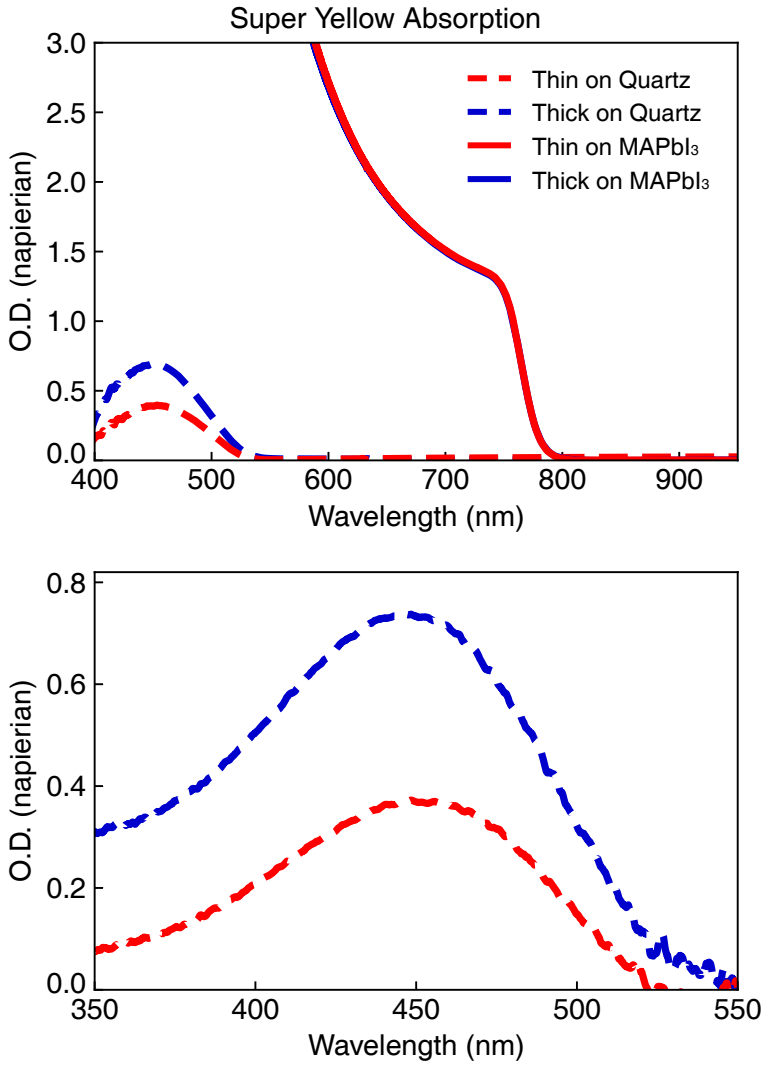


Figure 6.3: Top: Absorption of thin (red) and thick (blue) Super Yellow films on quartz (solid line) and on $MAPbI_3$:quartz (dashed line) substrates, measured with NIR source and Si detector. Bottom: Absorption of thin and thick Super Yellow films on quartz substrates, measured with Deuterium lamp and GaP detector.

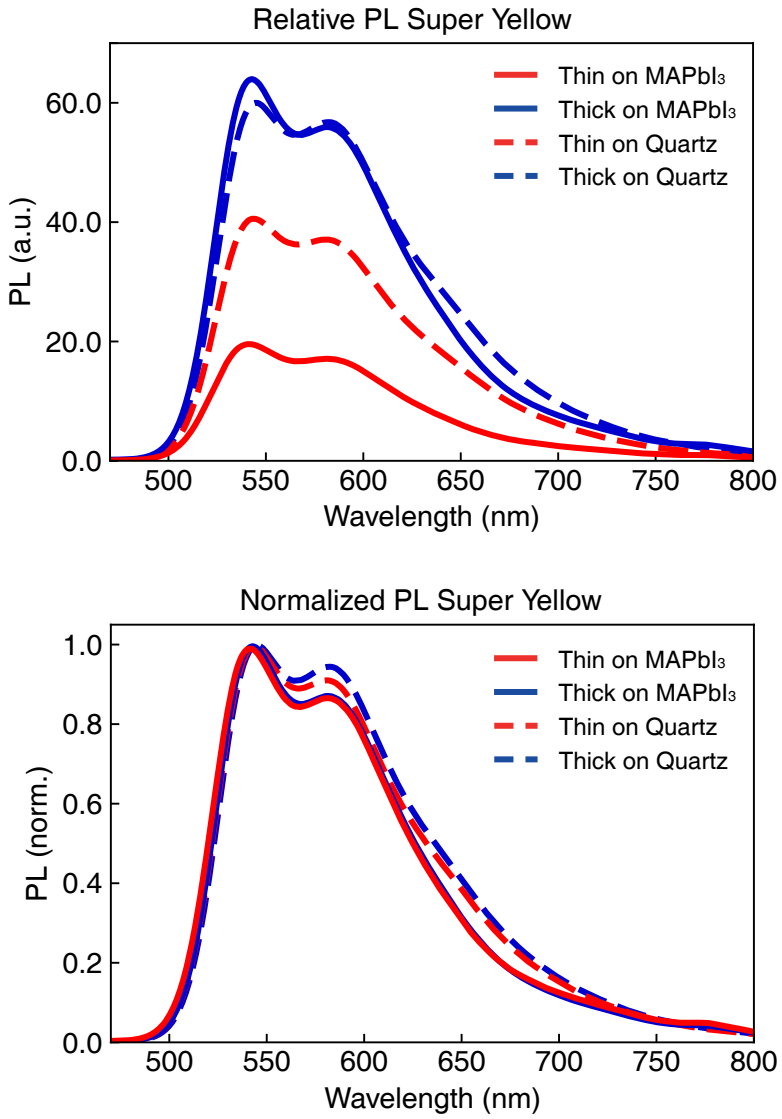


Figure 6.4: PL spectra from Super Yellow for thick (blue) and thin (red) films on quartz (dashed line) and on $MAPbI_3$:quartz (solid line) substrates. Top: Relative intensity of the PL. Bottom: Normalised PL Spectra.

6.3.3 P3HT

Figs. 6.5 and 6.7 show absorption and PL spectra of the P3HT films on quartz and on $MAPbI_2$:quartz. PL intensity from the P3HT films correlates with film thickness and no change in PL intensity was observed. Therefore, only normalised PL spectra are shown. Significant changes in PL lineshape were observed, which are discussed in Chapter 7.

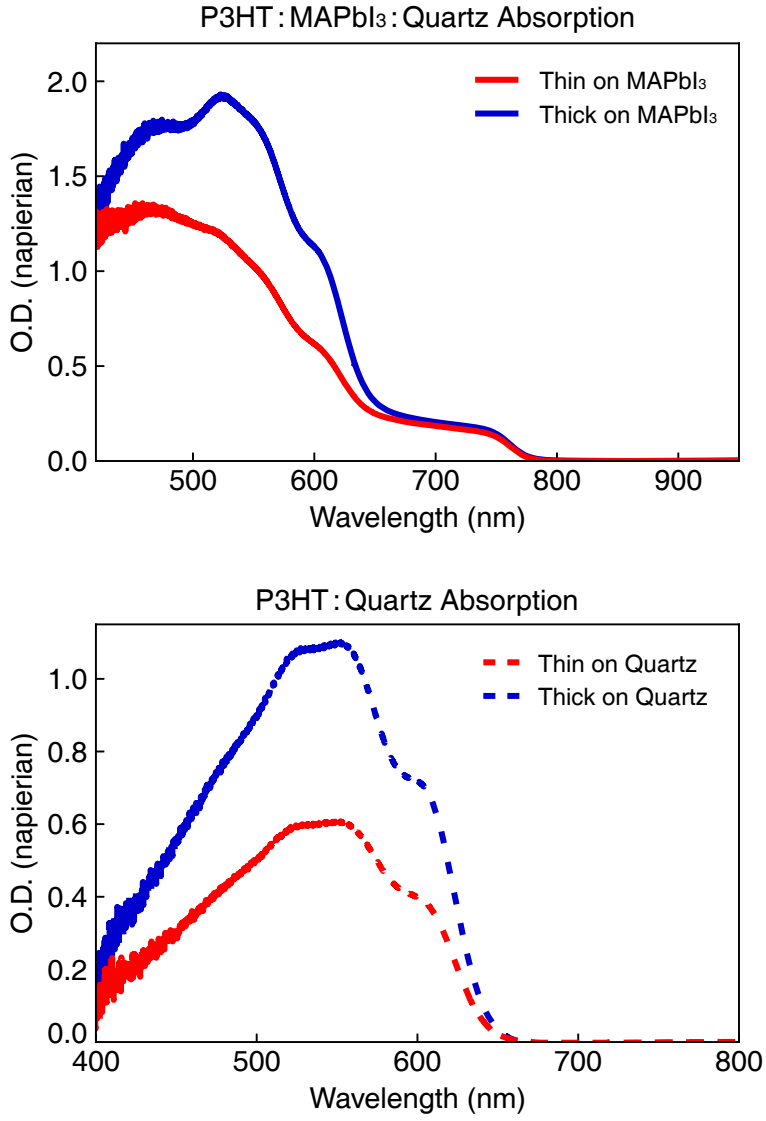


Figure 6.5: Top: Absorption of thin (red) and thick (blue) P3HT films on $MAPbI_3$:quartz (solid lines) substrates. Bottom: Absorption of thin and thick P3HT films on quartz (dashed lines) substrates, both measured with NIR source and Si detector.

6.3.4 PTAA

Absorption and PL spectra of the PTAA films on quartz and on $MAPbI_3$:quartz are depicted in Fig. 6.6 and Fig. 6.8, respectively. Only normalised PL is shown as the PL intensity from the PTAA films correlates with film thickness and no change in PL intensity was observed. Only very small, but not significant changes are found for PL lineshape.

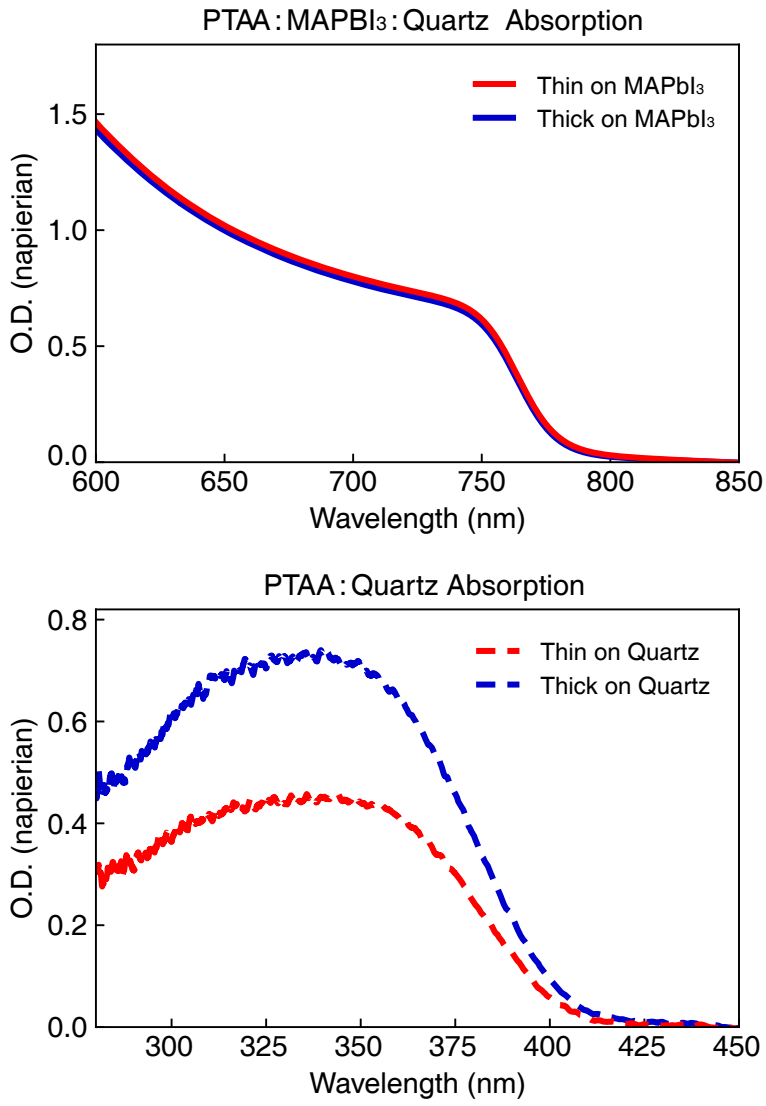


Figure 6.6: Top: Absorption of thin (red) and thick (blue) PTAA films on $MAPbI_3$:quartz (solid lines) substrates, measured with NIR source and Si detector. Bottom: Absorption of thin and thick PTAA films on quartz (dashed lines), measured with Deuterium lamp and GaP detector.

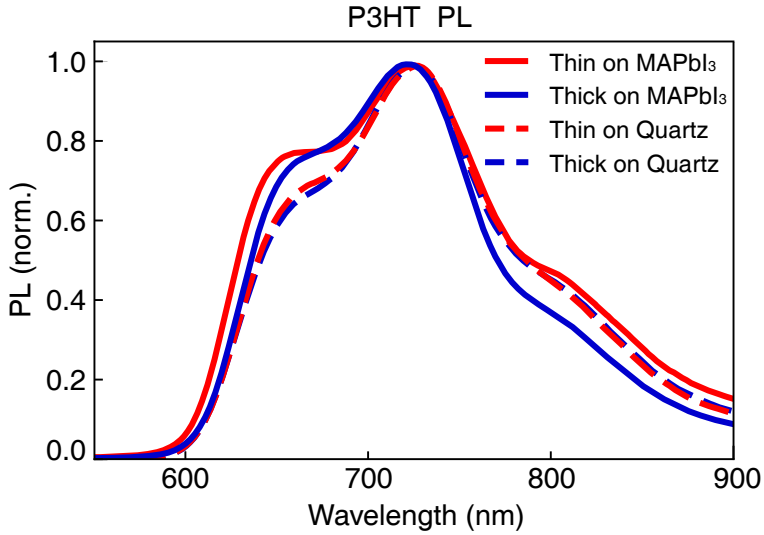


Figure 6.7: Normalised PL spectra from P3HT for thick (blue) and thin (red) films on quartz (dashed line) and on $MAPbI_3$:quartz (solid line) substrates.

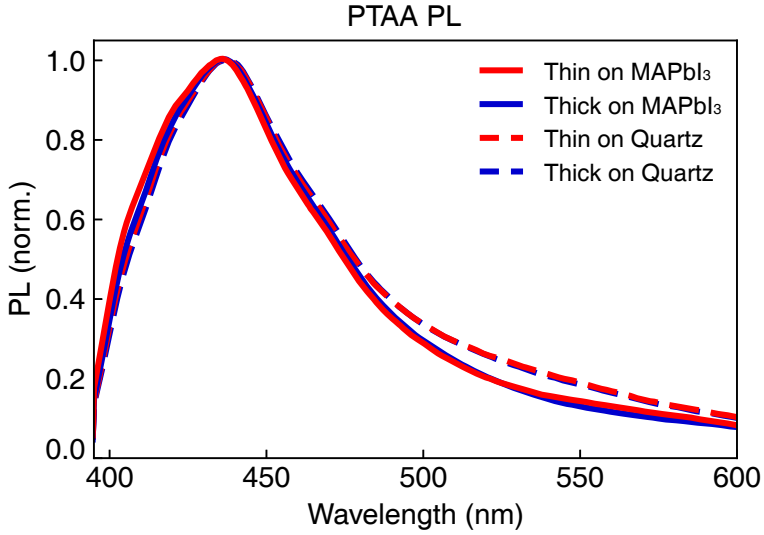


Figure 6.8: Normalised PL spectra from PTAA for thick (blue) and thin (red) films on quartz (dashed line) and on $MAPbI_3$:quartz (solid line) substrates.

6.3.5 $MAPbI_3$

Figs. 6.9 and 6.10 show absorption and PL of the 450 nm and 260 nm $MAPbI_3$ layers on z-cut quartz substrates ($MAPbI_3$:quartz). Absorption and PL from the 65 nm $MAPbI_3$ layer are plotted with the P3HT absorption (Fig. 7.3) and PL (Fig. 7.5) in Chapter 7. For the PL measurements, the films were excited at 400 nm with a fluence of the order of 20 $nJ\,cm^{-2}$.

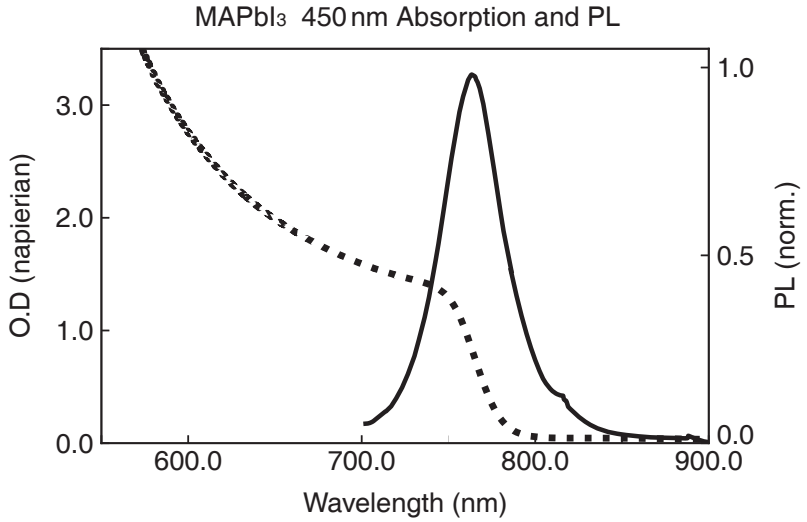


Figure 6.9: Absorption and PL from the 450 nm $MAPbI_3$:quartz, used as a substrate for the F8BT and Super Yellow films, measured with NIR source and Si detector

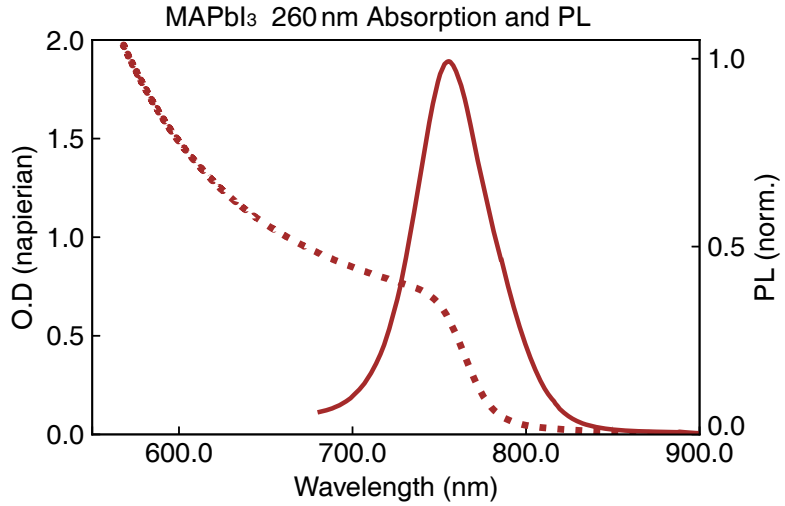


Figure 6.10: Absorption and PL from the 260 nm $MAPbI_3$:quartz, used as a substrate for the PTAA films, measured with NIR source and Si detector

6.4 PLQE

PLQE, ϕ, was measured for all polymers. PLQE can be obtained by comparison of integrated PL intensity from the sample with a known PLQE standard with ϕ_{ref}, taking into account the difference in absorption at the excitation wavelength λ_{exc} [201]:

$$\phi_{sample} = \phi_{ref} \frac{I_{sample}(\lambda_{PL})}{I_{ref}(\lambda_{PL})} \frac{A_{ref}(\lambda_{exc})}{A_{sample}(\lambda_{exc})}, \tag{6.1}$$

where $I_{sample/ref}(\lambda_{PL})$ is the integrated PL intensity over the range of polymer/ reference emission and $A_{sample/ref}(\lambda_{exc})$ is the absorbance at the excitation wavelength for the PL of the polymer or reference. The reference standard used in this work is the well-known fluorescence standard Rhodamin 6G (Rhodamine 6G analytic standard from Sigma Aldrich, molar weight: $479\,\mathrm{g\,mol^{-1}}$, $\phi_{ref} = 0.95$), which was diluted in solution with ethanol at a concentration of 0.8 mM. The suitability of this concentration was tested in previous work [202]. PL and Absorbance (O.D.) of the Rhodamine 6G solution are shown in Fig. 6.11. The polymer films degrade under simultaneous exposure to ambient air and laser emission, which is why the films were measured in a vacuum cell. As little light scattering is expected for these films, the use of the vacuum cell instead of an integrating sphere should not lead to substantial errors. Additionally, for the ET modelling, the comparison between data and model results is only sensitive to relative PLQE. The PLQE of Super Yellow was obtained by referencing with the fluorescence standard Rhodamine 6G in dilute solution in a quartz cuvette and was then used as a reference for the other polymers. Special care was taken for adjusting the focus position for each film. The resulting PLQE values are given in Table 6.2. The error given indicates the range of values obtained from a range of measurements for each polymer from thick and thin polymer films referenced either to the Rhodamine 6G solution (Super Yellow) or to the thick and thin Super Yellow samples (all other polymers).

Table 6.2: PLQE of the different polymers.

	F8BT	Super Yellow	P3HT	PTAA
PLQE	$71 \pm 1\%$	$26 \pm 3\%$	$1 \pm 0.3\%$	$0.5 \pm 0.03\%$

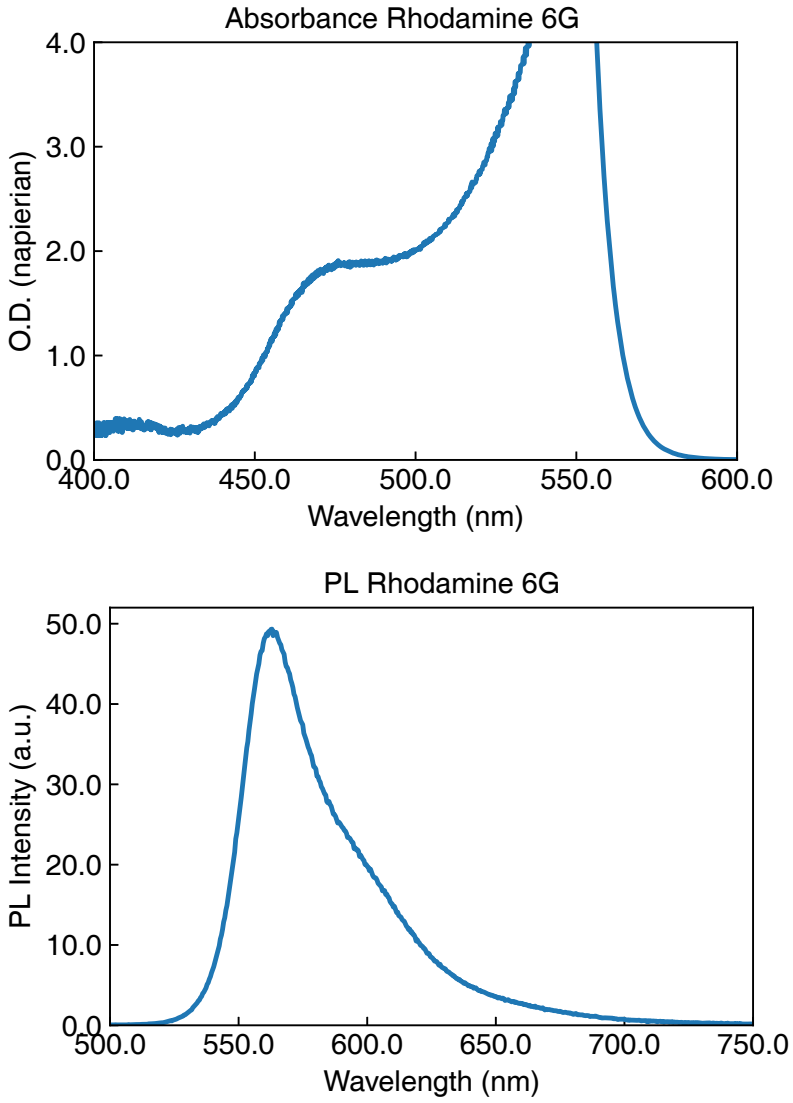


Figure 6.11: Absorbance and PL from 0.8 mM Rhodamine 6G in ethanol used as a reference for PLQE. Top: Absorbance from the solution, measured with FTIR, using a NIR source and a Si detector. Bottom: PL from the Rhodamine 6G solution.

6.5 PL Lifetimes

The PL decays following pulsed photoexcitation were measured by TCSPC (see Section 3.3). The samples were kept under vacuum during the experiment and excited at a fluence of 1 to 4 $\mathrm{nJ\,cm^{-2}}$. Table 6.3 provides an overview of decay lifetimes for the different polymers on quartz obtained from monoexponential fits to the data in the time ranges 0.1 to 3 ns (F8BT and Super Yellow) and 0.1 to 1.5 ns (P3HT and PTAA). Additionally, the absorption coefficient α at the excitation wavelength is listed (see Section 6.6.2 for more explanation). PL decays from films of different thicknesses of Super Yellow, F8BT and P3HT deposited on $MAPbI_3$:quartz and on quartz are shown in Fig 6.13. For PTAA, the the decay traces are shown in Fig. 6.12.

Table 6.3: PL lifetimes, excitation and detection wavelength and absorption coefficient at the excitation wavelength of the different polymers.

	F8BT	**Super Yellow**	**P3HT**	**PTAA**
Lifetime	0.85 ns	1 ns	0.3 ns	0.22 ns
Excitation Wavelength	400 nm	400 nm	460 nm	360 nm
Detection Wavelength	540 nm	600 nm	725 nm	460 nm
Absorption Coefficient	$0.013\,\mathrm{nm^{-1}}$	$0.013\,\mathrm{nm^{-1}}$	$0.008\,\mathrm{nm^{-1}}$	$0.015\,\mathrm{nm^{-1}}$

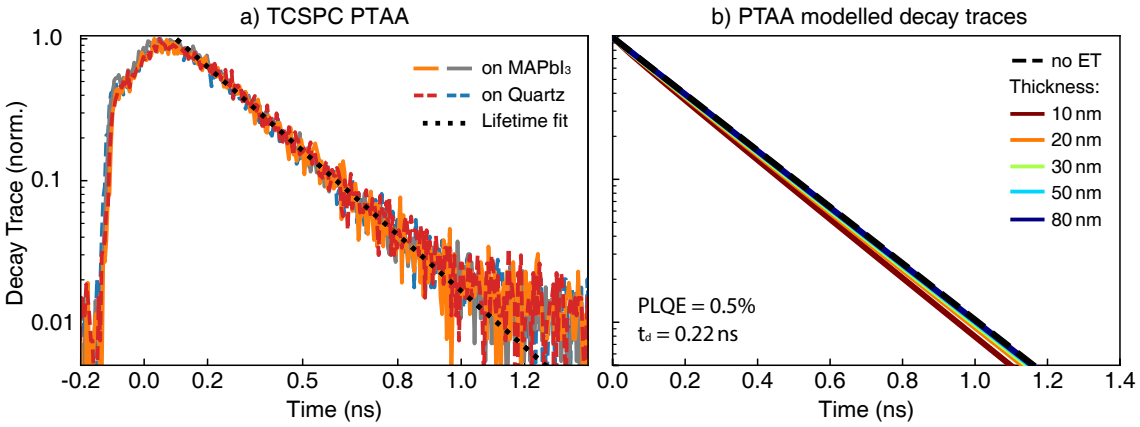


Figure 6.12: a) Normalised TCSPC traces from PTAA films of different thickness on quartz and $MAPbI_3$:quartz substrates, detected at 460 nm. No influence of either thickness or surface underneath the film is seen. The monoexponential fit for the decay lifetime is plotted on top of the data as black dotted curve. b) Modelled decay traces for films on $MAPbI_3$ taking into account ET (ET) from the polymer to the $MAPbI_3$ for polymer layer thicknesses between 10 nm and 80 nm. PLQE and decay lifetime as used in the model are indicated.

6.6 Fluorescence Decay and ET Efficiency Model

Accelerated PL decay is observed for high PLQE polymers (Super Yellow and F8BT) on $MAPbI_3$:quartz compared to their PL decay on quartz (cf. Fig. 6.13). No change in PL decay time was detected for low PLQE polymers on $MAPbI_3$:quartz (cf. Figs. 6.13 and 6.12a). The faster PL decay observed mainly for the thin (20 to 30 nm) layers of luminescent polymers suggests that ET may occur between the polymer and the $MAPbI_3$, as described by FRET.

In the this section, FRET theory is applied to model ET between the polymer and the $MAPbI_3$. In a first step, the application of FRET to a two-layer geometry is outlined. The theory leads to an expression for the PL decay as a function of time, which is fitted to the PL decay traces in a second step. Using the results from the first two steps, the efficiency of ET from an organic semiconductor to $MAPbI_3$ is calculated based on properties of the organic semiconductor layer in a third step.

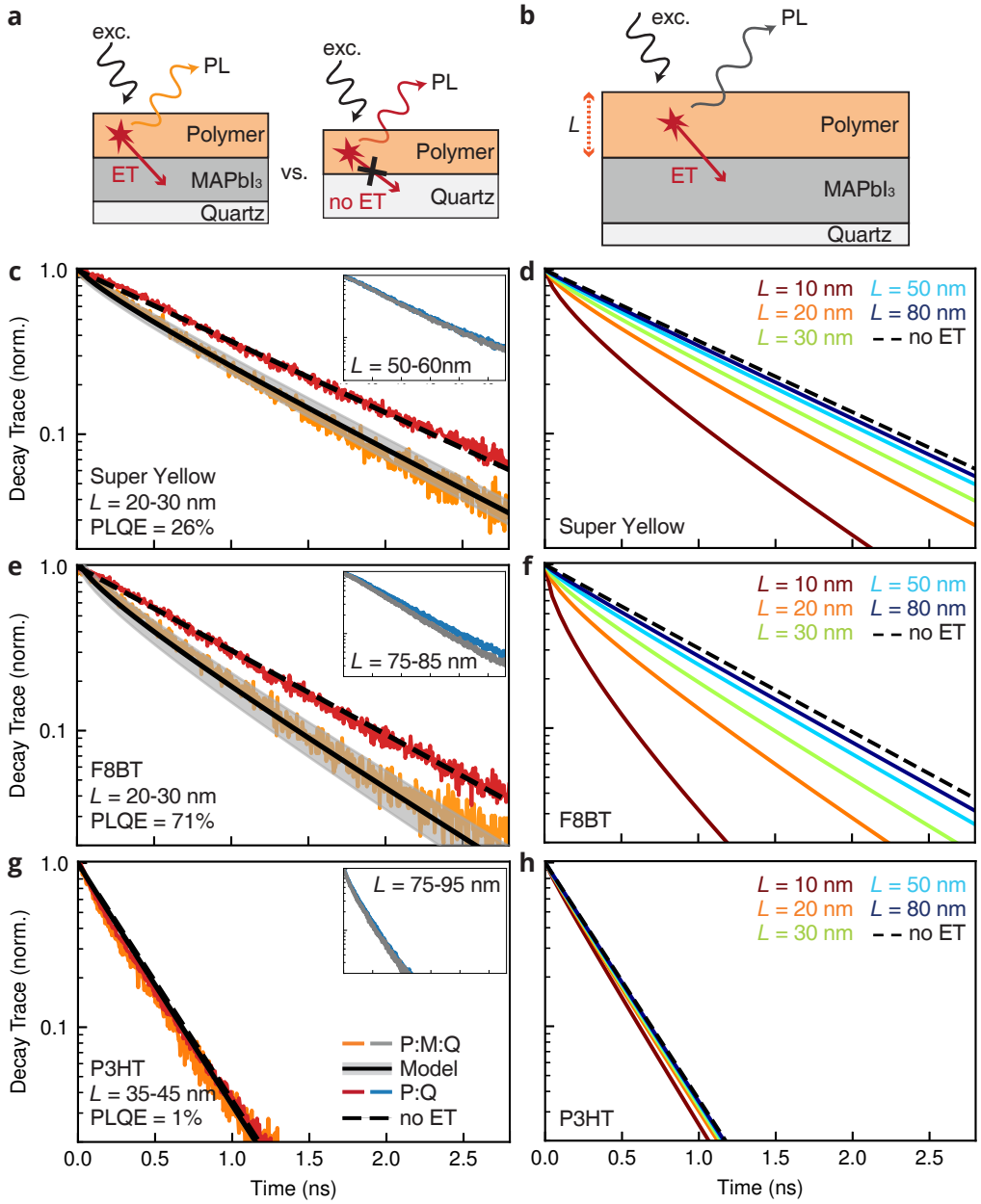


Figure 6.13: Decay traces for the polymers Super Yellow, F8BT and P3HT, as measured on quartz and on $MAPbI_3$:quartz (schematic in a) and modelled with ET on $MAPbI_3$:quartz (schematic in b). c), e) and g) show the measured data of films on $MAPbI_3$:quartz (orange) versus on quartz (red) for thin polymer films (inset: thicker polymer films on $MAPbI_3$:quartz in grey and on quartz in blue). The solid line depicts the modelled decay of the polymer film on $MAPbI_3$:quartz with an estimated error (grey shaded). The dashed line shows a monoexponential fit to the data, representing the PL lifetime of the polymer on quartz with no ET. d), f) and h) depict modelled decay traces for the polymers dependent on film thickness L. Film thickness and PLQE are noted for each case.

6.6.1 FRET in Two-Layer Geometry

FRET from an energy donor to an energy acceptor based on their dipole-dipole interactions can be expressed through the rate of the ET, $k_{da}(r)$ as a function of donor-acceptor distance r, donor lifetime τ_d, and the Förster radius R_0:

$$k_{da}(r) \;=\; \frac{1}{\tau_d}\left(\frac{R_0}{r}\right)^6. \tag{6.2}$$

with:

$$R_0 \;=\; \left(\frac{9\;\ln(10)\;\kappa^2\;\phi_d}{128\;\pi^5\;N_A\;n^4}J\right)^{1/6}, \tag{6.3}$$

where κ^2 accounts for the geometric orientation of the donor and acceptor dipoles, ϕ_d is the PLQE of a purely donor sample, N_A denotes the Avogadro constant, n is the refractive index and J is the overlap integral between donor emission and acceptor absorption [58, 64]. R_0 has units of nm if J is entered in units of $\frac{\mathrm{dm^3nm^4}}{\mathrm{mol\,cm}}$ [70]. R_0 defines the distance at which any other pathway of de-excitation of the donor is as likely as de-excitation via FRET. The orientation factor will be assumed to be $\kappa = 0.845\sqrt{2/3}$ for further discussions, which assumes random but fixed relative orientations of donor and acceptor dipoles within a solid film [170].

To correctly model the ET, the layer geometry has to be taken into account. Förster's original expression for $k_{da}(r)$ as stated above was derived for ET within a solution (3-dimensional space) with uniform donor and acceptor concentrations [59, 71]. A variety of theoretical approaches have since been applied by several authors [95–99] to adapt and extend Förster's theory to consider the effect of varying spatial dimension (see Section 2.3.3). The expression for FRET, which is important in this context, is an extended "KB-equation", which incorporates arbitrary distributions of donors and acceptors. Within this framework, the donor decay $I_d(t)$ as a function of time for ET between donors and acceptors, integrated over their positions $\mathbf{r_d}$ and $\mathbf{r_a}$ within a restricted volume, is given by:

$$I_d(t) \;=\; e^{-t/\tau_d}\int_V C_d(\mathbf{r_d})\;\varphi(t,\mathbf{r_d})\;d\mathbf{r_d} \tag{6.4}$$

with:

$$\varphi(t, \mathbf{r_d}) \;=\; \exp\Big(-\int_V C_a(\mathbf{r_a})\;[1 - e^{-t\;k(|\mathbf{r_a}-\mathbf{r_d})|}]\;d\mathbf{r_a}\Big), \tag{6.5}$$

where $C_d(\mathbf{r_d})$ and $C_a(\mathbf{r_a})$ denote the heterogeneous donor and acceptor concentrations. Yekta et al. [108] applied this formalism to systems with planar geometry and used it to derive analytic expressions for fluorescence decay inter alia for the situation of "parallel slabs of donor and acceptor touching at a sharp interface". Their approach is outlined in the following and in the final step of the derivation, a non-uniform donor concentration $C_d(z)$ is introduced to account for the fact that the number of initially excited donors as a function of film depth z is proportional to a Beer-Lambert profile.

For systems with planar symmetry, the donor and acceptor concentrations, $C_d(z)$ and $C_a(z)$ respectively, vary along a single spatial direction, here denoted as z-axis. For any thin vertical slice of the film, the donor and acceptor concentrations are assumed to be constant and Eqs. 6.4 and 6.5 can be rewritten as:

$$I_d(t) \;=\; e^{-t/\tau_d} \int C_d(z)\;\varphi(z,t)\;dz \tag{6.6}$$

$$\varphi(z,t) \;=\; \exp\Big(-\int_V C_a(z)\;[1 - e^{-t\;k(r)}]\;dV\Big) \tag{6.7}$$

Geometrical considerations lead to the general expression for $I_d(t)$ for systems with planar symmetry:

$$I_d(t) \;=\; e^{-t/\tau_d} \int_{-\infty}^{+\infty} C_d(z)\;\varphi(z,t)\;dz \tag{6.8}$$

$$\varphi(z,t) \;=\; \exp\Big(-h(z,t)\Big) \tag{6.9}$$

$$h(z,t) \;=\; 2\pi \int_0^{\infty} r\;\Big(1 - e^{-t/\tau_d\;(R_0/r)^6}\Big) \int_{z-r}^{z+r} C_a(\hat{z})\;d\hat{z}\;dr. \tag{6.10}$$

The planar system of interest here consists of two extended layers touching at an interface. One layer consists of an organic semiconductor donating energy to the $MAPbI_3$ acceptors in the second layer. In order to arrive at a numerical expression for

this situation, the interface is positioned at $z = 0$, the donor layer extends from $z = 0$ to L and the extended acceptor layer spans from $z = 0$ to $-\infty$. The assumption of an infinite acceptor layer is well justified as most of the ET happens within a few R_0, which is much smaller than the thickness of the $MAPbI_3$ layers considered here. The concentration of donors and acceptors within each respective extended layer can be assumed to be uniform: C_d and C_a. However, the number of initially excited donors will be assumed to follow a Beer-Lambert profile and is therefore not uniform. From these assumptions and geometrical definitions the concentrations can be written as:

$$C_d(z) \;=\; C_d \; e^{-\alpha \; (L-z)} \tag{6.11}$$

$$C_a(z) \;=\; C_a \; H(-z) \tag{6.12}$$

where α is the absorption coefficient of the polymer at the excitation wavelength used for the donor decay measurements and $H(x)$ denotes the Heaviside function (0 for $x < 0$ and 1 for $x \geq 0$). Using these definitions, the donor decay can be written as:

$$I_d(t) \;=\; e^{-t/\tau_d} \; C_d \int_0^L e^{-\alpha \; (L-z)} \; \varphi(z,t) \; dz \tag{6.13}$$

$$\varphi(z,t) \;=\; \exp\!\left(-\frac{\pi}{3} \; C_a \; R_0^3 \left(\frac{t}{\tau_d}\right)^{\frac{1}{2}} \left[T^{-\frac{1}{2}}(1-e^{-T}) + 2\gamma(\tfrac{1}{2},T) - 3T^{-\frac{1}{6}} \; \gamma(\tfrac{2}{3},T)\right]\right) \tag{6.14}$$

where the substitution

$$T \;=\; \frac{t}{\tau_d} \left(\frac{R_0}{z}\right)^6 \tag{6.15}$$

has been made and $\gamma(n,T)$ is the incomplete gamma function, defined as:

$$\gamma(n,T) \;=\; \int_0^T \; u^{n-1} \; e^{-u} \; du. \tag{6.16}$$

6.6.2 PL Decay Modelling

Equations 6.13 to 6.16 enable modelling of the PL decay data from the polymers on $MAPbI_3$:quartz. The modelling was performed in two steps: First, the expression for $I_d(t)$ in Eq. 6.13 is employed and R_0 is used as a fitting parameter to fit the data from SuperYellow:$MAPbI_3$:quartz. The global parameter C_a is determined through R_0 and is also obtained in this step. In a second step, it is assumed that the difference in R_0 between the polymers is a function of PLQE only (as discussed below) and the measured PLQE values from the polymers are used to obtain $I_d(t)$ through Eq. 6.13 for F8BT, P3HT and PTAA. A schematic overview of the modelling approach is depicted in Fig. 6.14.

The parameters for calculating $I_d(t)$ are: the donor lifetime τ_d, donor (polymer) and acceptor ($MAPbI_3$) concentration C_d and C_a, polymer film thickness L, Förster radius R_0 and absorption coefficient of the polymer α. These parameters will be discussed and their determination analysed in the following:

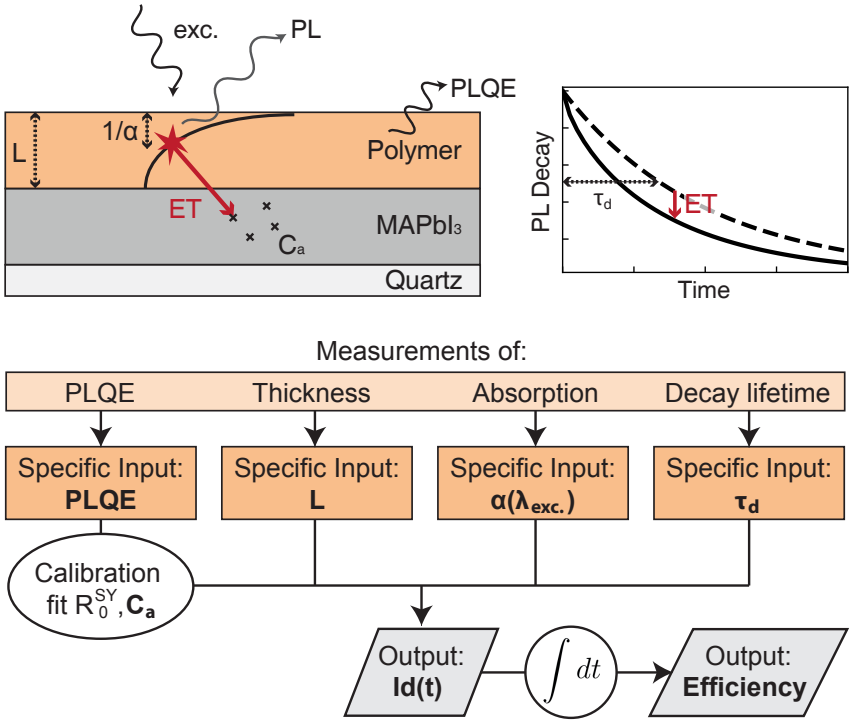


Figure 6.14: Schematic representation of modelling PL decay traces and ET efficiency.

Donor lifetime, τ_d: The donor lifetime in absence of any acceptors was obtained from polymer films on a quartz substrate. A monoexponential lifetime decay was fitted to the TCSPC data over the following time ranges: 0.1 to 3 ns (F8BT and Super Yellow), 0.1 to 1.5 ns (P3HT) and t_0 was set to the peak of the rise of the TCSPC data. The fits are indicated as dashed lines in Fig. 6.13 and the obtained lifetimes for the different polymers are listed in Table 6.3.

Film thickness, L: Film thickness of the polymer film on $MAPbI_3$ was obtained from DEKTAK measurements and is used as a specific input parameter. The values for the polymer films are given in Table 6.1.

Donor concentration C_d: The donor concentration in units of a number density is assumed to be uniform within the polymer film and is used as a scaling factor only. C_d scales the overall PL intensity in Eq. 6.13. The fitting is performed with normalised PL decay traces, which are not determined in absolute terms. Therefore, no specific value is assigned to C_d. However, the concentration of *excited* donors as a function of film penetration depth, $C_d(z)$ is assumed to follow Beer's law (see Eq. 6.11) and was incorporated into the expression for $I_d(t)$ in Eq. 6.13.

Absorption coefficient, α: The absorption coefficient was obtained from absorption data (see Section 6.3) at the excitation wavelength for the PL decay measurements (see Table 6.3) and from the polymer film thickness (see Table 6.1). It is a fixed input parameter to the model, specific to each polymer. The values are listed in Table 6.3 in units of nm^{-1} as entered in $I_d(t)$. The unit nm^{-1} is used for consistency as the film thickness L and the film penetration depth z are entered in nm in Eq. 6.13.

Acceptor concentration, C_a: Here, the acceptor concentration refers to accepting sites within the $MAPbI_3$ layer, which is an abstract definition and should not to be confused with single cells of $MAPbI_3$ or specific atoms within the $MAPbI_3$. C_a will be

obtained through and fitting the transient data. The acceptor concentration can be expressed a function of the refractive index n, PLQE ϕ_d, the spectral overlap J and the Förster Radius R_0. These physical quantities therefore become input parameters for modelling the PL decay data and will be further discussed. Beforehand, an equation to express C_a in terms of these quantities will be derived. C_a has units of nm^{-3} as R_0 is entered in units of nm in Eq. 6.14. The Förster radius is defined in Eq. 6.3 and can be rewritten in terms of units as [33, 64, 70]:

$$\frac{R_0}{\mathrm{nm}} \;=\; 0.02108 \left(\frac{\kappa^2 \; \phi_d}{n^4} \left[\frac{J}{\mathrm{mol}^{-1}\mathrm{dm}^3\mathrm{cm}^{-1}\mathrm{nm}^4} \right] \right)^{1/6}, \tag{6.17}$$

with the overlap integral J as a function of wavelength λ in nm. J is given as:

$$J \;=\; \int I_d(\lambda)\epsilon_a(\lambda)\lambda^4 \; d\lambda, \tag{6.18}$$

where $I_d(\lambda)$ is the normalised donor emission and $\epsilon_a(\lambda)$ is the acceptor extinction coefficient.

$$\epsilon_a(\lambda) \;=\; \frac{\log_{10}(e)}{C_{a,molar}} \; \alpha_a(\lambda), \tag{6.19}$$

where $\alpha_a(\lambda)$ is the absorption coefficient as a function of wavelength in units of cm^{-1} and

$$C_{a,molar} \;=\; \frac{\hat{C}_a}{N_A} \tag{6.20}$$

is the molar acceptor concentration in units of $\mathrm{mol/dm}^3$ and $\hat{C}_a$ denotes the acceptor concentration in units of dm^{-3}. For C_a in units of nm^{-3}, it follows:

$$C_a \;=\; N_A \; C_{a,molar} \; 10^{-24} \;=\; 0.6022 \; C_{a,molar}. \tag{6.21}$$

In addition to the overlap integral J, the Förster radius R_0 in Eq 6.17 is determined by the refractive index n, the orientation factor κ and PLQE ϕ_d. The orientation factor κ is fixed for all samples (see above) and the constant $k \;=\; \kappa^2/n^4$ is introduced. Using these definitions, Eq. 6.17 rewrites as:

$$R_0^6 \;=\; k \; \phi_d \; J \;=\; k \; \phi_d \; \frac{1}{C_{a,molar}} \; \hat{J} \tag{6.22}$$

with

$$\hat{J} \;=\; C_{a,molar}\; J \;=\; \log_{10}(e) \int I_d(\lambda)\alpha_a(\lambda)\lambda^4 \; d\lambda. \tag{6.23}$$

Using the above, the derivation arrives at an expression for C_a as a function of R_0, ϕ_d, $\hat{J}$ and k:

$$C_a \;=\; 0.6022 \; \frac{k \; \phi_d \; \hat{J}}{R_0^6}. \tag{6.24}$$

Equation 6.24 expresses the acceptor concentration C_a as a function of the refractive index n (through k), PLQE ϕ_d, the modified overlap $\hat{J}$ and the Förster Radius R_0. These physical quantities become additional input parameters for modelling the PL decay data and will be discussed in the following:

Refractive index, n: In original FRET theory, the refractive index refers to the solution in which donors and acceptors were dissolved [58, 64], which no longer applies for the case of a two-solid-layers system. For films of π-conjugated polymers, an effective refractive index of $n_{poly} = 1.6$ can be assumed [173–175] and $MAPbI_3$ has a refractive index of $n_{MAPbI_3} = 2.5$ at the wavelengths at which the polymers emit [203]. The average value from the polymer and the $MAPbI_3$ of $n = 2.05$ in was used in the calculations assuming that the refractive indexes of both media play a role for the ET process.

Modified spectral overlap, $\hat{J}$: : The modified spectral overlap between donor emission and acceptor absorption is defined through Eq. 6.23. $\hat{J}$ was calculated from $MAPbI_3$ absorption and polymer emission data (see Section 6.3). $\hat{J} = 3.4 \times 10^{14}\,\mathrm{nm}^3$ was calculated for Super Yellow and entered in the calculation of C_a (as in Eq. 6.24) when fitting the PL decay data from SuperYellow:$MAPbI_3$:quartz.

Förster radius, R_0: R_0 is defined in Equations 6.3 and 6.17. As mentioned above, modelling the PL decay of the polymers was done in two steps: In a first step, R_0 was used as a fitting parameter in Eqs. 6.13 to 6.16 to fit the PL decay data from SuperYellow:$MAPbI_3$:quartz to obtain R_0^{SY} and through Eq. 6.24 also the global input parameter C_a. In a second step, $I_d(t)$ of the other polymers is modelled using Eqs. 6.13 to 6.16 with $C_a = 0.0016\,\mathrm{nm}^{-3}$ and $R_0^{SY} = 8.5 \pm 0.6$ as global input parameters and

$$R_0^{polymer} = R_0^{SY} \left(\frac{\phi_{polymer}}{\phi_{SY}} \right)^{1/6} \tag{6.25}$$

as a polymer specific input parameter. Here, it is assumed that the polymer PLQE is the most sensitive parameter in determining R_0 between the different polymers to describe the ET from the polymer layer to the $MAPbI_3$ layer. R_0 (see Eq. 6.17) is determined by the orientation factor κ, PLQE ϕ_d, the refractive index n and the spectral overlap J. κ is a fixed parameter and n is assumed to be the same for the investigated polymers. The other parameter next to ϕ_d which might change between the polymers is the overlap integral J (see Eq. 6.18) or, alternatively, $\hat{J}$, as defined in Eq. 6.23. The spectral overlap is determined from normalised donor emission and acceptor absorption. All polymers were deposited on $MAPbI_3$, which acts as the acceptor. Therefore, the acceptor absorption represented through the extinction coefficient in J or the absorption coefficient in $\hat{J}$ in the overlap integral remains unchanged in any case. Additionally, there is (almost) full overlap between polymer emission and $MAPbI_3$ absorption for all investigated polymers. Differences in the overlap integral would therefore only stem from the wavelength-dependence of the normalised donor emission. The assumption of determining $R_0^{polymer}$ through change in PLQE only is accordingly supported by the computed values of $\hat{J}$ for Super Yellow, F8BT and P3HT: $\frac{\hat{J}}{10^{14}\ \mathrm{nm}^3} = 3.4$ (Super Yellow), 3.3 (F8BT) and 3.0 (P3HT, which has slightly less overlap). The PLQE values for these polymers range from 1% to 71%, which is clearly a much greater difference.

The resulting modelled decay traces are depicted together with the experimentally measured PL decay in Fig. 6.13 and will be discussed in Section 6.7. The Förster radii which were calculated for the polymers are noted in Table 6.4. The error on the Förster radius and on the modelled PL decay data was determined from uncertainties in the measured input parameters ϕ_d (see Table 6.2) and L (10%). The error on R_0^{SY} was estimated from fitting the PL decay data with the upper and lower boundaries for ϕ_{SY} and L_{SY}. The error in the modelled PL decay data from the other polymers was then estimated from the resulting R_0^{SY}, polymer PLQE and polymer thickness. The error estimations are depicted as shaded area around the modelled PL traces in Fig. 6.13.

6.6.3 Calculation of ET Efficiency

ET efficiencies are calculated from modelled PL decay of a material in absence and in presence of $MAPbI_3$. The PL decay of the polymers in absence of an energy acceptor is expected to follow a monoexponential decay $\exp(-t/\tau_d)$ with the PL lifetime τ_d as fitted in Section 6.3. The PL decay of a polymer in the presence of $MAPbI_3$ as an acceptor can be modelled using Eqs. 6.13 to 6.16 as $I_d(t)$. In both cases, the integrated area of the PL decay represents the number of decay events at the detection wavelength minus potential ET events. The difference in the integrated area from the appropriately scaled monoexponential PL decay and from integration of Eq. 6.13 is a measure for the ET efficiency η_{ET}, which is therefore calculated as:

$$\eta_{ET} = \frac{F_{sc} \int \exp(-t/t_d)\, dt - \int I_d(t)\, dt}{F_{sc} \int \exp(-t/t_d)\, dt}. \tag{6.26}$$

F_{sc} is a scaling factor introduced to scale the monoexponential PL decay to the scaling of $I_d(t)$ in Eq. 6.13: $F_{sc} = I_d(t_0)$. For the modelling of the transfer efficiency, t_0 is set to 1×10^{-6} ns as zero can not be used for practical calculation in the integral of Eq. 6.13. Using a lower value for t_0 does not change the value of the efficiency in any case. The transfer efficiency takes values between 0 and 1. In terms of

practical calculation, the integration is performed as a definitive integral using the python package scipy.integrate [204] and the boundaries were set to $t = 0.000\,001$ to 100 ns. Convergence of the integral was thoroughly tested with a wide range of input parameters covering the whole range of parameter values that were used for the figures.

The calculation of ET efficiency is based on measurable CTL (charge transfer layer) material properties that influence the ET mechanism. Measured PL decay data from model polymers was used to calibrate the modelling. The resulting ET efficiency model is however applicable not only to the polymers that are investigated but more generally to layers of organic semiconductors deposited on $MAPbI_3$.

Eq. 6.26 in combination with Eqs. 6.13 -6.16 enables to model ET efficiency between an organic semiconductor layer and $MAPbI_3$ layer. Global input parameters employed to calibrate the model are $R_0^{SY} = 8.5 \pm 0.6$ nm and $C_a = 0.0016\,\mathrm{nm}^{-3}$, which were determined in the first step of the PL decay modelling. Input parameters specific to the organic semiconductor are its film thickness L, PL lifetime τ_d, PLQE ϕ_d and the absorption coefficient $\alpha(\lambda_{exc.})$ at the wavelength of excitation. The results for the calculated η_{ET} for experimentally investigated polymers are listed in Table 6.4.

Modelled ET efficiency between a photoexcited organic semiconductor layer and a $MAPbI_3$ layer are depicted in Fig. 6.15 as a function of CTL film thickness, and PLQE and in Fig 6.16 as a function of absorption coefficient at the excitation wavelength and PLQE.

Table 6.4: Thickness, Förster radius and ET efficiency of polymer films on $MAPbI_3$:quartz for Super Yellow, F8BT and P3HT.

	Film Thickness (nm)	**Förster Radius** (nm)	**ET Eff.** (%)
Super Yellow	23	8.5 ± 0.6	28
F8BT	25	10 ± 0.9	38
P3HT	40	4.9 ± 0.7	3
PTAA	35	4.4 ± 0.5	2

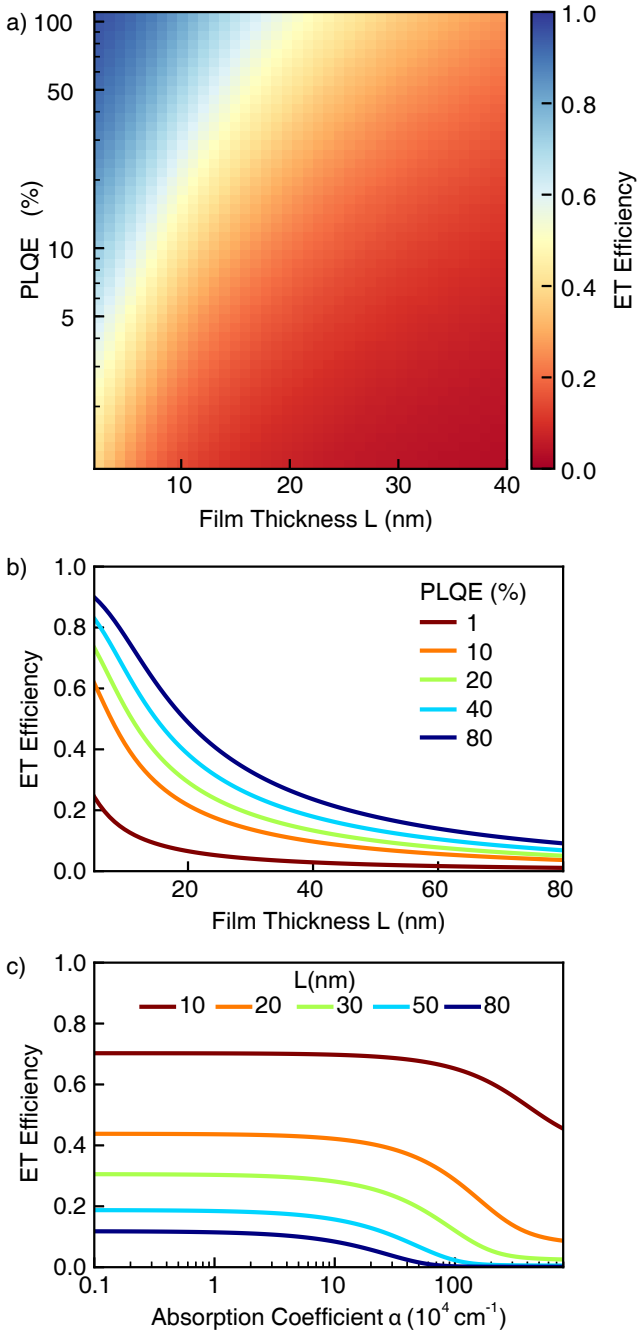


Figure 6.15: a) Efficiency of the ET between a photoexcited organic semiconductor layer and a $MAPbI_3$ layer underneath as a function of organic semiconductor film thickness L and PLQE. b) ET efficiency as a function of organic semiconductor film thickness for distinct PLQE values with $\alpha = 13 \times 10^4\,\mathrm{cm}^{-1}$. c) ET efficiency as a function of the CTL absorption coefficient $\alpha(\lambda_{exc})$ at the excitation wavelength, for different film thicknesses and a value of 50% PLQE.

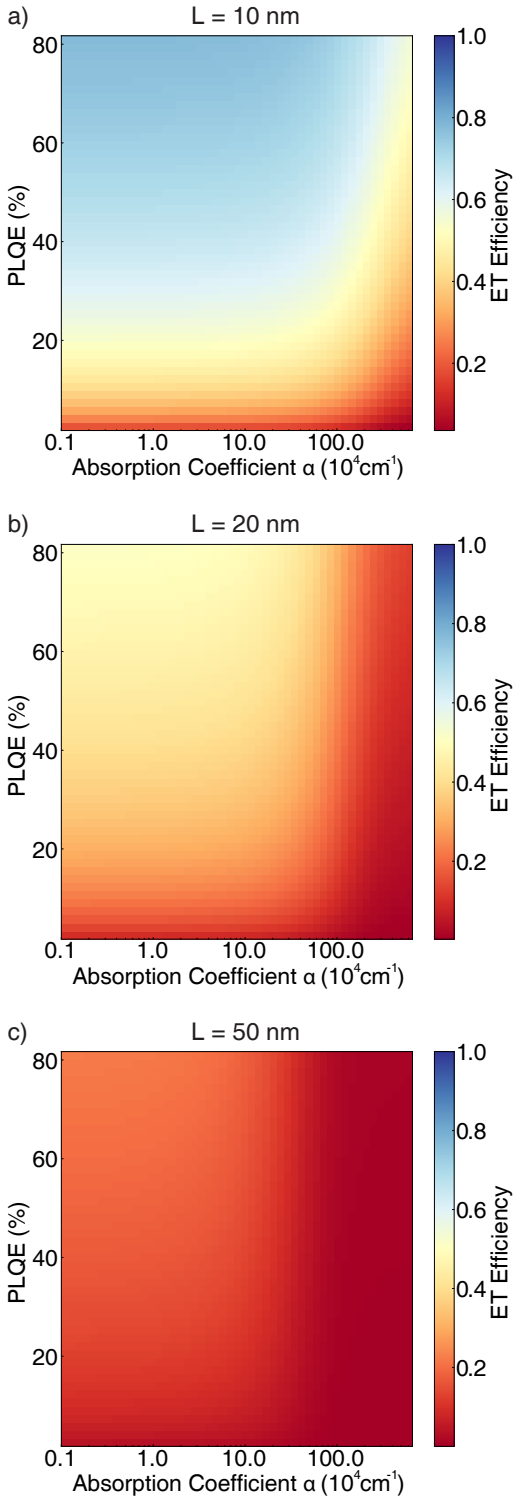


Figure 6.16: Transfer efficiency as a function of absorption coefficient α and PLQE for films of a) 10 nm b) 20 nm c) 50 nm thickness.

6.7 Discussion

This section discusses experimental observations and modelling of ET between a photoexcited polymer layer and the underlying $MAPbI_3$. The focus lies on how much of the energy from incoming light which is undesirably absorbed by an organic semiconductor is transferred to the $MAPbI_3$ underneath and on determining the properties of CTLs that lead to efficient ET from the photoexcited CTL to the MHP, which could counteract parasitic light absorption. The discussion is structured in three sections: First the observation of ET between photoexcited polymer layers and a $MAPbI_3$ layer is examined. Second, the results from modelling the PL decay traces are considered. Third, the findings from modelling the ET efficiency based on CTL properties and their influence on choosing CTL materials are discussed.

Reduced overall PL emission intensity was observed for the highly emissive polymers Super Yellow and F8BT in polymer:$MAPbI_3$:quartz samples that yield a polymer layer thickness of the order of 25 nm as opposed to samples with a polymer layer thickness greater than 50 nm or weakly emitting polymer samples (cf. Figs. 6.2-6.8). Reduced PL intensity is a sign of ET [58, 64] and therefore a first indication that energy is transferred from the photoexcited polymer to $MAPbI_3$ for thin and high PLQE films. Intuitively, ET would be expected to be more prominent for thinner films: Upon light illumination, an excitation is created in the polymer layer at a penetration depth that depends on the polymer absorption coefficient [33]. For thinner films, it is thus more likely that the initial excitation is created closer to the interface with the energy accepting $MAPbI_3$ than for thicker films. Therefore, since ET is highly sensitive to the distance between an energy donor (polymer) and an energy acceptor ($MAPbI_3$), energy is more likely to be transferred if donor and acceptor are in closer vicinity [30] as it is the case for thinner polymer layers.

Features of ET can also be assessed by examining PL decay dynamics: The left column of Fig. 6.13 depicts measured PL decay traces from polymer:quartz and polymer:$MAPbI_3$:quartz for different polymer layer thicknesses. The PL decay traces were recorded at polymer-specific wavelengths at which predominantly the polymer emits (cf. Table 6.3 and figures in Section 6.3). The measured PL decay of the thin (∼25 nm) and high PLQE polymers Super Yellow and F8BT exhibits a faster PL decay when deposited on top of $MAPbI_3$:quartz than on quartz. This implies an additional decay channel for excitations in these samples, which is not observed for thicker (> 50 nm) polymer layers and for the weakly emitting P3HT and PTAA. Faster PL decay for an energy donor material in the presence of an energy acceptor is a hallmark of resonant ET [64, 114, 205, 206]. Photoexcitation of the polymer layer will generate relatively tightly bound excitons in the material [46], whose dipole moments are associated with oscillating electric fields that will couple to electronic transitions in the perovskite. Such dipole-dipole resonant coupling may lead to transfer of the originally generated exciton from the energy donor (the polymer) to the acceptor ($MAPbI_3$) without the need for photon emission, provided that the donor emission and acceptor absorption spectrally overlap. It is noteworthy, that such an ET process that couples to states high above the band edge of $MAPbI_3$ will most likely result in the generation of free electron-hole pairs, rather than tightly bound excitons, given the low (15 meV) [207] exciton binding energy for $MAPbI_3$.

In addition, this ET mechanism is indeed intuitively expected to be more prominent for thinner polymer films and higher PLQE values, as observed here. For thinner films, a larger fraction of the photoexcited excitons are created in the polymer film within close proximity to the polymer:$MAPbI_3$ interface. Given that the ET mechanism only has a certain range over which it is effective (quantified by the Förster radius [30], discussed in more detail below), thinner polymer films therefore result in a higher likelihood of excitons being transferred to $MAPbI_3$. This situation is further exacerbated when polymer layers are highly absorbing, since illumination

creates an exponentially decaying excitation profile within the film (see schematic in Figure 6.14), whose penetration depth depends inversely on the polymer absorption coefficient [33]. For high absorption coefficients at a given excitation wavelengths, excitons are thus generated close to the surface of the polymer film, far from the polymer:$MAPbI_3$ interface, if films are thick. In addition, the observed strong dependence of the ET process on the PLQE of the polymer clearly supports the presence of ET, given that a lower PLQE may reflect a reduced oscillator strength of the excitonic downward transition in the polymer, which will lower the coupling strength to electronic transitions in $MAPbI_3$. As discussed in more detail in Chapter 7, P3HT has a strong tendency for H-aggregate formation, which suppresses its PLQE and oscillator strength for downward transitions, explaining why even for thin polymer films on $MAPbI_3$ little ET occurs (see Figure 6.13g). The measurements of PL spectra and PL decay dynamics therefore clearly indicate that energy is transferred between the photoexcited polymer layer and the adjacent $MAPbI_3$ layer.

Excellent agreement was found between the measured and modelled PL decay traces, which confirms the presented methodological approach. The results from modelling the PL decay traces for polymer:$MAPbI_3$:quartz samples are shown in Fig. 6.13. In the right column, the modelled decay curves (black solid lines) are depicted together with the measured PL decay (orange lines) with errors (grey shaded areas) deduced from measurement uncertainties. The PL decay was fitted for Super Yellow and based thereupon, the PL decay traces of F8BT, P3HT and PTAA samples were modelled. The left column of Fig. 6.13 shows modelled PL decay dynamics for different polymer layer thicknesses L. As intuitively expected, PL intensity decays faster for thinner polymer films on $MAPbI_3$:quartz because the excitations in these polymer films are created closer to the $MAPbI_3$ interface such that more energy can be transferred from the polymer to the $MAPbI_3$. The effect of faster PL decay is strongest for F8BT which has the highest PLQE and weakest for the low PLQE

polymers P3HT and PTAA. A high polymer PLQE ϕ_d enlarges the Förster radius R_0 (cf. Eq. 6.3) which is a measure for the distance at which ET is likely to occur. Therefore, the higher the PLQE, the larger the distance from the initial excitation in the polymer for which ET to the $MAPbI_3$ is expected.

The Förster radius is a distance measure for ET and thus provides a first benchmark on CTL thickness to achieve efficient ET. R_0 for ET between the polymer and $MAPbI_3$ is calculated for each polymer in the modelling process and is listed in Table 6.4. The fitted Förster radius for Super Yellow as the energy donor and $MAPbI_3$ as the energy acceptor is $R_0^{SY} = 8.5 \pm 0.6$ nm. A large Förster radius is expected as polymer emission and $MAPbI_3$ absorption fully overlap (cf. Fig. 6.4 and 6.9), thereby fulfilling the resonance condition for FRET over a wide range of wavelengths [30]. Additionally, exciton diffusion within the donor material prior to the ET event has been observed to enhance the Förster radius deduced from PL decay dynamics [114, 177, 178], which could also be the case here as R_0 was deduced from PL decay data.

The resulting modelled ET efficiency as a function of CTL film thickness, PLQE and absorption coefficient at the excitation wavelength are shown in Figs. 6.15 and 6.16. There are three key trends that indicate how efficient ET from an organic semiconductor to the $MAPbI_3$ can be achieved in order to avoid losses, which are crucial for choosing the front carrier-extraction layers in MHP-based solar cells: i) The higher the CTL PLQE, the more efficient the ET. ii) Thin ($\leq$ 10 nm) CTLs are beneficial for efficient ET. iii) A high ($\gg 1 \times 10^5\,\mathrm{cm}^{-1}$) absorption coefficient of the organic semiconductor at the wavelength of the absorbed light impedes ET. The underlying reasons for these observations relate to both the nature of resonant ET and the dual-layer geometry. As elucidated previously, high PLQE leads to stronger dipole-dipole coupling between downward transitions in the photoexcited CTL and upwards transitions responsible for absorption in $MAPbI_3$. CTLs whose thickness is comparable with the Förster radius R_0 that captures the range over which dipole-dipole interactions are effective,

will also show enhanced chance of ET events. A high absorption coefficient $\alpha(\lambda_{exc})$ at the excitation wavelength, on the other hand, is detrimental, because it results in a short penetration depth of incoming light, with more photoexcitations being created in the CTL closer to its front surface and therefore further away from the $MAPbI_3$ layer, reducing ET efficiency. Such uneven excitation profiles will become prominent when $\alpha(\lambda_{exc}) \gg L^{-1}$, which, for CTL layer thicknesses of a few tens of nanometers, means a threshold condition of $\alpha(\lambda_{exc}) \sim 1 \times 10^5\,\mathrm{cm}^{-1}$ above which ET efficiency deteriorates, as shown in Figs. 6.15c) and 6.16. For smaller values of $\alpha(\lambda_{exc})$ the penetration depth is longer than the layer thickness L and more excitations are likely to be created within the capture radius of the $MAPbI_3$ acceptor layer. Commonly employed CTL materials are likely to meet this criterion as they are generally chosen to have minimized absorption of sun light [208]. It was further found that the PL lifetime τ_d does not substantially influence the ET efficiency, within the wide range of lifetimes (0.1 to 1000 ns) and PLQE (0.1 to 80 %.) used in the modelling.

Taken together, it is the combination of CTL thickness, PLQE and absorption coefficient which is decisive for determining the attainable efficiency of ET. In particular, stronger parasitic light absorption coefficients may still be tolerated for CTLs, if these layers are thin and exhibit high PLQE. This finding is important, given that exploration of sun-facing front CTL materials so far has concentrated exclusively on materials that are transparent (i.e. absorb as little as possible across the sun spectrum) to avoid parasitic absorption in the CTL [208]. The findings above suggest that less transparent materials with high PLQE may be equally tolerable as CTL materials for MHP-based solar cells because absorbed energy is efficiently transferred to the MHP. This approach opens up a larger material space suitable for CTLs, allowing selection of previously unexplored candidates that share further positive characteristics, such as higher charge-carrier mobilities or more optimized energy level alignment, which can reduce charge-extraction losses. Regardless of the specific selection, any efficient ET process between the front facing CTL and the active MHP

layer will enhance device performance, as it mitigates parasitic light absorption by transferring excitations to the MHP, from where they can be harvested as photocurrent.

6.8 Summary and Conclusion

The potential of efficient energy transfer between a photoexcited organic semiconductor layer and a metal halide perovskite layer has been assessed for the first time. Parasitic absorption of light in sun-facing front charge-extraction layers in metal halide perovskite-based solar cells does not necessarily lead to unwanted losses. Significant energy transfer to the metal halide perovskite can enhance the photocurrent of the device, allowing metal halide perovskite-based solar cells to reach their limits.

Excitation energy transfer from a photoexcited polymer layer to $MAPbI_3$ was experimentally observed. The measured PL decay from the polymers was successfully modelled and efficiency of the energy transfer was calculated.

Discerning the material properties of a molecular charge transfer layer that lead to efficient energy transfer is key as it may reduce losses in MHP-based solar cells and thus improve device performance. By modelling the energy transfer efficiency based on experimentally observed PL decays from layers of photoexcited polymers on $MAPbI_3$, it was found that in order to achieve efficient energy transfer, very thin ($\leq 10\,\mathrm{nm}$) layers and/or high PLQE materials should be considered. The findings also highlight that is not necessary for the organic semiconductor to be fully transparent at the wavelengths of absorption of the metal halide perovskite if the material exhibits high PLQE, which considerably widens the field of possible candidates for charge-extraction layers.

7

Aggregation in P3HT Films on a Metal Halide Perovskite Layer

Contents

7.1 Background and Motivation 133
7.2 Sample Preparation 135
7.3 Absorption 135
7.4 Photoluminescence 136
7.5 Discussion 140
7.6 Summary and Conclusion 145

Reproduced in part from work submitted for publication by Eggimann et al. in Ref. [182].

7.1 Background and Motivation

In this chapter, thin film structures of the hole-transport material poly(3-hexylthiophene) (P3HT) are investigated. P3HT is a widely researched polymer of which the chemical structure is shown in Fig. 7.1. Centered around a report by Brown et al. [153] on the relative weakness and temperature behaviour of the lowest energy feature in P3HT absorption spectra, the origin of the spectral features of P3HT have been subject of much debate and investigation [49, 153, 209–214]. A widely used interpretation for the data is the model of weakly coupled H-aggregates forming because of interchain interaction between the chromophores in polymer films, which was introduced and applied by Spano and co-workers [213, 214]. For ideal H-aggregates the transition to the ground state is dipole-forbidden and there is no 0-0 peak in the emission, but disorder can lead to an increase of relative intensity of the 0-0 peak to the 0-1 peak in emission and absorption [52, 213]. More recently, the model for aggregate formation was extended to so called "HJ-aggregates" taking into account competition between interchain and intrachain interactions and therefore between the formation of H- and J-aggregates, respectively [49, 56]. Here, intrachain interaction characterises electronic excitations that are delocalised along the polymer chains (through bond) whereas interchain interaction relates to the electronic excitations delocalised between chains (through space) [48]. Sample morphology is thereby assumed to play a decisive role and for thin films in which interchain coupling is dominant, the weakly coupled H-aggregate model offers a prevalent framework for data interpretation [48, 49].

Diffusion of excitations is a critical mechanism for the efficiency of light-to-energy conversion in organic photovoltaic devices. Once an exciton is created by the incoming light, an electron and a hole need to be dissociated and transported to

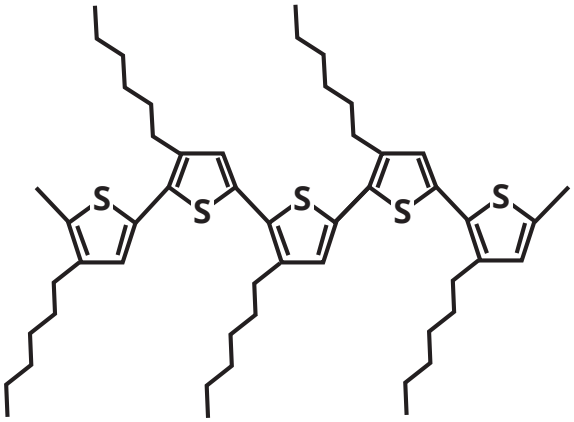


Figure 7.1: Chemical structure of Poly(3-hexylthiophene-2-5-diyl) $(C_{10}H_{14}S)_n$.

electrodes effectively. In conjugated polymers, charge-carrier transport occurs either between neighboring polymer chains with overlapping π-orbitals (interchain) or along the polymer backbone (intrachain). Both transport pathways are sensitive to the arrangement of the polymer chains, which differs between polymer in solution and in thin films [215] and is strongly influenced by film morphology [49, 216–219]. A good understanding of the polymer structures within the transport layer and the role of the interface to other layers is therefore critical for the development of efficiently working devices.

To gain better understanding of the morphology of the hole-transport material P3HT and its interface with a metal halide perovskite, emission and absorption spectra of P3HT films with varying thickness deposited on $MAPbI_3$ layers are examined and compared to spectra from P3HT films deposited on quartz. The variation in thickness was achieved by a change in spin speed during fabrication. P3HT films deposited on a metal halide perovskite are of great interest as it is a structure used in perovskite-based solar cells [189, 220, 221]. The following question is addressed: ***How does variation in film thickness and spin speed during sample preparation influence film morphology of P3HT films on $MAPbI_3$?***

7.2 Sample Preparation

The general fabrication process of preparing polymer thin films on z-cut quartz substrates directly and on a thin (65 nm) $MAPbI_3$ layer on z-cut quartz substrates ($MAPbI_3$:quartz) as well as the fabrication of the $MAPbI_3$ layer by thermal evaporation has been described in Section 6.2. For the considered P3HT films, a solution was prepared containing P3HT (Poly(3-hexylthiophene-2-5-diyl), purchased from Sigma Aldrich (CAS number 104934-50-1), dissolved in anhydrous toluene at a concentration of 15 mg mL^{-1}. The solution was then deposited on the quartz directly, or on the $MAPbI_3$ layer on quartz by dynamic spin coating with 2000, 3000, 4000, 5000 and 6000 rpm, to vary the thickness (see Table 7.1) of the P3HT layers. Additionally, two control samples with different P3HT thickness were prepared on a 260 nm $MAPbI_3$ film, showing the same photo-physical behaviour than the films on the thinner (65 nm) $MAPbI_3$ layer on quartz.

7.3 Absorption

The reason for depositing the P3HT films on such a thin $MAPbI_3$ layer was to enable extraction of the P3HT absorption from P3HT:$MAPbI_3$:quartz samples by subtracting the absorption from a $MAPbI_3$-only layer from the total absorption of these samples. This approach allows for investigation of film morphology and aggregation for P3HT films deposited on a $MAPbI_3$ layer.

Table 7.1: Thickness of the P3HT films deposited on quartz and on $MAPbI_3$:quartz with varying spin speed.

	2000 rpm	3000 rpm	4000 rpm	5000 rpm	6000 rpm
P3HT : quartz	77 nm	62 nm	52 nm	46 nm	42 nm
P3HT : $MAPbI_3$: quartz	92 nm	70 nm	55 nm	48 nm	40 nm

Absorption was measured employing the FTIR technique, which is described in Section 3.4 and the source/detector combination that was used is indicated for each case in the figure caption. The absorption of the P3HT films on $MAPbI_3$:quartz and on quartz substrates is shown in Fig. 7.2. Absorption from only the P3HT layer obtained through subtraction of the corresponding $MAPbI_3$ spectrum is depicted in Fig. 7.3. Additionally, normalised (at the absorption peak at 560 nm) and zoomed-in P3HT absorption components from P3HT:$MAPbI_3$:quartz samples are shown in Fig. 7.4. The absorption peak around 615 nm changes relative to the absorption peak at 560 nm for the films on $MAPbI_3$.

7.4 Photoluminescence

The PL spectra of the P3HT films of different thicknesses on quartz and on $MAPbI_3$:quartz are shown in Fig. 7.5. The variation in thickness was achieved by changing spin speed in the fabrication routine from 2000 rpm to 6000 rpm in steps of 1000 rpm. The faster the spin speed, the thinner the sample, which was confirmed with Dektak and absorption measurements (see Table 7.1). The films were excited at 460 nm with a fluence of 3 to 4 $nJ\,cm^{-2}$. The spectra are normalised to the 0-1 transition. P3HT PL peaks are observed at 655 nm (0-0), 725 nm (0-1) and 810 nm (0-2). The peak of the corresponding $MAPbI_3$ PL is at 765 nm. For the P3HT films on quartz (dashed lines), the spectral lineshape of the PL does not change with thickness. A very slight change of the 0-0 feature around 650 nm is likely to be caused by self-absorption. For the P3HT films $MAPbI_3$:quartz (solid lines) there is significant change: the ratio of the 0-0 to 0-1 peak increases compared to the film on quartz and changes with thickness and the spectra are blue-shifted. Furthermore, the P3HT:$MAPbI_3$:quartz films exhibit a change in 0-2 to 0-1 peak intensity with changing thickness/spin speed.

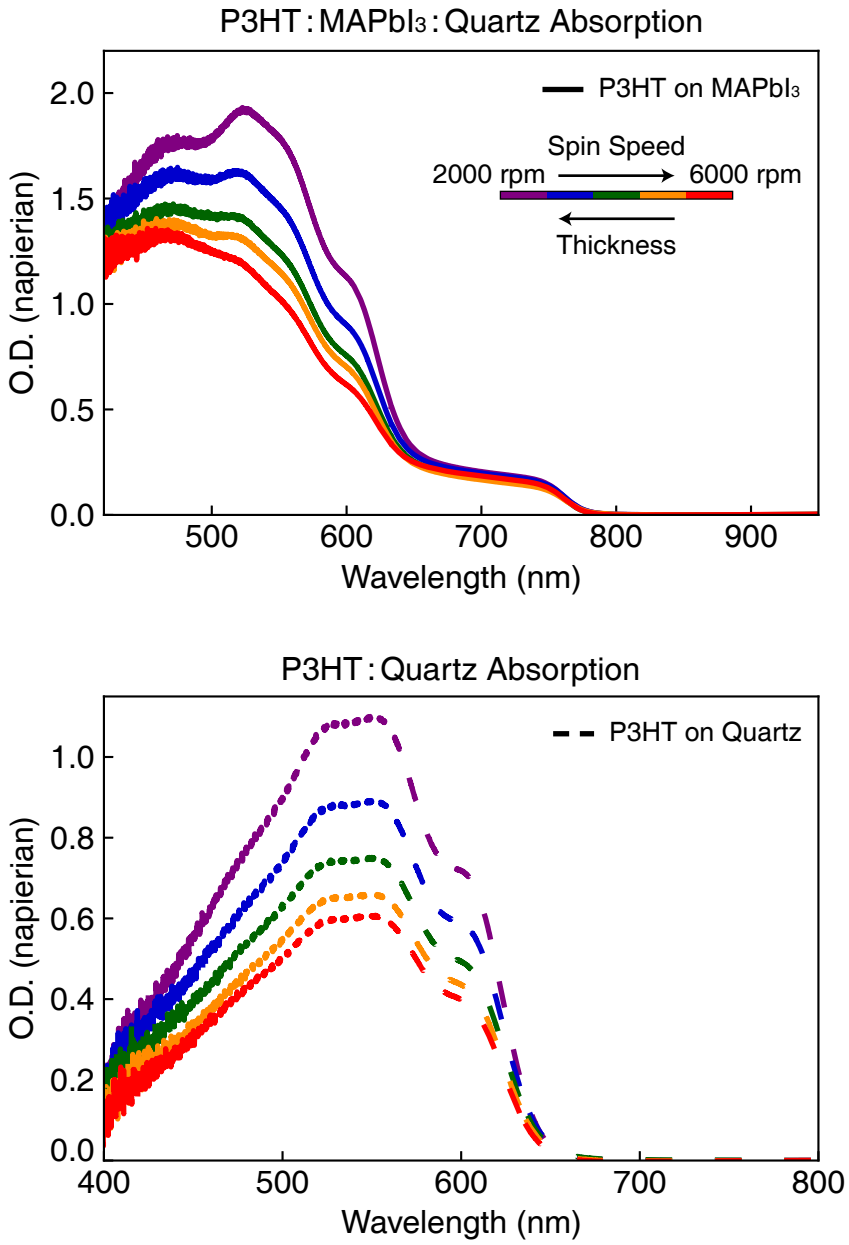


Figure 7.2: Top: Absorption of P3HT films with varying spin speed and thickness (indicated through color spectrum; spin speed changes in steps of 1000 rpm from 2000 rpm to 6000 rpm) on $MAPbI_3$:quartz (solid lines) substrates. Bottom: Absorption of P3HT films with varying spin speed and thickness on quartz (dashed lines) substrates, both measured with NIR source and Si detector.

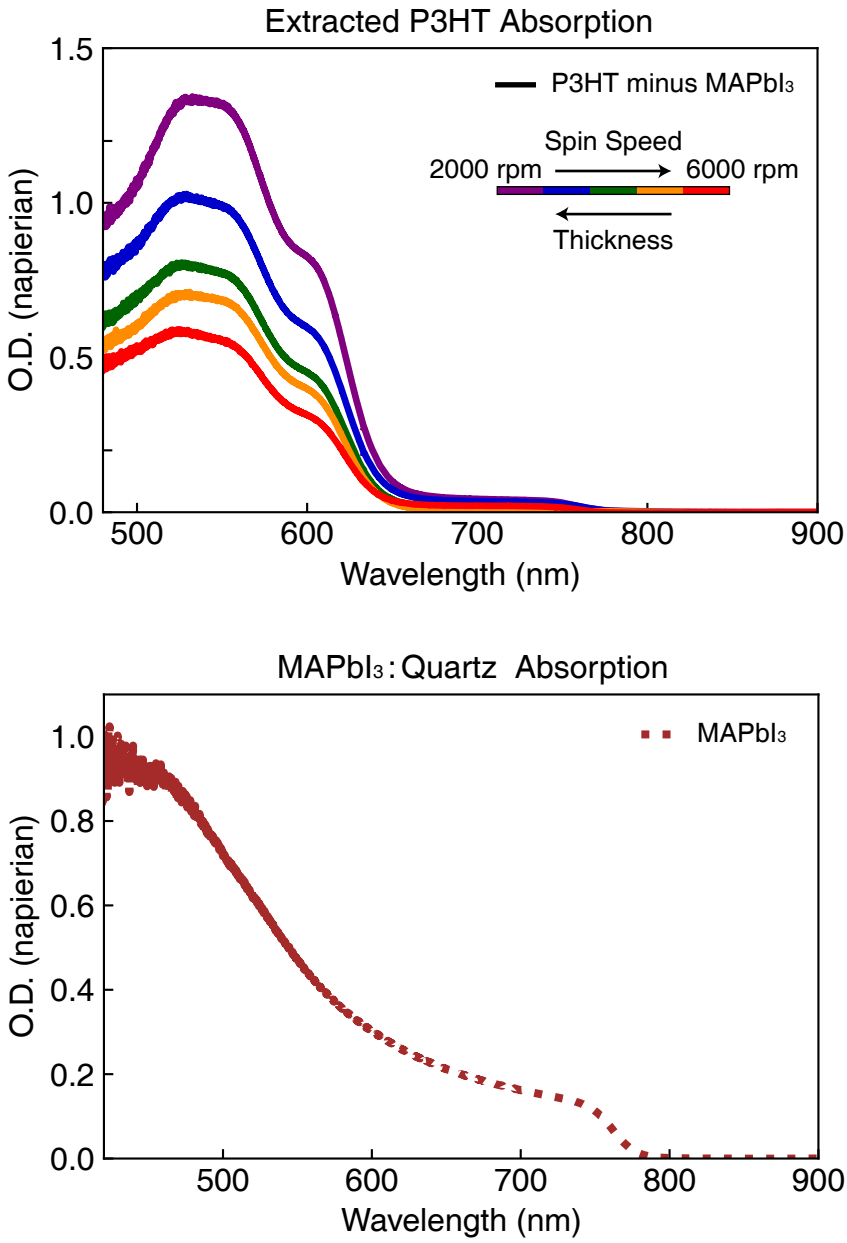


Figure 7.3: Top: P3HT component of P3HT:$MAPbI_3$:quartz absorption from films with varying spin speed and thickness (indicated through color spectrum). The absorption from the $MAPbI_3$ layer was subtracted. Bottom: Absorption of $MAPbI_3$:quartz substrate (brown dotted line), both measured with NIR source and Si detector.

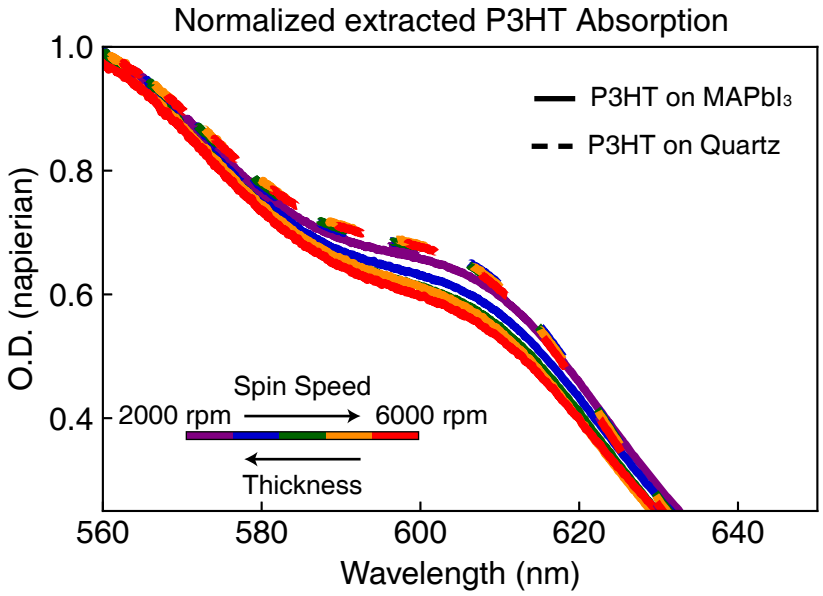


Figure 7.4: Normalised (at 560 nm) P3HT component of absorption from films with varying spin speed and thickness (indicated through color spectrum) on quartz (dashed lines) and $MAPbI_3$:quartz (solid lines) substrates.

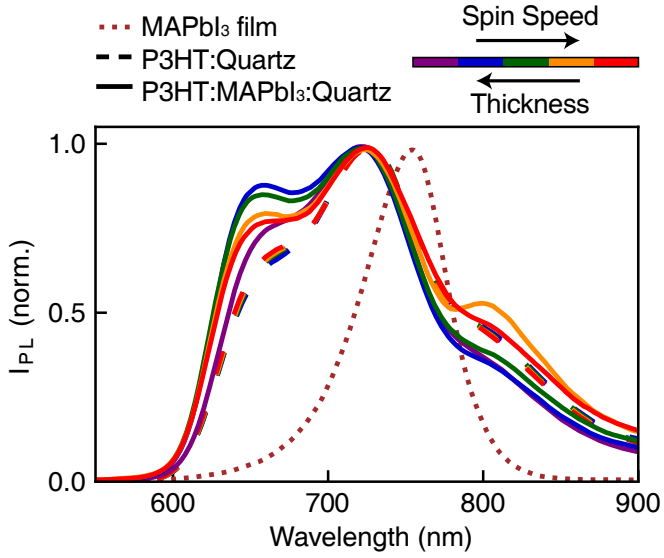


Figure 7.5: Normalised PL intensity from P3HT films with varying spin speed during processing on quartz (dashed lines) and on $MAPbI_3$ (solid lines). Line colors indicate spin speed/film thickness. Spin speed was increased from 1000 to 6000 rpm in steps of 1000 rpm yielding P3HT film thicknesses from 92 to 40 nm for the films on $MAPbI_3$:quartz and 77 to 42 nm for the films on quartz. Film thickness does not scale linearly with spin speed. Normalised PL from a pure $MAPbI_3$ film is shown as a dotted brown line.

7.5 Discussion

The following discussion focuses on structural changes in P3HT films utilised as hole-transport layers in perovskite-based solar cells. Exploring film morphology and aggregate formation within a film is commonly performed by analyzing absorption and PL spectra [48, 52, 54, 56, 222, 223], which are presented for P3HT films on $MAPbI_3$:quartz and on quartz in Sections 7.3 and 7.4 and which will be discussed in the following. The discussion is structured in four sections as follows: First the absorption spectra are briefly commented. Second the PL spectra are analysed for differences between P3HT films deposited on $MAPbI_3$:quartz and on quartz. Third, film thickness-dependent changes in PL spectra from P3HT:$MAPbI_3$ films are discussed. And fourth, implications of the discussion of the spectra are related to film morphology and to implications for perovskite-based solar cells that employ P3HT as a hole-transport layer.

The change in absorption peak around 615 nm for the films on $MAPbI_3$ substrates shown in Figs. 7.4 suggests a change in aggregation with spin speed/film thickness in these films. This is not the case for the P3HT films on quartz substrates. The change is least prominent for the thickest film spun at the lowest spin speed, which agrees with changes observed in the PL spectra (cf. Fig. 7.5) on which the discussion will mainly focus. The absorption spectra presented here are obtained by subtracting the $MAPbI_3$ absorption spectrum and might therefore be more prone to error than the PL, which stems only from P3HT (cf. $MAPbI_3$ PL peak in Fig. 7.5). Furthermore, a recent study highlighted that PL is more suited for the study of aggregation in P3HT thin films of different thickness than absorption [54].

For the discussion of the PL spectra, first, a comparison is made between steady-state PL from P3HT films on a quartz substrate (dashed lines in Fig. 7.5) and the PL from the films on $MAPbI_3$:quartz (solid lines in Fig. 7.5). The observations are

discussed within the framework of weakly interacting H-aggregates, which form due to interchain interactions of the P3HT chromophores as outlined in Section 7.1. For the films on $MAPbI_3$:quartz, a blue-shift and an increase in 0-0 to 0-1 PL peak ratio is observed compared to the films on quartz, which corresponds to a weaker H-aggregate signature of suppressed 0-0 emission. The detected relative increase of the 0-0 peak of the PL from the films on $MAPbI_3$ can be attributed to a decrease in interchain (through space) coupling, stemming from microstructural differences between those P3HT films [49, 54, 56]. A change in film morphology leading to less H-aggregate formation in P3HT films has been observed previously for films deposited on substrates with considerable surface roughness [54, 224]. The observations based on Fig. 7.5 more specifically agree with the work of Ehrenreich et al. [54] who compared PL lineshapes from a thin and a thick P3HT film on metal halide perovskite. They attributed the difference to a P3HT film structure composed of an amorphous region with less interchain interaction formed at the interface to the rough metal halide perovskite and a more ordered region further away from this interface. A thin P3HT film is more dominated by PL from the amorphous, less H-aggregated region than the thick film and its 0-0 emission is thus less suppressed. In agreement with this, the PL features from the thickest (2000 rpm) P3HT film on $MAPbI_3$:quartz presented in Fig. 7.5 are most alike to the PL lineshape of the films on a smooth quartz substrate while the thinner (3000 rpm to 6000 rpm) films show a more pronounced relative increase of the 0-0 PL peak and are more blue-shifted, which is a stronger signature of the amorphous phase at the $MAPbI_3$ interface.

So far, the focus was on the difference between P3HT films on a quartz substrate and on $MAPbI_3$:quartz. However, there are additional differences in the PL spectra between films with varying thickness on a $MAPbI_3$:quartz substrate. Such a thickness dependence of the spectral lineshape of P3HT emission is observed only for P3HT films

on the rough $MAPbI_3$:quartz and not for P3HT films on smooth quartz implying that further changes in aggregation are connected to the roughness of the $MAPbI_3$ surface.

One such difference in PL spectra is a decrease in relative 0-0 PL peak intensity with decreasing film thickness for all but the thickest P3HT:$MAPbI_3$:quartz film is (see Fig. 7.5). This is somewhat opposite to what would be expected from the explanation of film thickness-dependent emission stemming either mainly from the amorphous layer close to $MAPbI_3$ (thinner films) or from a more ordered and H-aggregated layer on top (thicker films) and needs further discussion.

Before discussing this observation, PL spectral changes of the P3HT:$MAPbI_3$:quartz films occurring with different film thickness are further analysed: The relative intensity of the 0-0 peak decreases with decreasing film thickness and thus increasing spin speed. Within the framework of H-aggregates, this indicates that the interchain interaction is stronger in these thinner, faster spun-cast films [52, 213]. Additionally, the relative intensity of the 0-2 to 0-1 PL peak in Fig. 7.5 changes with thickness and therefore with spin speed for the P3HT film on $MAPbI_3$: The 0-2 to 0-1 ratio is highest for the two thinnest films (5000 rpm and 6000 rpm), which also have a lower 0-0 to 0-1 peak ratio compared to the two intermediate films (3000 rpm and 4000 rpm).

For the discussion of these observations, the framework is extended to the HJ-aggregate model [49], which accounts for the interplay between inter- (through space) and intrachain (through the polymer bond) coupling. The strength of the two interactions can be assessed from the ratios of the 0-0 to 0-1 peak and of the 0-2 to 0-1 peak. It has been shown that the 0-2 to 0-1 PL peak ratio is predominantly determined by intrachain (through bond) interactions and a decrease in relative peak intensity signifies stronger intrachain coupling [56]. The ratio of the 0-0 to 0-1 PL peak is an indication of the strength of interchain (through space) interaction as discussed above and still a main factor in the HJ-aggregate model [225]. In addition to that, when intrachain interaction is considered as well, the interplay between inter- and intrachain interaction also influences the 0-0 to 0-1 peak ratio: stronger intrachain

interaction leads to an increase in 0-0 to 0-1 peak ratio [56]. Applied to the P3HT films on $MAPbI_3$, interchain coupling strengthens (0-0 to 0-1 PL ratio decreases) and intrachain coupling weakens (0-2 to 0-1 PL ratio increases) for the two thinnest films spun-cast at highest spin speeds compared to the two films spun-cast at intermediate spin speeds. At this point, it is however important to notice that the changes in PL intensity ratios observed here are far weaker than the changes for example observed for P3HT nanofibers displaying mainly J-aggregate behaviour [55]. The P3HT thin films spun-cast on $MAPbI_3$:quartz are therefore still considered to predominantly exhibit H-aggregation behaviour but in order to fully understand their PL spectral lineshape, intrachain interactions need to be taken into account through the HJ-aggregate model.

Finally, the changes in interaction strengths are related to film morphology, which is graphically summarised in Fig. 7.6. Weaker interchain (through space) interaction and stronger intrachain (through bond) interaction has been found for films with a two-phase morphology with interconnected crystalline and amorphous phases compared to films with a chain-extended morphology comprising of layered stacks with high torsional disorder [56, 225]. The above discussion on thickness/spin speed dependent changes in interaction strengths for P3HT:$MAPbI_3$:quartz films allows to draw the following conclusions with respect to their morphology:

i) An amorphous phase at the interface to the $MAPbI_3$ causes a decrease in interchain interaction compared to films on a smooth quartz substrate. As Ehrenreich et al. [54] point out, this film structure results in a loss channel for hole transport in perovskite-based solar cells due to an energetically enhanced HOMO (highest occupied molecular orbital) in the amorphous interface area of the polymer [226] preventing efficient charge transport [227].

ii) The change in intrachain interaction for various thin films on $MAPbI_3$ additionally indicates more torsional disorder and possibly a less amorphous phase in the

thinner films spun-cast at high speeds. This change in morphology is likely related not only to the change in thickness but to the spin speed with a higher spin speed causing more torsional disorder in the film deposited on a rough substrate.

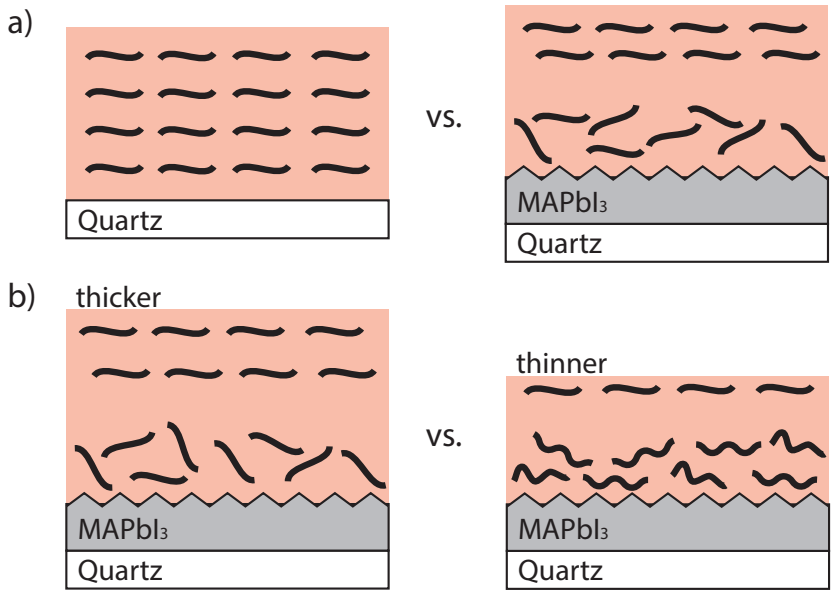


Figure 7.6: Schematic depiction of changes in P3HT film morphology with P3HT film thickness and substrate. a) P3HT films spun-cast on the rougher $MAPbI_3$:quartz substrate form an amorphous phase at the interface compared to films spun-cast on the smooth quartz substrate directly. b) Thinner P3HT films, spun-cast at higher spin speeds possibly form with the polymer chains exhibiting more torsional disorder and a less amorphous phase at the $MAPbI_3$ interface.

7.6 Summary and Conclusion

This chapter explored the influence of thickness and spin speed during fabrication on film morphology of the hole-transport material P3HT. To this end, P3HT films were deposited on a metal halide perovskite layer, which is a configuration found in perovskite-based solar cells. Changes in aggregation for P3HT films with varying thickness spun-cast on a $MAPbI_3$ layer indicate the presence of an amorphous phase at the interface, which is expected to negatively influence the performance of solar cell devices as reported previously [54]. In addition to validating this effect, comparing a range of different film thicknesses of P3HT led to new insights as the effect is weakened for thinner films spun-cast at high spin speed in which also a higher degree of torsional disorder is observed. Thinner and faster spun-cast P3HT may therefore be beneficial for perovskite-based solar cell performance but further investigation is needed.

Furthermore, this chapter highlights that in order to fully understand morphological changes in thin films of P3HT spun-cast on a $MAPbI_3$ layer, both, interchain and intrachain interactions between P3HT chromophores need to be considered. The HJ-aggregate model can therefore more accurately account for morphological changes between films of different thicknesses than the commonly employed model of weakly coupled H-aggregates, which only accounts for interchain interactions.

8 Conclusion and Outlook

This thesis expands the fundamental understanding of the optoelectronic properties of different organic semiconductors. Continuous investigation of organic semiconductors is crucial for their successful application in technologies such as OLEDs and solar cells. In the following, the specific findings from each thesis chapter and their implications for the respective field of research including future investigations are summarised.

Chapters 4 and 5, explored the influence of the fraction of β-phase chains present in thin films of the blue-emitting polymer PFO on the nature of the electronic states, chain conformation and Förster resonant energy transfer from glassy- to β-phase chain segments. Consistency amongst PFO films was ensured by employing the same fabrication technique to obtain a wide range of β-phase fractions. It was demonstrated that such comparability is of great importance as photophysical properties of PFO films are very sensitive to film microstructure and therefore to film preparation. All PFO films fabricated exhibited high (> 0.6 for the films containing β-phase) PLQE, peaking at a value of 0.72 at 25.6% β-phase content. The emission peaks of the β-phase were observed to red-shift and narrow while the associated Huang-Rhys factor decreases with increasing β-phase content. These findings suggest that the conformation of β-phase

segments changes with increasing fraction, adopting a more planar structure and/or including a larger number of repeat units. The red-shift in PFO emission also affects the resonance condition for energy transfer between glassy-phase and β-phase chain segments, which results in a slight decrease in Förster radius with increasing β-phase fraction. By comparing the Förster radii obtained from spectral overlap calculations to those extracted from measurements of transient PL dynamics, the Förster radius is found to be enhanced by exciton diffusion within the glassy phase occurring prior to energy transfer. The insights obtained from this systematic study deepen the understanding of the fundamental photophysical properties of PFO films, which is essential for the further development of light-emitting materials and applications.

Possible directions of further research include performing grazing-incidence wide-angle X-ray scattering (GIWAXS) on PFO films with varying β-phase and low-temperature measurements of absorption, PL and PL transients. GIWAXS can be employed to investigate and understand molecular packing and orientation in thin films [228] and therefore possible interactions between the PFO chain segments that have adapted β-phase and their contribution to the increased effective π-conjugation with increasing β-phase content in PFO thin films. GIWAXS measurements could lead to a better understanding of the microstructural changes causing the more planar β-phase chain segments and/or the larger number of repeat units in PFO thin films with increasing β-phase content. Low temperature measurements could be insightful as at low temperatures, certain exciton diffusion mechanisms that influence PL transients and the obtained Förster radius freeze out. Enlargement of the Förster radius through exciton diffusion prior to the energy transfer event would therefore be reduced and it would be expected that the values of Förster radii determined from low-temperature PL transients and from spectral overlap calculations would converge. Furthermore, low-temperature spectral analysis could offer additional insights into the electronic states of PFO thin films with a reliably tuned β-phase content.

Chapter 6 assessed the potential of efficient energy transfer to overcome parasitic light absorption in sun-facing charge transport layers (CTL) of metal halide perovskite (MHP)-based solar cells. Energy transfer from different conjugated polymer layers to a $MAPbI_3$ layer was experimentally observed and the PL dynamics from the polymer films on a $MAPbI_3$ layer were successfully simulated. The results from PL decay modelling were used to calibrate the calculation of the energy transfer efficiency for a photoexcited organic semiconductor layer on top of a $MAPbI_3$ layer. On the basis of the developed modelling approach, significant energy transfer from a photoexcited molecular CTL to the MHP is expected for organic semiconductors with high PLQE and/or very thin ($\leq$ 10 nm) layers. Parasitic light absorption in a front CTL was therefore shown to not necessarily lead to losses but efficient energy transfer to the MHP can enhance the photocurrent of the device, allowing devices to reach their limits. The modelling results also highlight that is not necessary for the organic semiconductor to be fully transparent at the wavelengths of MHP absorption if the CTL material exhibits high PLQE, which considerably widens the field of possible future candidates for charge-extraction layers. Further research, synthesis and exploration of new CTL material candidates within the field of MHP-based solar cells could follow from these findings.

In **Chapter 7**, thickness but also variation of spin speed during the fabrication process were found to influence aggregation in P3HT films deposited on a $MAPbI_3$ layer. The formation of a previously observed amorphous layer at the MHP interface was confirmed, which has a negative impact for MHP-based solar cell devices. New insights were gained on how thickness and variation of spin speed influence aggregation and the formation of the amorphous phase. Thin P3HT films spun-cast at high spin speed possibly reduce the negative impact on devices. More research is however needed to confirm this finding. Further insights could be gained by measuring and comparing the glass transition temperature of P3HT films with varying thickness/spin

speed deposited on a $MAPbI_3$ layer and by performing GIWAXS on them. These two techniques enable studying molecular order, specifically in terms of Π-Π-stacking and lamellar stacking in thin films of conjugated polymers [229] and could provide more information on how film microstructure changes with variation in P3HT film thickness and processing spin-speed. Such insights could in turn be linked to the electronic properties of the thin films, which are decisive for their operation in MHP solar cells and could therefore lead to a better understanding on how P3HT thin film processing influences solar cell performance. The discussion of aggregates in P3HT films also highlighted that for a full understanding of the observed changes in aggregation, an extended HJ-aggregate model needs to be considered. This contributes to the broader discussion of the nature of aggregates in P3HT thin films.

References

[1] IPCC. 'IPCC Special Report on Renewable Energy Sources and Climate Change Mitigation'. Ed. by Edenhofer, O.; Richs-Madruga, R.; Sokona, Y.; Seyboth, K.; Matschoss, P.; Kadner, S.; Zwickel, T.; Eickemeier, P.; Hansen, G.; Schlömer, S. *et al.* Cambridge University Press, Cambridge, United Kingdom and New York, NY, USA, 2011.

[2] European Comission. *Clean Energy for all Europeans*. 2019.

[3] IEA. *World Energy Outlook 2019*. 2019.

[4] IPCC. 'IPCC Special Report on the impacts of global warming of 1.5°C above pre-industrial levels and related global greenhouse gas emission pathways, in the context of strengthening the global response to the threat of climate change'. Ed. by Masson-Delmotte, V.; Zhai, P.; Pörtner, H.-O.; Roberts, D.; Skea, J.; Shukla, P. R.; Pirani, A.; Moufouma-Okia, W.; Péan, C.; Pidcock, R. *et al.* Cambridge University Press, Cambridge, United Kingdom and New York, NY, USA, 2018.

[5] Geels, F. W.; Berkhout, F. and Van Vuuren, D. P. 'Bridging analytical approaches for low-carbon transitions'. *Nat. Clim. Change*, 2016, **6**, 576–583.

[6] Eyre, N.; Darby, S. J.; Grünewald, P.; McKenna, E. and Ford, R. 'Reaching a 1.5°C target: socio-technical challenges for a rapid transition to low-carbon electricity systems'. *Philos. Trans. R. Soc. A*, 2018, **376**, 20160462.

[7] Shell. *World Energy Model: A View to 2100*. 2017.

[8] Eggimann, S.; Usher, W.; Eyre, N. and Hall, J. W. 'How weather affects energy demand variability in the transition towards sustainable heating'. *Energy*, 2020, **195**, 116947.

[9] Unruh, G. C. 'Escaping carbon lock-in'. *Energy Policy*, 2002, **30**, 317–325.

[10] Şen, Z. 'Solar energy in progress and future research trends'. *Prog. Energy Combust. Sci.*, 2004, **30**, 367–416.

[11] Kabir, E.; Kumar, P.; Kumar, S.; Adelodun, A. A. and Kim, K. H. 'Solar energy: Potential and future prospects'. *Renew. Sustain. Energy Rev.*, 2018, **82**, 894–900.

[12] *http://www.exeter.ac.uk/research/inspiring/keythemes/science/climate/ (accessed 2018-04-16)*.

[13] Köhler, A. and Bässler, H. *Electronic Processes in Organic Semiconductors*. Wiley-VCH Verlag GmbH & Co, 2015.

[14] Facchetti, A. 'π-Conjugated Polymers for Organic Electronics and Photovoltaic Cell Applications'. *Chem. Mater.*, 2011, **23**, 733–758.

[15] Guo, X.; Baumgarten, M. and Müllen, K. 'Designing π-Conjugated Polymers for Organic Electronics'. *Prog. Polym. Sci.*, 2013, **38**, 1832–1908.

[16] Chiang, C. K.; Fincher, C. R.; Park, Y. W.; Heeger, A. J.; Shirakawa, H.; Louis, E. J.; Gau, S. C. and MacDiarmid, A. G. 'Electrical Conductivity in Doped Polyacetylene'. *Phys. Rev. Lett.*, 1977, **39**, 1098–1101.

[17] Heeger, A. J. 'Nobel Lecture: Simuconducting and Metallic Polymers: The Fourth Generation of Polymeric Materials.' *J. Phys. Chem. B*, 2001, **105**, 8475–8491.

[18] Hedley, G. J.; Ruseckas, A. and Samuel, I. D. W. 'Light Harvesting for Organic Photovoltaics'. *Chem. Rev.*, 2017, **117**, 796–837.

[19] Sirringhaus, H. '25th Anniversary Article: Organic Field-Effect Transistors: The Path Beyond Amorphous Silicon'. *Adv. Mater.*, 2014, **26**, 1319–1335.

[20] Tang, C. W. and Slyke, S. A. van. 'Organic electroluminescent diodes'. *Appl. Phys. Lett.*, 1987, **51**, 913–915.

[21] Friend, R. H.; Gymer, R. W.; Holmes, A. B.; Burroughes, J. H.; Marks, R. N.; Taliani, C.; Bradley, D. D.; Dos Santos, D. A.; Brédas, J. L.; Lögdlund, M. *et al.* 'Electroluminescence in conjugated polymers'. *Nature*, 1999, **397**, 121–128.

[22] Kraft, A.; Grimsdale, A. C. and Holmes, A. B. 'Electroluminescent Conjugated Polymers-Seeing Polymers in a New Light'. *Angew. Chem. Int. Ed.*, 1998, **37**, 402–428.

[23] Burroughes, J. H.; Bradley, D. D. C.; Brown, A. R.; Marks, R. N.; Mackay, K.; Friend, R. H.; Burns, P. L. and Holmes, A. B. 'Light-emitting diodes based on conjugated polymers'. *Nature*, 1990, **347**, 539–541.

[24] Chen, H.; Guo, Y.; Yu, G.; Zhao, Y.; Zhang, J.; Gao, D.; Liu, H. and Liu, Y. 'Highly π-Extended Copolymers with Diketopyrrolopyrrole Moieties for High-Performance Field-Effect Transistors'. *Adv. Mater.*, 2012, **24**, 4618–4622.

[25] Bronstein, H.; Chen, Z.; Shahid Ashraf, R.; Zhang, W.; Du, J.; Durrant, J. R.; Shakya Tuladhar, P.; Song, K.; Watkins, S. E.; Geerts, Y. *et al.* 'Thieno[3,2-b]thiophene-Diketopyrrolopyrrole-Containing Polymers for High-Performance Organic Field-Effect Transistors and Organic Photovoltaic Devices'. *J. Am. Chem. Soc*, 2011, **133**, 3272–3275.

[26] Kola, S.; Sinha, J. and Katz, H. E. 'Organic Transistors in the New Decade: Toward n-Channel, Printed and Stabilized Devices'. *J. Polym. Sci. B*, 2012, **50**, 1090–1120.

[27] Günes, S.; Neugebauer, H. and Sariciftci, N. S. 'Conjugated Polymer-Based Organic Solar Cells'. *Chem. Rev.*, 2007, **107**, 1324–1338.

[28] Li, G.; Zhu, R. and Yang, Y. 'Polymer solar cells'. *Nat. Photonics*, 2012, **6**, 153–161.

[29] Zhao, J.; Li, Y.; Yang, G.; Jiang, K.; Lin, H.; Ade, H.; Ma, W. and Yan, H. 'Efficient organic solar cells processed from hydrocarbon solvents'. *Nat. Energy*, 2016, **1**, 1–7.

[30] Förster, T. 'Zwischenmolekulare Energiewanderung und Fluoreszenz'. *Ann. Phys.*, 1948, **2**, 55–75.

[31] Alger, M. *Polymer Science Dictionary*. Springer, 2017.

[32] Strobl, G. R. *The Physics of Polymers*. Springer-Verlag Berlin Heidelberg, 1997.

[33] Valeur, B. and Berberan-Santos, M. N. *Molecular Fluorescence: Principles and Applications*. Wiley-VCH Verlag GmbH & Co, 2012.

[34] Torras, J.; Casanovas, J. and Alemán, C. 'Reviewing Extrapolation Procedures of the Electronic Properties on the π-Conjugated Polymer Limit'. *J. Phys. Chem. A*, 2012, **116**, 7571–7583.

[35] Kuhn, H. 'A Quantum-Mechanical Theory of Light Absorption of Organic Dyes and Similar Compounds'. *J. Chem. Phys.*, 1949, **17**, 1198–1212.

[36] Chang, J. C. 'Monopole effects on electronic excitation interactions between large molecules. I. Application to energy transfer in chlorophylls'. *J. Chem. Phys.*, 1977, **67**, 3901.

[37] Kohler, B. E. 'A simple model for linear polyene electronic structure'. *J. Chem. Phys.*, 1990, **93**, 5838–5842.

[38] Lewis, G. N. and Calvin, M. 'The color of organic substances'. *Chem. Rev.*, 1939, **25**, 273–328.

[39] Kuhn, W. 'Über das Absorptionsspektrum der Polyene'. *Helv. Chim. Acta*, 1948, **31**, 1780–1799.

[40] Beljonne, D.; Cornil, J.; Silbey, R.; Millié, P. and Brédas, J. L. 'Interchain interactions in conjugated materials: The exciton model versus the supermolecular approach'. *J. Chem. Phys.*, 2000, **112**, 4749.

[41] Herz, L. M. 'Charge-Carrier Dynamics in Organic-Inorganic Metal Halide Perovskites'. *Annu. Rev. Phys.*, 2016, **67**, 65–89.

[42] Cogdell, R. J.; Gall, A. and Köhler, J. 'The architecture and function of the light-harvesting apparatus of purple bacteria: from single molecules to in vivo membranes.' *Q. Rev. Biophys.*, 2006, **39**, 227–324.

[43] Wannier, G. H. 'The Structure of Electronic Excitation Levels in Insulating Crystals'. *Phys. Rev.*, 1937, **52**, 191–197.

[44] Frenkel, J. 'On the transformation of light into heat in solids. I'. *Phys. Rev.*, 1931, **37**, 17–44.

[45] Landau, L. 'Über Die Bewegung der Elektronen in Kristallgitter'. *Phys. Z. Sowjetunion*, 1933, **3**, 644–645.

[46] Brédas, J. L.; Cornil, J. and Heeger, A. J. 'The exciton binding energy in luminescent conjugated polymers'. *Adv. Mater.*, 1996, **8**, 447–452.

[47] Kasha, M. 'Energy Transfer Mechanisms and the Molecular Exciton Model for Molecular Aggregates'. *Radiat. Res.*, 1963, **20**, 55.

[48] Spano, F. C. and Silva, C. 'H- and J-Aggregate Behavior in Polymeric Semiconductors'. *Annu. Rev. Phys. Chem.*, 2014, **65**, 477–500.

[49] Yamagata, H. and Spano, F. C. 'Interplay between intrachain and interchain interactions in semiconducting polymer assemblies: The HJ-aggregate model'. *J. Chem. Phys.*, 2012, **136**, 184901.

[50] Noriega, R.; Rivnay, J.; Vandewal, K.; Koch, F. P.; Stingelin, N.; Smith, P.; Toney, M. F. and Salleo, A. 'A general relationship between disorder, aggregation and charge transport in conjugated polymers'. *Nat. Mater.*, 2013, **12**, 1038–1044.

[51] Botiz, I. and Stingelin, N. 'Influence of Molecular Conformations and Microstructure on the Optoelectronic Properties of Conjugated Polymers'. *Materials*, 2014, **7**, 2273–2300.

[52] Spano, F. C. 'The Spectral Signatures of Frenkel Polarons in H-and J-Aggregates'. *Acc. Chem. Res.*, 2010, **43**, 429–439.

[53] Panzer, F.; Sommer, M.; Bässler, H.; Thelakkat, M. and Köhler, A. 'Spectroscopic Signature of Two Distinct H-Aggregate Species in Poly(3-hexylthiophene)'. *Macromolecules*, 2015, **48**, 1543–1553.

[54] Ehrenreich, P.; Birkhold, S. T.; Zimmermann, E.; Hu, H.; Kim, K. D.; Weickert, J.; Pfadler, T. and Schmidt-Mende, L. 'H-aggregate analysis of P3HT thin films-Capability and limitation of photoluminescence and UV/Vis spectroscopy'. *Sci. Rep.*, 2016, **6**, 32434.

[55] Niles, E. T.; Roehling, J. D.; Yamagata, H.; Wise, A. J.; Spano, F. C.; Moulé, A. J. and Grey, J. K. 'J-Aggregate Behavior in Poly-3-hexylthiophene Nanofibera'. *J. Phys. Chem. Lett.*, 2012, **3**, 259–263.

[56] Paquin, F.; Yamagata, H.; Hestand, N. J.; Sakowicz, M.; Bérubé, N.; Côté, M.; Reynolds, L. X.; Haque, S. A.; Stingelin, N.; Spano, F. C. *et al.* 'Two-dimensional spatial coherence of excitons in semicrystalline polymeric semiconductors: Effect of molecular weight'. *Phys. Rev. B*, 2013, **88**, 155202.

[57] Dexter, D. L. 'A Theory of Sensitized Luminescence in Solids'. *J. Chem. Phys.*, 1953, **21**, 836–859.

[58] Förster, T. 'Energiewanderung und Fluoreszenz'. *Sci. Nat.*, 1946, **6**, 166–175.

[59] Förster, T. 'Experimentelle und Theoretische Untersuchung des Zwischenmolekularen Übergangs von Elektroneneanregungsenergie'. *Z. Naturforsch.*, 1949, **4a**, 321–327.

[60] Clegg, R. M. 'Nuts and bolts of excitation energy migration and energy transfer'. *Chlorophyll a Fluorescence - A Signature of Photosynthesis*. Ed. by Papgeorgiou, G. C. and Govindjee. Heidelberg: Springer, 2010, 83–105.

[61] Scholes, G. D. 'Long-Range Resonance Energy Transfer in Molecular Systems'. *Annu. Rev. Phys. Chem.*, 2003, **54**, 57–87.

[62] Brédas, J.; Beljonne, D.; Coropceanu, V. and Cornil, J. 'Charge-Transfer and Energy-Transfer Processes in π-Conjugated Oligomers and Polymers: A Molecular Picture'. *Chem. Rev.*, 2004, **104**, 4971–5003.

[63] Beenken, W. J. D. and Pullerits, T. 'Excitonic coupling in polythiophenes: Comparison of different calculation methods'. *J. Chem. Phys.*, 2004, **120**, 2490.

[64] Medintz, I. and Hildebrandt, N., eds. *FRET - Förster Resonance Energy Transfer*. Wiley-VCH Verlag GmbH & Co, 2014.

[65] Perrin, J. 'Fluorescence et induction moleculaire par resonance'. *C. R. Acad. Sci.*, 1927, **184**, 1097–1100.

[66] Perrin, F. 'Théorie quantique des transferts d'activation entre molecules de même espèce. Cas des solutions fluorescentes'. *Ann. Phys.*, 1932, **17**, 283–313.

[67] Gaviola, E. and Pringsheim, P. 'Über den Einfluss der Konzentration oaf de Polarisation der Fluoreszenz von Farbstofflösungen'. *Z. Phys.*, 1924, **24**, 24–36.

[68] Feofilov, P. P. and Sveshnikov, B. J. 'On the concentrational depolarization of the fluorescence of dye-stuff solutions'. *J. Phys. USSR*, 1940, **3**, 493–505.

[69] De Member, J. R. and Filipescu, N. 'Intramolecular Energy Transfer between Nonconjugated Chromophores. Effect of Rigid Perpendicular Orientation'. *J. Am. Chem. Soc.*, 1968, **90**, 6425–6428.

[70] Braslavsky, S. E.; Fron, E.; Rodríguez, H. B.; Román, E. S.; Scholes, G. D.; Schweitzer, G.; Valeur, B. and Wirz, J. 'Pitfalls and limitations in the practical use of Förster's theory of resonance energy transfer'. *Photochem. Photobiol. Sci.*, 2008, **7**, 1444–1448.

[71] Förster, T. '10th Spiers Memorial Lecture. Transfer Mechanisms of Electronic Excitation'. *Discuss. Faraday Soc.*, 1959, **27**, 7–17.

[72] Grage, M.; Zaushitsyn, Y.; Yartsev, A.; Chachisvilis, M.; Sundström, V. and Pullerits, T. 'Ultrafast excitation transfer and trapping in a thin polymer film'. *Phys. Rev. B*, 2003, **67**, 205207.

[73] Westenhoff, S.; Daniel, C.; Friend, R. H.; Silva, C.; Sundström, V. and Yartsev, A. 'Exciton migration in a polythiophene: Probing the spatial and energy domain by line-dipole Förster-type energy transfer'. *J. Chem. Phys.*, 2005, **122**.

[74] Menelaou, C.; Schiphorst, J. T.; Kendhale, A. M.; Parkinson, P.; Debije, M. G.; Schenning, A. P. H. J. and Herz, L. M. 'Rapid Energy Transfer Enabling Control of Emission Polarization in Perylene Bisimide Donor-Acceptor Triads'. *J. Phys. Chem. Lett.*, 2015, **6**, 1170–1176.

[75] Schmid, S. A.; Abbel, R.; Schenning, A.; Meijer, E. W. and Herz, L. M. 'Energy transfer processes along a supramolecular chain of π-conjugated molecules'. *Philos. Trans. R. Soc. A*, 2012, **370**, 3787–3801.

[76] Schmid, S. A.; Abbel, R; Schenning, A. P. H.; Meijer, E. W.; Sijbesma, R. P. and Herz, L. M. 'Analyzing the Molecular Weight Distribution in Supramolecular Polymers'. *J. Am. Chem. Soc.*, 2009, **131**, 17696–17704.

[77] Schmid, S. A.; Abbel, R.; Schenning, A. P. H. J.; Meijer, E. W. and Herz, L. M. 'Impact of nuclear lattice relaxation on the excitation energy transfer along a chain of π-conjugated molecules'. *Phys. Rev. B*, 2010, **81**, 1–5.

[78] Parkinson, P.; Knappke, C. E. I.; Kamonsutthipaijit, N.; Sirithip, K.; Matichak, J. D.; Anderson, H. L. and Herz, L. M. 'Ultrafast Energy Transfer in Biomimetic Multristrand Nanorings'. *J. Am. Chem. Soc.*, 2014, **136**, 8217–8220.

[79] Parkinson, P.; Kamonsutthipaijit, N.; Anderson, H. L. and Herz, L. M. 'Size-Independent Energy Transfer in Biomimetic Nanoring Complexes'. *ACS Nano*, 2016, **10**, 5933–5940.

[80] Levine, I. N. *Quantum Chemistry*. Pearson Prentice Hall Upper Saddle River, NJ, 2000.

[81] Beljonne, D; Pourtois, G; Silva, C; Hennebicq, E; Herz, L. M.; Friend, R. H.; Scholes, G. D.; Setayesh, S; Mullen, K and Bredas, J. L. 'Interchain vs. intrachain energy transfer in acceptor-capped conjugated polymers'. *Proc. Natl. Acad. Sci.*, 2002, **99**, 10982–10987.

[82] Marguet, S.; Markovitsi, D.; Millié, P. and Hervé, S. 'Influence of Disorder on Electronic Excited States: An Experimental and Numerical Study'. *J. Phys. Chem. B*, 1998, **102**, 4697–4710.

[83] Krueger, B. P.; Scholes, G. D. and Fleming, G. R. 'Calculation of Couplings and Energy-Transfer Pathways between the Pigments of LH2 by the ab Initio Transition Density Cube Method'. *J. Chem. Phys. B*, 1998, **102**, 5378–5386.

[84] Ridley, J. and Zerner, M. 'An Intermediate Neglect of Differential Overlap Technique for Spectroscopy" Pyrrole and the Azines'. *Theoret. Chim. Acta (Berl.)*, 1973, **32**, 111–134.

[85] Bacon, A. D. and Zerner, M. C. 'An intermediate neglect of differential overlap theory for transition metal complexes: Fe, Co and Cu chlorides'. *Theoret. Chim. Acta (Berl.)*, 1979, **53**, 21–54.

[86] Thompson, M. A. and Zerner, M. C. 'A Theoretical Examination of the Electronic Structure and Spectroscopy of the Photosynthetic Reaction Center from Rhodopseudomonas viridis'. *J. Am. Chem. Soc.*, 1991, **113**, 8210–8215.

[87] Hennebicq, E.; Pourtois, G.; Scholes, G. D.; Herz, L. M.; Russell, D. M.; Silva, C.; Setayesh, S.; Grimsdale, A. C.; Müllen, K.; Brédas, J. L. *et al.* 'Exciton Migration in Rigid-Rod Conjugated Polymers: An Improved Fo1rster Model'. *J. Am. Chem. Soc.*, 2005, **127**, 4744–4762.

[88] Poulsen, L.; Jazdzyk, M.; Communal, J. E.; Sancho-García, J. C.; Mura, A.; Bongiovanni, G.; Beljonne, D.; Cornil, J.; Hanack, M.; Egelhaaf, H. J. *et al.* 'Three-Dimensional Energy Transport in Highly Luminescent Host-Guest Crystals: A Quantitative Experimental and Theoretical Study'. *J. Am. Chem. Soc.*, 2007, **129**, 8585–8593.

[89] Daniel, C.; Westenhoff, S.; Makereel, F.; Friend, R. H.; Beljonne, D.; Herz, L. M. and Silva, C. 'Monte Carlo Simulation of Exciton Bimolecular Annihilation Dynamics in Supramolecular Semiconductor Architectures'. *J. Phys. Chem.*, 2007, **111**, 19111–19119.

[90] Nguyen, T.-Q.; Wu, J.; Doan, V.; Schwartz, B. J. and Tolbert, S. H. 'Control of Energy Transfer in Oriented Conjugated Polymer – Mesoporous Silica Composites'. *Science*, 2000, **288**, 652–656.

[91] Stryer, L. 'Fluorescence Energy Transfer as a Spectroscopic Ruler'. *Ann. Rev. Biochem.*, 1978, **47**, 819–846.

[92] Loura, L. and Prieto, M. 'Resonance Energy Transfer in Biophysics: Formalisms and Application to Membrane Model Systems'. *4th Springer Series on Fluorescence Methods and Applications*. 2008, 299–322.

[93] Farinha, J. P. and Martinho, J. M. 'Resonance Energy Transfer in Polymer Interfaces'. *4th Springer Series on Fluorescence Methods and Applications*. Springer Verlag Berlin Heidelberg, 2008, 215–256.

[94] Didenko, V. V. 'DNA probes using fluorescence resonance energy transfer (FRET): Designs and applications'. *BioTechniques*, 2001, **31**, 1106–1121.

[95] Hauser, M.; Klein, U. K. A. and Gösele, U. 'Extension of Försters Theory of Long-Range Energy Transfer to Donor-Acceptor Pairs in Systems of Molecular Dimensions'. *Z. Phys. Chem.*, 1976, **101**, 255–266.

[96] Huber, D. L.; Hamilton, D. S. and Barnett, B. 'Time-dependent effects in fluorescent line narrowing'. *Phys. Rev. B*, 1977, **16**, 4642–4650.

[97] Blumen, A. and Manz, J. 'On the concentration and time dependence of the energy transfer to randomly distributed acceptors'. *J. Chem. Phys.*, 1979, **71**, 4694–4702.

[98] Wolber, P. K. and Hudson, B. S. 'An analytic solution to the Förster energy transfer problem in two dimensions'. *Biophys. J.*, 1979, **28**, 197–210.

[99] Klafter, J and Blumen, A. 'Fractal behavior in trapping and reaction'. *J. Chem. Phys.*, 1984, **80**, 875–877.

[100] Baumann, J. and Fayer, M. D. 'Excitation transfer in disordered two-dimensional and anisotropic three-dimensional systems: Effects of spatial geometry on time-resolved observables'. *J. Chem. Phys.*, 1986, **85**, 4087–4107.

[101] Szöllosi, J.; Damjanovich, S. and Mátyus, L. 'Application of Fluorescence Resonance Energy Transfer in the Clinical Laboratory: Routine and Research'. *Cytom. Part A*, 1998, **34**, 159–179.

[102] Kenworthy, A. K. 'Imaging Protein-Protein Interactions Using Fluorescence Resonance Energy Transfer Microscopy'. *Methods*, 2001, **24**, 289–296.

[103] James, J. R.; Oliveira, M. I.; Carmo, A. M.; Iaboni, A. and Davis, S. J. 'A rigorous experimental framework for detecting protein oligomerization using bioluminescence resonance energy transfer'. *Nat. Methods*, 2006, **3**, 1001–1006.

[104] Wang, Y.; Zhao, C. L. and Winnik, M. A. 'Molecular diffusion and latex film formation: An analysis of direct nonradiative energy transfer experiments'. *J. Chem. Phys.*, 1991, **95**, 2143–2153.

[105] Draxler, S.; Lippitsch, M. E.; Klimant, I.; Kraus, H. and Wolfbeis, O. S. 'Effects of Polymer Matrices on the Time-Resolved Luminescence of a Ruthenium Complex Quenched by Oxygen'. *J. Phys. Chem.*, 1995, **99**, 3162–3167.

[106] Parkinson, P; Aharon, E; Chang, M. H.; Dosche, C; Frey, G. L.; Köhler, A and Herz, L. M. 'Dimensionality-dependent energy transfer in polymer-intercalated SnS2 nanocomposites'. *Phys. Rev. B*, 2007, **75**, 165206.

[107] Farinha, J. P. and Martinho, J. M. 'Resonance Energy Transfer in Polymer Nanodomains'. *J. Phys. Chem. C*, 2008, **112**, 10591–10601.

[108] Yekta, A.; Duhamel, J. and Winnik, M. A. 'Dipole-dipole electronic energy transfer. Fluorescence decay functions for arbitrary distributions of donors and acceptors: systems with planar geometry'. *Chem. Phys. Lett.*, 1995, **235**, 119–125.

[109] Farinha, J. P. and Martinho, J. M. 'Electronic energy transfer in restricted geometries Application to the study of spherical and planar interphases of diblock copolymer films'. *J. Lumin.*, 1997, **72-74**, 914–917.

[110] Yekta, A.; Winnik, M. A.; Farinha, J. P. and Martinho, J. M. 'Dipole-Dipole Electronic Energy Transfer. Fluorescence Decay Functions for Arbitrary Distributions of Donors and Acceptors. II. Systems with Spherical Symmetry'. *J. Phys. Chem. A*, 1997, **101**, 1787–1792.

[111] Farinha, J. P.; Spiro, J. G. and Winnik, M. A. 'Dipole-Dipole Electronic Energy Transfer: Fluorescence Decay Functions for Arbitrary Distributions'. *J. Phys. Chem. B*, 2004, **108**, 16392–16400.

[112] Achermann, M. 'Time-Resolved Photoluminescence Spectroscopy'. *Optical Techniques for Solid-State Materials Characterization*. Taylor & Francis Group, LLC, 2012, 443–465.

[113] Gong, J. Q.; Parkinson, P.; Kondratuk, D. V.; Gil-Ramírez, G.; Anderson, H. L. and Herz, L. M. 'Structure-Directed Exciton Dynamics in Templated Molecular Nanorings'. *J. Phys. Chem. C*, 2015, **119**, 6414–6420.

[114] Eggimann, H. J.; Le Roux, F. and Herz, L. M. 'How β-Phase Content Moderates Chain Conjugation and Energy Transfer in Polyfluorene Films'. *J. Phys. Chem. Lett.*, 2019, **10**, 1729–1736. https://doi.org/10.1021/acs.jpclett.9b00483.

[115] Shah, J. 'Ultrafast Luminescence Spectroscopy Using Sum Frequency Generation'. *IEEE J. Quantum Electron.*, 1988, **24**, 276–288.

[116] Hecht, E. *Optics*. Addison Wesley, 2002.

[117] Kowalevicz, A. 'Ultrashort pulse generation and measurement'. *Optical Techniques for Solid-State Materials Characterization*. Taylor & Francis Group, LLC, 2012.

[118] Edmund Optics. *Off-Axis Parabolic Metal Mirrors. https://www.edmundoptics.de/campaigns/off-axis-parabolic-metal-mirrors/ (accessed 2020-05-28)*.

[119] Rullière, C; Amand, T and Marie, X. 'Spectroscopic Methods for Analysis of Sample Dynamics'. *Femtosecond Laser Pulses - Principles and Experiments*. Ed. by Rullière, C. 2nd ed. New York, 2005, 223–281.

[120] Becker, W. *Advanced Time-Correlated Single Photon Counting Techniques*. Springer-Verlag Berlin Heidelberg, 2005.

[121] Sauer, M.; Hofkens, J. and Enderlein, J. *No Handbook of Fluorescence Spectroscopy and Imaging*. Wiley-VCH Verlag GmbH & Co, 2011.

[122] Haver, R.; Tejerina, L.; Jiang, H. W.; Rickhaus, M.; Jirasek, M.; Grübner, I.; Eggimann, H. J.; Herz, L. M. and Anderson, H. L. 'Tuning the Circumference of Six-Porphyrin Nanorings'. *J. Am. Chem. Soc.*, 2019, **141**, 7965–7971.

[123] Wahl, M. *Time-Correlated Single Photon Counting, Technical Note*. PicoQuant, 2014.

[124] Griffiths, P. R. and Haseth, J. A. de. *Fourier Transform Infrared Spectrometry*. John Wiley & Sons, Inc., 2007.

[125] Smith, B. C. *Fundamentals of Fourier Transform Infrared Spectroscopy*. CRC Press, Taylor & Francis Group, LLC, 2011.

[126] Bruker Optics. *VERTEX 80/80v. www.bruker.com (accessed 2020-05-04)*.

[127] Bruker Optics. *FT-IR Spectroscopy Basics. www.bruker.com (accessed 2020-05-19)*.

[128] Grice, A. W.; Bradley, D. D. C.; Bernius, M. T.; Inbasekaran, M.; Wu, W. W. and Woo, E. P. 'High brightness and efficiency blue light-emitting polymer diodes'. *Appl. Phys. Lett.*, 1998, **73**, 629–631.

[129] Zhang, X.; Hu, Q.; Lin, J.; Lei, Z.; Guo, X.; Xie, L.; Lai, W. and Huang, W. 'Efficient and stable deep blue polymer light-emitting devices based on β-phase poly(9,9-dioctylfluorene)'. *Appl. Phys. Lett.*, 2013, **103**, 153301.

[130] Zhang, Q.; Chi, L.; Hai, G.; Fang, Y.; Li, X.; Xia, R.; Huang, W. and Gu, E. 'An Easy Approach to Control β-Phase Formation in PFO Films for Optimized Emission Properties'. *Molecules*, 2017, **22**, 315.

[131] Chua, L. L.; Zaumseil, J.; Chang, J. F.; Ou, E. C. W.; Ho, P. K. H.; Sirringhaus, H. and Friend, R. H. 'General observation of n-type field-effect behaviour in organic semiconductors'. *Nature*, 2005, **434**, 194–199.

[132] Heliotis, G.; Xia, R.; Bradley, D. D. C.; Turnbull, G. A.; Samuel, I. D.; Andrew, P. and Barnes, W. L. 'Blue, surface-emitting, distributed feedback polyfluorene lasers'. *Appl. Phys. Lett.*, 2003, **83**, 2118–2120.

[133] Rothe, C.; Galbrecht, F.; Scherf, U. and Monkman, A. 'The β-Phase of Poly(9,9-dioctylfluorene) as a Potential System for Electrically Pumped Organic Lasing'. *Adv. Mater.*, 2006, **18**, 2137–2140.

[134] Lu, H.-H.; Liu, C.-Y.; Chang, C.-H. and Chen, S.-A. 'Self-Dopant Formation in Poly(9,9-di-n-octylfluorene) via a Dipping Method for Efficient and Stable Pure-Blue Electroluminescence'. *Adv. Mater.*, 2007, **19**, 2574–2579.

[135] Perevedentsev, A.; Chander, N.; Kim, J.-S. S. and Bradley, D. D. C. 'Spectroscopic properties of poly(9,9-dioctylfluorene) thin films possessing varied fractions of β-phase chain segments: enhanced photoluminescence efficiency via conformation structuring'. *J. Polym. Sci. B*, 2016, **54**, 1995–2006.

[136] Yap, B. K.; Xia, R.; Campoy-Quiles, M.; Stavrinou, P. N. and Bradley, D. D. C. 'Simultaneous optimization of charge-carrier mobility and optical gain in semiconducting polymer films'. *Nat. Mater.*, 2008, **7**, 376–380.

[137] Bradley, D. D. C.; Grell, M.; Long, X.; Mellor, H.; Grice, A.; Road, H.; Inbasekaran, M. and Woo, E. P. 'Influence of Aggregation on the Optical Properties of a Polyfluorene'. *Proc. SPIE*, 1997, **3145**. Ed. by Vardeny, Z. V. and Rothberg, L. J., 254–259.

[138] Grell, M.; Bradley, D. D. C.; Ungar, G.; Hill, J. and Whitehead, K. S. 'Interplay of Physical Structure and Photophysics for a Liquid Crystalline Polyfluorene'. *Macromolecules*, 1999, **32**, 5810–5817.

[139] Scherf, U. and List, E. J. W. 'Semiconducting Polyfluorenes - Towards Reliable Structure-Property Relationships'. *Adv. Mater.*, 2002, **14**, 477–487.

[140] Ariu, M.; Lidzey, D. G.; Sims, M.; Cadby, A. J.; Lane, P. A and Bradley, D. D. C. 'The effect of morphology on the temperature-dependent photoluminescence quantum efficiency of the conjugated polymer poly(9,9-dioctylfluorene'. *J. Phys. Condens. Matter*, 2002, **14**, 9975–9986.

[141] Monkman, A.; Rothe, C.; King, S. and Dias, F. 'Polyfluorene Photophysics'. *Adv. Polym. Sci.*, 2008, **212**, 187–225.

[142] Chunwaschirasiri, W; Tanto, B; Huber, D. L. and Winokur, M. J. 'Chain conformations and photoluminescence of poly(di-n-octylfluorene)'. *Phys. Rev. Lett.*, 2005, **94**, 107402.

[143] Sirtonski, M. R.; McFarlane, S. L. and Veinot, J. G. 'Stabilizing the optical properties of PFO through addition of a non-volatile low molecular weight aromatic ether'. *J. Mater. Chem.*, 2010, **20**, 8147–8152.

[144] Bansal, A. K.; Ruseckas, A.; Shaw, P. E. and Samuel, I. D. W. 'Fluorescence Quenchers in Mixed Phase Polyfluorene Films'. *J. Phys. Chem. C*, 2010, **114**, 17864–17867.

[145] Peet, J.; Brocker, E.; Xu, Y. and Bazan, G. C. 'Controlled Beta-Phase Formation in Poly(9,9-di-n-octylfluorene) by Processing with Alkyl Additives'. *Adv. Mater.*, 2008, **20**, 1882–1885.

[146] Yu, M. N.; Soleimaninejad, H.; Lin, J. Y.; Zuo, Z. Y.; Liu, B.; Bo, Y. F.; Bai, L. B.; Han, Y. M.; Smith, T. A.; Xu, M. *et al.* 'Photophysical and Fluorescence Anisotropic Behavior of Polyfluorene β-Conformation Films'. *J. Phys. Chem. Lett.*, 2018, **9**, 364–372.

[147] Shaw, P. E.; Ruseckas, A.; Peet, J.; Bazan, G. C. and Samuel, I. D. W. 'Exciton-Exciton Annihilation in Mixed-Phase Polyfluorene Films'. *Adv. Funct. Mater.*, 2010, **20**, 155–161.

[148] Denis, J.-C.; Schumacher, S.; Hedley, G. J.; Ruseckas, A.; Morawska, P. O.; Wang, Y.; Allard, S.; Scherf, U.; Turnbull, G. A.; Samuel, I. D. W. *et al.* 'Subpicosecond Exciton Dynamics in Polyfluorene Films from Experiment and Microscopic Theory'. *J. Phys. Chem. C*, 2015, **119**, 9734–9744.

[149] Schwartz, B. J. 'Conjugated Polymers as Molecular Materials: How Chain Conformation and Film Morphology Influence Energy Transfer and Interchain Interactions'. *Annu. Rev. Phys. Chem.*, 2003, **54**, 141–172.

[150] Huang, L.; Huang, X.; Sun, G.; Gu, C.; Lu, D. and Ma, Y. 'Study of β-Phase and Chains Aggregation Degrees in Poly(9,9-dioctylfluorene) (PFO) Solution'. *J. Phys. Chem. C*, 2012, **116**, 7993–7999.

[151] Ariu, M.; Sims, M.; Rahn, M.; Hill, J.; Fox, A. M.; Lidzey, D. G.; Oda, M.; Cabanillas-Gonzalez, J. and Bradley, D. D. C. 'Exciton migration in β-phase Poly(9,9-dioctylfluorene)'. *Phys. Rev. B*, 2003, **67**, 1–11.

[152] Chang, M. H.; Hoffmann, M.; Anderson, H. L. and Herz, L. M. 'Dynamics of Excited-State Conformational Relaxation and Electronic Delocalization in Conjugated Porphyrin Oligomers'. *J. Am. Chem. Soc.*, 2008, **130**, 10171–10178.

[153] Brown, P. J.; Thomas, D. S.; Köhler, A.; Wilson, J. S.; Kim, J. S.; Ramsdale, C. M.; Sirringhaus, H. and Friend, R. H. 'Effect of interchain interactions on the absorption and emission of poly(3-hexylthiophene)'. *Phys. Rev. B*, 2003, **67**, 064203.

[154] Hoffmann, S. T.; Scheler, E.; Koenen, J. M.; Forster, M.; Scherf, U.; Strohriegl, P.; Bässler, H. and Köhler, A. 'Triplet energy transfer in conjugated polymers. III. An experimental assessment regarding the influence of disorder on polaronic transport'. *Phys. Rev. B*, 2010, **81**, 165208.

[155] Cornil, J.; Beljonne, D.; Heller, C. M.; Campbell, I. H.; Laurich, B. K.; Smith, D. L.; Bradley, D. D. C.; Müllen, K. and Brédas, J. L. 'Photoluminescence spectra of oligo-paraphenylenevinylenes: a joint theoretical and experimental characterization'. *Chem. Phys. Lett.*, 1997, **278**, 139–145.

[156] Wasserberg, D.; Dudek, S. P.; Meskers, S. C. and Janssen, R. A. 'Comparison of the chain length dependence of the singlet- and triplet-excited states of oligofluorene'. *Chem. Phys. Lett.*, 2005, **411**, 273–277.

[157] Huber, D. L. and Avgin, I. 'Optical Absorption of the β-Phase of Poly(9,9-dioctylfluorene)'. *J. Polym. Sci. B*, 2016, **54**, 1109–1111.

[158] Avgin, I. and Huber, D. L. 'Excitons in disordered polymers'. *J. Lumin.*, 2007, **122-123**, 389–392.

[159] Silva, C.; Russell, D. M.; Dhoot, A. S.; Herz, L. M.; Daniel, C.; Greenham, N. C.; Arias, A. C.; Setayesh, S.; Müllen, K. and Friend, R. H. 'Exciton and polaron dynamics in a step-ladder polymeric semiconductor: the influence of interchain order'. *J. Phys. Condens. Matter*, 2002, **14**, 9803–9824.

[160] Nijegorodov, N. I. and Downey, W. S. 'The Influence of Planarity and Rigidity on the Absorption and Fluorescence Parameters and Intersystem Crossing Rate Constant in Aromatic Molecules'. *J. Phys. Chem.*, 1994, **98**, 5639–5643.

[161] Khan, A. L. T.; Sreearunothai, P.; Herz, L. M.; Banach, M. J. and Köhler, A. 'Morphology-dependent energy transfer within polyfluorene thin films'. *Phys. Rev. B*, 2004, **69**, 085201.

[162] Montilla, F.; Ruseckas, A. and Samuel, I. D. W. 'Exciton-Polaron Interactions in Polyfluorene Films with β-Phase'. *J. Phys. Chem. C*, 2018, **122**, 9766–9772.

[163] Herz, L. M.; Silva, C.; Friend, R. H.; Phillips, R. T.; Setayesh, S.; Becker, S.; Marsitsky, D. and Müllen, K. 'Effects of aggregation on the excitation transfer in perylene-end-capped polyindenofluorene studied by time-resolved photoluminescence spectroscopy'. *Phys. Rev. B*, 2001, **64**, 195203.

[164] Chang, M. H.; Frampton, M. J.; Anderson, H. L. and Herz, L. M. 'Intermolecular Interaction Effects on the Ultrafast Depolarization of the Optical Emission from Conjugated Polymers'. *Phys. Rev. Lett.*, 2007, **98**, 027402.

[165] Powell, R. C. and Soos, Z. G. 'Singlet Exciton Energy Transfer in Organic Solids'. *J. Lumin.*, 1975, **11**, 1–45.

[166] Powell, R. C. and Kepler, R. G. 'Evidence for Long-Range Exciton-Impurity Interaction in Tetracene-Doped Anthracene Crystals'. *Phys. Rev. Lett.*, 1969, **22**, 636–639.

[167] Herz, L. M. 'Aggregation Effects in Conjugated Polymer Films Studied by Time-Resolved Photoluminescence Spectroscopy'. PhD thesis. University of Cambridge, 2001.

[168] Herz, L. M.; Silva, C; Grimsdale, A. C.; Müllen, K and Phillips, R. T. 'Time-dependent energy transfer rates in a conjugated polymer guest-host system'. *Phys. Rev. B*, 2004, **70**, 1–9.

[169] Stevens, M. A.; Silva, C.; Russell, D. M. and Friend, R. H. 'Exciton dissociation mechanisms in the polymeric semiconductors poly(9,9-dioctylfluorene) and poly(9,9-dioctylfluorene-co-benzothiadiazole)'. *Phys. Rev. B*, 2001, **63**, 165213.

[170] Maksimov, M. and Rozman, I. 'On Energy Transfer in Solid Solutions'. *Opt. Spectrosc. USSR*, 1961, **12**, 337–338.

[171] Lunt, R. R.; Giebink, N. C.; Belak, A. A.; Benziger, J. B. and Forrest, S. R. 'Exciton diffusion lengths of organic semiconductor thin films measured by spectrally resolved photoluminescence quenching'. *J. Appl. Phys.*, 2009, **105**, 53711.

[172] Campoy-Quiles, M.; Heliotis, G.; Xia, R.; Ariu, M.; Pintani, M.; Etchegoin, P. and Bradley, D. D. 'Ellipsometric Characterization of the Optical Constants of Polyfluorene Gain Media'. *Adv. Funct. Mater.*, 2005, **15**, 925–933.

[173] Campoy-Quiles, M.; Alonso, M. I.; Bradley, D. D. and Richter, L. J. 'Advanced Ellipsometric Characterization of Conjugated Polymer Films'. *Adv. Funct. Mater.*, 2014, **24**, 2116–2134.

[174] Tropf, L.; Dietrich, C. P.; Herbst, S.; Kanibolotsky, A. L.; Skabara, P. J.; Würthner, F.; Samuel, I. D.; Gather, M. C. and Höfling, S. 'Influence of optical material properties on strong coupling in organic semiconductor based microcavities'. *Appl. Phys. Lett.*, 2017, **110**, 153302.

[175] Macdonald, E. K. and Shaver, M. P. 'Intrinsic high refractive index polymers'. *Polym. Int.*, 2015, **64**, 6–14.

[176] Tabata, K.; Braam, D.; Kushida, S.; Tong, L.; Kuwabara, J.; Kanbara, T.; Beckel, A.; Lorke, A. and Yamamoto, Y. 'Self-assembled conjugated polymer spheres as fluorescent microresonators'. *Sci. Rep.*, 2014, **4**, 5902.

[177] Stryer, L.; Thomas, D. D. and Meares, C. F. 'Diffusion-enhanced fluorescence energy transfer'. *Ann. Rev. Biophys. Bioeng.*, 1982, **11**, 203–222.

[178] Lyons, B. P. and Monkman, A. P. 'The role of exciton diffusion in energy transfer between polyfluorene and tetraphenyl porphyrin'. *Phys. Rev. B*, 2005, **71**, 235201.

[179] Collini, E. and Scholes, G. D. 'Coherent Intrachain Energy Migration in a Conjugated Polymer at Room Temperature'. *Science*, 2009, **323**, 369–373.

[180] Perevedentsev, A.; Stavrinou, P. N.; Smith, P. and Bradley, D. D. C. 'Solution-Crystallization and Related Phenomena in 9,9-Dialkyl-Fluorene Polymers. II. Influence of Side-Chain Structure'. *J. Polym. Sci. B*, 2015, **53**, 1492–1506.

[181] Reichenberger, M.; Kroh, D.; Matrone, G. M. M.; Schötz, K.; Pröller, S.; Filonik, O.; Thordardottir, M. E.; Herzig, E. M.; Bässler, H.; Stingelin, N. *et al.* 'Controlling Aggregate Formation in Conjugated Polymers by Spin-Coating Below the Critical Temperature of the Disorder-Order Transition'. *J. Polym. Sci. B*, 2018, **56**, 532–542.

[182] Eggimann, H. J.; Patel, J. B.; Johnston, M. B. and Herz, L. M. 'Efficient Energy Transfer Mitigates Parasitic Light Absorption in Molecular Charge-Extraction Layers for Perovskite Solar Cells'. *Nat. Commun.*, 2020, **11**, 5525. https://doi.org/10.1038/s41467-020-19268-w.

[183] Park, B. W.; Philippe, B.; Jain, S. M.; Zhang, X.; Edvinsson, T.; Rensmo, H.; Zietz, B. and Boschloo, G. 'Chemical engineering of methylammonium lead iodide/bromide perovskites: tuning of opto-electronic properties and photovoltaic performance'. *J. Mater. Chem. A*, 2015, **3**, 21760–21771.

[184] Saliba, M.; Correa-Baena, J.-P.; Grätzel, M.; Hagfeldt, A. and Abate, A. 'Perowskit-Solarzellen: atomare Ebene, Schichtqualität und Leistungsfähigkeit der Zellen'. *Angew. Chem.*, 2018, **130**, 2582–2598.

[185] Herz, L. M. 'Charge-Carrier Mobilities in Metal Halide Perovskites: Fundamental Mechanisms and Limits'. *ACS Energy Lett.*, 2017, **2**, 1539–1548.

[186] Meggiolaro, D.; Motti, S. G.; Mosconi, E.; Barker, A. J.; Ball, J.; Andrea Riccardo Perini, C.; Deschler, F.; Petrozza, A. and De Angelis, F. 'Iodine chemistry determines the defect tolerance of lead-halide perovskites'. *Energy Environ. Sci.*, 2018, **11**, 702–713.

[187] NREL. *Best Research-Cell Efficiency Chart. https://www.nrel.gov/pv/cell-efficiency.html (accessed 2020-05-26).*

[188] Fang, Y.; Bi, C.; Wang, D. and Huang, J. 'The Functions of Fullerenes in Hybrid Perovskite Solar Cells'. *ACS Energy Lett.*, 2017, **2**, 782–794.

[189] Jung, E. H.; Jeon, N. J.; Park, E. Y.; Moon, C. S.; Shin, T. J.; Yang, T. Y.; Noh, J. H. and Seo, J. 'Efficient, stable and scalable perovskite solar cells using poly(3-hexylthiophene)'. *Nature*, 2019, **567**, 511–515.

[190] Schloemer, T. H.; Christians, J. A.; Luther, J. M. and Sellinger, A. 'Doping strategies for small molecule organic hole-transport materials: impacts on perovskite solar cell performance and stability'. *Chem. Sci.*, 2019, **10**, 1904–1935.

[191] Zhang, Y.; Liu, M.; Eperon, G. E.; Leijtens, T. C.; McMeekin, D.; Saliba, M.; Zhang, W.; De Bastiani, M.; Petrozza, A.; Herz, L. M. *et al.* 'Charge selective contacts, mobile ions and anomalous hysteresis in organic-inorganic perovskite solar cells'. *Mater. Horiz.*, 2015, **2**, 315–322.

[192] Eames, C.; Frost, J. M.; Barnes, P. R.; O'Regan, B. C.; Walsh, A. and Islam, M. S. 'Ionic transport in hybrid lead iodide perovskite solar cells'. *Nat. Commun.*, 2015, **6**, 7495.

[193] Lin, R.; Xiao, K.; Qin, Z.; Han, Q.; Zhang, C.; Wei, M.; Saidaminov, M. I.; Gao, Y.; Xu, J.; Xiao, M. *et al.* 'Monolithic all-perovskite tandem solar cells with 24.8% efficiency exploiting comproportionation to suppress Sn(ii) oxidation in precursor ink'. *Nat. Energy*, 2019, **4**, 864–873.

[194] Palmstrom, A. F.; Eperon, G. E.; Leijtens, T.; Prasanna, R.; Habisreutinger, S. N.; Nemeth, W.; Gaulding, E. A.; Dunfield, S. P.; Reese, M.; Nanayakkara, S. *et al.* 'Enabling Flexible All-Perovskite Tandem Solar Cells'. *Joule*, 2019, **3**, 2193–2204.

[195] Jiang, Y.; Almansouri, I.; Huang, S.; Young, T.; Li, Y.; Peng, Y.; Hou, Q.; Spiccia, L.; Bach, U.; Cheng, Y. B. *et al.* 'Optical analysis of perovskite/silicon tandem solar cells'. *J. Mater. Chem. C*, 2016, **4**, 5679–5689.

[196] Kirchartz, T.; Staub, F. and Rau, U. 'Impact of Photon Recycling on the Open-Circuit Voltage of Metal Halide Perovskite Solar Cells'. *ACS Energy Lett.*, 2016, **1**, 731–739.

[197] Filipič, M.; Löper, P.; Niesen, B.; De Wolf, S.; Krč, J.; Ballif, C. and Topič, M. 'CH3NH3PbI3 perovskite / silicon tandem solar cells: characterization based optical simulations'. *Opt. Express*, 2015, **23**, A263.

[198] Ball, J. M.; Stranks, S. D.; Hörantner, M. T.; Hüttner, S.; Zhang, W.; Crossland, E. J.; Ramirez, I.; Riede, M.; Johnston, M. B.; Friend, R. H. *et al.* 'Optical properties and limiting photocurrent of thin-film perovskite solar cells'. *Energy Environ. Sci.*, 2015, **8**, 602–609.

[199] Albrecht, S.; Saliba, M.; Correa-Baena, J. P.; Jäger, K.; Korte, L.; Hagfeldt, A.; Grätzel, M. and Rech, B. 'Towards optical optimization of planar monolithic perovskite/silicon-heterojunction tandem solar cells'. *J. Opt.*, 2016, **18**, 064012.

[200] Patel, J. B.; Wong-Leung, J.; Van Reenen, S.; Sakai, N.; Wang, J. T. W.; Parrott, E. S.; Liu, M.; Snaith, H. J.; Herz, L. M. and Johnston, M. B. 'Influence of Interface Morphology on Hysteresis in Vapor-Deposited Perovskite Solar Cells'. *Adv. Electron. Mater.*, 2017, **3**, 1600470.

[201] Ishida, H.; Bünzli, J. C. and Beeby, A. *Guidelines for measurement of luminescence spectra and quantum yields of inorganic and organometallic compounds in solution and solid state (IUPAC Technical Report)*. 2016.

[202] Trimpl, M. J. *Charge-Carrier Recombination and Trapping Mechanisms in Metal Halide Perovskite Semiconductors. Master Thesis. Technische Universität München.* 2019.

[203] Ball, J. M.; Stranks, S. D.; Hörantner, M. T.; Hüttner, S.; Zhang, W.; Crossland, E. J.; Ramirez, I.; Riede, M.; Johnston, M. B.; Friend, R. H. *et al.* 'Optical properties and limiting photocurrent of thin-film perovskite solar cells'. *Energy Environ. Sci.*, 2015, **8**, 602–609.

[204] Virtanen, P.; Gommers, R.; Oliphant, T. E.; Haberland, M.; Reddy, T.; Cournapeau, D.; Burovski, E.; Peterson, P.; Weckesser, W.; Bright, J. *et al.* 'SciPy 1.0: Fundamental Algorithms for Scientific Computing in Python'. *Nat. Methods*, 2020, **17**, 261–272.

[205] Cho, I. W. and Ryu, M. Y. 'Effect of energy transfer on the optical properties of surface-passivated perovskite films with CdSe/ZnS quantum dots'. *Sci. Rep.*, 2019, **9**, 18433.

[206] Rabouw, F. T.; Den Hartog, S. A.; Senden, T. and Meijerink, A. 'Photonic effects on the Förster resonance energy transfer efficiency'. *Nat. Commun.*, 2014, **5**, 3610.

[207] Galkowski, K.; Mitioglu, A.; Miyata, A.; Plochocka, P.; Portugall, O.; Eperon, G. E.; Wang, J. T. W.; Stergiopoulos, T.; Stranks, S. D.; Snaith, H. J. *et al.* 'Determination of the exciton binding energy and effective masses for methylammonium and formamidinium lead tri-halide perovskite semiconductors'. *Energy Environ. Sci.*, 2016, **9**, 962–970.

[208] Calió, L.; Kazim, S.; Grätzel, M. and Ahmad, S. 'Hole-Transport Materials for Perovskite Solar Cells'. *Angew. Chem. Int. Ed.*, 2016, **55**, 14522–14545.

[209] Sakurai, K.; Tachibana, H.; Shiga, N.; Terakura, C.; Matsumoto, M. and Tokura, Y. 'Experimental determination of excitonic structure in polythiophene'. *Phys. Rev. B*, 1997, **56**, 9552–9556.

[210] Jiang, X. M.; Österbacka, R.; Korovyanko, O.; An, C. P.; Horovitz, B.; Janssen, R. A. and Vardeny, Z. V. 'Spectroscopic Studies of Photoexcitations in Regioregular and Regiorandom Polythiophene Films'. *Adv. Funct. Mater.*, 2002, **12**, 587–597.

[211] Koren, A. B.; Curtis, M. D.; Francis, A. H. and Kampf, J. W. 'Intermolecular Interactions in π-Stacked Conjugated Molecules. Synthesis, Structure, and Spectral Characterization of Alkyl Bithiazole Oligomers'. *J. Am. Chem. Soc.*, 2003, **125**, 5040–5050.

[212] Kobayashi, T.; Hamazaki, J.-i.; Kunugita, H.; Ema, K.; Endo, T.; Rikukawa, M. and Sanui, K. 'Coexistence of photoluminescence from two intrachain states in polythiophene films'. *Phys. Rev. B*, 2003, **67**, 205214.

[213] Spano, F. C. 'Modeling disorder in polymer aggregates: The optical spectroscopy of regioregular poly(3-hexylthiophene) thin films'. *J. Chem. Phys.*, 2005, **122**, 234701.

[214] Clark, J.; Silva, C.; Friend, R. H. and Spano, F. C. 'Role of Intermolecular Coupling in the Photophysics of Disordered Organic Semiconductors: Aggregate Emission in Regioregular Polythiophene'. *Phys. Rev. Lett.*, 2007, **98**, 206406.

[215] Cook, S.; Furube, A. and Katoh, R. 'Analysis of the excited states of regioregular polythiophene P3HT'. *Energy Environ. Sci.*, 2008, **1**, 294–299.

[216] Kline, R. J. and McGehee, M. D. 'Morphology and Charge Transport in Conjugated Polymers'. *Polym. Rev.*, 2006, **46**, 27–45.

[217] Joshi, S.; Grigorian, S.; Pietsch, U.; Pingel, P.; Zen, A.; Neher, D. and Scherf, U. 'Thickness Dependence of the Crystalline Structure and Hole Mobility in Thin Films of Low Molecular Weight Poly(3-hexylthiophene)'. *Macromolecules*, 2008, **41**, 6800–6808.

[218] Brinkmann, M. 'Structure and Morphology Control in Thin Films of Regioregular Poly(3-hexylthiophene)'. *J. Polym. Sci. Pol. Phys.*, 2011, **49**, 1218–1233.

[219] O'Connor, B.; Kline, R. J.; Conrad, B. R.; Richter, L. J.; Gundlach, D.; Toney, M. F. and DeLongchamp, D. M. 'Anisotropic Structure and Charge Transport in Highly Strain-Aligned Regioregular Poly(3-hexylthiophene)'. *Adv. Funct. Mater.*, 2011, **21**, 3697–3705.

[220] Heo, J. H.; Im, S. H.; Noh, J. H.; Mandal, T. N.; Lim, C. S.; Chang, J. A.; Lee, Y. H.; Kim, H. J.; Sarkar, A.; Nazeeruddin, M. K. *et al.* 'Efficient inorganic-organic hybrid heterojunction solar cells containing perovskite compound and polymeric hole conductors'. *Nat. Photonics*, 2013, **7**, 486–491.

[221] Zhou, P.; Bu, T.; Shi, S.; Li, L.; Zhang, Y.; Ku, Z.; Peng, Y.; Zhong, J.; Cheng, Y. B. and Huang, F. 'Efficient and stable mixed perovskite solar cells using P3HT as a hole transporting layer'. *J. Mater. Chem. C*, 2018, **6**, 5733–5737.

[222] Clark, J.; Chang, J. F.; Spano, F. C.; Friend, R. H. and Silva, C. 'Determining exciton bandwidth and film microstructure in polythiophene films using linear absorption spectroscopy'. *Appl. Phys. Lett.*, 2009, **94**, 163306.

[223] Hildner, R.; Köhler, A.; Müller-Buschbaum, P.; Panzer, F. and Thelakkat, M. 'π-Conjugated Donor Polymers: Structure Formation and Morphology in Solution, Bulk and Photovoltaic Blends'. *Adv. Energy Mater.*, 2017, **7**, 1700314.

[224] Halászová, S.; Váry, T.; Nádašdy, V.; Chlpík, J. and Cirák, J. 'Effect of Substrate Roughness on Photoluminescence of Poly(3-Hexylthiophene)'. *AIP Conference Proceedings*. Vol. 1996. 2018, 20051.

[225] Pereira, V. S.; Leal, L. A.; Ribeiro Junior, L. A. and Blawid, S. 'Inferring changes in π-stack mobility induced by aging from vibronic transitions in poly(3-hexylthiophene-2,5-diyl) films'. *Synth. Met.*, 2019, **247**, 276–284.

[226] Tsoi, W. C.; Spencer, S. J.; Yang, L.; Ballantyne, A. M.; Nicholson, P. G.; Turnbull, A.; Shard, A. G.; Murphy, C. E.; Bradley, D. D.; Nelson, J. *et al.* 'Effect of Crystallization on the Electronic Energy Levels and Thin Film Morphology of P3HT:PCBM Blends'. *Macromolecules*, 2011, **44**, 2944–2952.

[227] Herrmann, D.; Niesar, S.; Scharsich, C.; Köhler, A.; Stutzmann, M. and Riedle, E. 'Role of Structural Order and Excess Energy on Ultrafast Free Charge Generation in Hybrid Polythiophene/Si Photovoltaics Probed in Real Time by Near-Infrared Broadband Transient Absorption'. *J. Am. Chem. Soc.*, 2011, **133**, 18220–18233.

[228] Müller-Buschbaum, P. 'Probing Organic Solar Cells with Grazing Incidence Scattering Techniques'. *Synchrotron Radiation in Materials Science*. 2018.

[229] Wang, T.; Pearson, A. J.; Dunbar, A. D.; Staniec, P. A.; Watters, D. C.; Coles, D.; Yi, H.; Iraqi, A.; Lidzey, D. G. and Jones, R. A. 'Competition between substrate-mediated π - π stacking and surface-mediated Tg depression in ultrathin conjugated polymer films'. *Eur. Phys. J E Soft Matter*, 2012, **35**, 129.